University of West Bohemia
Faculty of Applied Sciences

# Magnetron sputtering of films with enhanced mechanical and tribological properties

Ing. Daniel Javdošňák

*A thesis submitted for the degree of Doctor of Philosophy*
*in the field of Plasma Physics and Physics of Thin Films*

Supervisor: prof. Ing. Jindřich Musil, DrSc.
Department of Physics

Pilsen 2019

Západočeská univerzita v Plzni
Fakulta aplikovaných věd

# Magnetronové naprašování vrstev s vylepšenými mechanickými a tribologickými vlastnostmi

Ing. Daniel Javdošňák

*Disertační práce k získání akademického titulu doktor v oboru Fyzika Plazmatu a Tenkých Vrstev*

Školitel: prof. Ing. Jindřich Musil, DrSc.
Katedra Fyziky

Plzeň 2019

# Preface

The work presented in this Ph.D. thesis has been carry out 2015–2019 at the laboratory of Department of Physics and NTIS – European Centre of Excellence, Faculty of Applied Sciences, University of West Bohemia in Pilsen (Czech Republic). This thesis is to the best of my knowledge original, except parts where references are made to previous scientific articles and literature. The thesis is submitted in a form of four topics, and three of which have been published in the form of scientific publications.

Financial support of the research was provided by the projects SGS–2013–045 (2015): Novel thin-film materials and plasma deposition systems, SGS–2016–056 (2016–2018): New nanostructured thin-film materials formed by plasma technologies, SGS–2019–031 (2019): New thin-film materials formed by advanced plasma technologies, GA16-18183S: Advanced surface coatings with enhanced properties and thermal stability, and LO1506: Sustainability support of the center NTIS - New Technologies for the Information Society.

Pilsen, November 2019 ……...…………….. Ing. Daniel Javdošňák

# Acknowledgments

My Ph.D. study has brought me lots of interesting experiences and knowledge in the field of research of the new materials.

Firstly, I would like to thank Prof. Ing. Jindřich Musil, DrSc. for being my PhD supervisor, who has been a tremendous mentor with an inexhaustible source of ideas and inspiration. I really appreciate the opportunity to work in your team. I would like to thank him for his guidance, patience, motivation, encouraging of my research, handing over me a lot of valuable experience in order to rise me a good scientist. I am grateful for giving me the chance to present my work at many international conferences in Europe and USA. I appreciate it very much.

Besides my supervisor, I would like to thank head of department Prof. RNDr. Jaroslav Vlček, CSc. who provided me a deeper insight into the beauty of plasma physics. I am grateful for your excellent management of the department and provided friendly atmosphere and organization. I appreciate your support during my whole study at the department of physics.

I am also thankful to Asoc. Profs. Ing. Jiří Houška and Šimon Kos for their fruitful cooperation on research and scientific discussion on the topic of solid-state physics. Moreover, I emphasize my thanks to Asoc. Profs. Pavel Baroch and Petr Zeman for the valuable advice and providing information about deposition techniques and thin films.

This work would not have been possible without the scientific and technical support of many people, including: Ing. Radomír Čerstvý for X-ray diffraction and nanoindentation, RNDr. Stanislav Haviar, Ph.D. for SEM (EDX, WDX), Ing. Zbyněk Soukup, Ph.D. for wear and friction coefficient measurements, Ing. Tomáš Tölg for support with electrical network and power supply connections, Asoc. Prof. Jiří Houška, Ph.D. for Ellipsometry and optical spectroscopy, and many great people of our department not listed here.

I am very grateful to all stuff and my colleagues (Ph.D. students) who inspired me, cooperated, gave me a feedback and lots of help, and created a friendly environment. My thanks belong to all my fellow workers and other “Labkouns” (graduates of Ph.D. study) with whom I have met during my four years of studying.

Finally, I would like to express my warmest gratitude to my parents, who believed and supported me. And the biggest thanks go to my beloved wife Yuliia, for her love, patience and encouragements.

# Contents


I. **Introduction** ........ 1
1. Designing of protective – wear resistant films ........ 1
1.1. Friction ........ 3
1.2. Wear ........ 4
1.2.1. Crack nucleation ........ 4
1.3. Hardness ........ 5
1.3.1. Nanocomposite films ........ 7
1.4. Toughness ........ 8
1.4.1. $H/E$ ratio ≈ toughness ........ 8
1.4.2. $B/G$ ratio and Cauchy pressure $C_{12}$ - $C_{44}$ ≈ ductility ........ 8
1.4.3. Toughening approaches ........ 9
2. Designing of films with enhanced cracking resistance ........ 11
3. Al-Si films ........ 13
4. Al-Si-N films ........ 14
5. W films ........ 15
6. Ti-W films ........ 17
7. $WN_x$ films ........ 19
II. **Aims of the thesis** ........ 21
III. **Experimental details** ........ 22
1. Film preparation ........ 22
1.1. Magnetron sputtering ........ 22
1.2. Experimental setup ........ 23
1.3. Substrates and preparation prior to deposition ........ 25
1.4. Deposition conditions ........ 26
1.4.1. Al-Si films ........ 26
1.4.2. Al-Si-N films ........ 26
1.4.3. W films ........ 27
1.4.4. Ti-W films ........ 27
1.4.5. $WN_x$ films ........ 27
2. Film characterization ........ 28
2.1. Profilometry ........ 28
2.2. Structure - XRD ........ 28
2.3. Elemental composition ........ 29
2.4. Surface morphology and cross-section ........ 29
2.5. Mechanical properties ........ 29
2.6. Cracking resistance ........ 29
2.7. Tribological properties ........ 30
2.8. Spectroscopic ellipsometry ........ 30
IV. **Results and discussion** ........ 31
A. Mechanical and tribological properties of Al-Si films deposited by magnetron sputtering ........ 32
1. Elemental content ........ 33
2. Structure and microstructure ........ 33
3. Mechanical properties ........ 37
3.1. Effect of the O content on the mechanical properties ........ 39
4. Resistance to cracking ........ 40
5. Friction and wear ........ 42
B. On the significance of the microstructure in wear resistance of ceramic films ........ 45
1. Structure and microstructure ........ 46

2. Mechanical properties ... 47
3. Wear resistance ... 48
C. Hardness enhancement in W films deposited by magnetron sputtering ... 52
1. Adhesion ... 53
2. Deposition conditions ... 55
3. Structure and microstructure ... 57
4. Mechanical properties ... 59
D. Thermal stability of β-(Ti,W) films deposited by magnetron sputtering ... 62
1. Structure and microstructure of high-T β-Ti films ... 63
2. Thermal stability of high-T β-phase films ... 65
3. Mechanical properties of films ... 66
4. Cracking resistance of films ... 67
E. Tribological properties and oxidation resistance of tungsten and tungsten nitride films at temperatures up to 500 °C ... 69
1. Structure, microstructure and mechanical properties ... 70
2. Tribological properties at temperatures up to 500°C ... 72
3. Oxidation resistance at temperatures up to 500 °C ... 77
V. **Conclusions** ... 81
VI. **Appendix** ... 84
VII. **References** ... 85
VIII. **Further publications of the candidate** ... 96
1. Papers in international journals ... 96
2. Oral presentations at international conferences ... 96
3. Poster presentations at international conferences ... 97
**Abstract** ... 98
**Resumé česky** ... 100

# I. Introduction

In recent years there is increasing demand for films (coatings) (with thickness typically between 0.5 μm and 10 μm) that allow to protect the base material against cracking or wear, and thus prolong its lifetime. These films are referred to so-called protective films, exhibiting either high hardness (>20 GPa) and simultaneously high toughness, or exhibit low friction coefficient (<0.2) and form solid lubricants. The most common use of such films is in the field of machinery industry (high-speed cutting tools, drill bits, dies, molds, etc.), automotive (bearings and engine parts), and aerospace (bearings). Historically, the most common commercially used (from 80s) thin film is TiN. It has been mainly used on high-speed steel tools for metal cutting, but it has also found other tribological applications, such as in forming tools, bearings, seals and as an erosion protection layer. One important attraction of the titanium nitride is its golden color.

## 1. Designing of protective – wear resistant films

Both properties (friction and wear) are mutually exclusive, and to achieve both low friction and low wear rate in the material is often a difficult task. Because the low friction material has low **shear strength** ($\sigma_0$) and thus low shear strength leads to high wear rates. Therefore, the aim of the protective thin films is to ensure that the availability of the low shear strength phase is just sufficient to impart the friction properties (only on the surface), but without excessive wear taking place [1].

The equation (1.1) [2–4] is very important, since it suggests a key way of reducing friction. If thin film or the third body interposed between two surfaces (film and counterpart) exhibits low shear strength, then the **coefficient of friction** ($\mu$) can be low. It means that to achieve low friction in materials, the shear strength must be also low. Low friction materials (thin films) are often denoted like "easy-to-shear" materials. From classical models for sliding friction, in the case of metals, the shear strength at a first approximation is proportional to their hardness $H \approx 5\sigma_0$ [5]. This is the main principle of lubricious thin films materials.

$$\mu = \sigma_0 \pi \left(\frac{3}{4}\frac{R}{E^*}\right)^{2/3} L^{-1/3} \tag{1.1}$$

Where $R$ is relative radius of curvature of a contact bodies, $E^* = E/(1-v^2)$ is the effective Young's modulus, $E$ is the Young's modulus and $v$ is the Poisson's ratio, and $L$ is normal load,

In order to develop protective wear resistant film (for cutting tools or self-lubrication applications), the following requirements should be fulfilled [1,6]: (1) The **hardness** and **toughness** requirement: while for tools the hardness is a prime metric to ensure reliable cutting, tool life time, and machining quality, the machine contacts do not normally require very hard mating contacts as the contact load is usually distributed and contact fatigue is better avoided with the

contact surface compliance. For cutting tools the high hardness is important, but it is an insufficient condition. T. L. Oberle [7] found that the influence of elasticity (*E*) in combination with hardness (*H*) gives a more reliable indicator of wear resistance than hardness alone. This has been revised and expanded upon, in recent years by A. Leyland et al. [8,9]. They proposed that the parameter *H*/*E* ratio is proportional to the toughness of material. (2) The **environmental robustness**: most machines have interrupted operations, which add both regular and irregular temperature oscillations as well as corrosive and oxidative exposures of various length. This leads to 'tribochemical' reaction that has the considerable influence on both friction and wear [10]. The chemical reactions on the surfaces are strongly influenced by the high local pressures at asperities and the flash temperatures, which can be over 1000 °C [1]. (3) **Stable operation**: the stability of the friction loss in their contacts is critical for reliable and predicted operation over the broad variations of loads, speeds, temperatures and environments. (4) **Low friction coefficient <0.2** needs to be in the case of an effective solid lubricant. An irreversible deformation of the contact surfaces is likely to occur for friction values in excess of 0.2 [11].

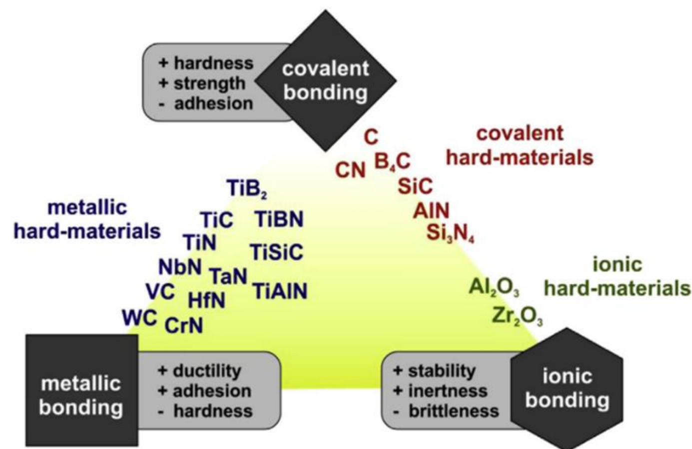


**Fig. 1.1.** Classification of hard ceramic materials according to their chemical bonding and the corresponding mechanical and physical properties. Modified by Mayrhofer et al. [12] after Holleck et al. [13].

These aforementioned requirements can be realized by combination of the proper composition of transitional metal nitrides (TMNs), and microstructural design i.e. by increasing the complexity and strength of grain boundaries [14]. The TMN films have very attractive mechanical and chemical properties such as high hardness, good abrasive and sliding wear resistance, and high temperature stability, as well as oxidation and corrosion resistance [12]. These attractive properties of the TMNs mainly arise from the strong covalent component to their chemical bonding, which can generally be considered as a mixture of metallic, ionic, and covalent contributions [12]. Furthermore, multiphase structures are expected to have interfaces with high cohesive strength, since different crystalline phases often exhibit different sliding systems and provide complex boundary to accommodate a coherent strain, thus preventing the formation of cracks, voids or defects [14]. Additionally, more information about the toughening microstructural design for films is given in the chapter 1.4.3 – Toughening approaches. A variety of hard materials can be used in nanocomposite film microstructural design. Figure 1.1 gives an overview of the classification of hard ceramic materials according to their chemical bonding and the associated change in properties [12]. The distinct metallic contribution causes electrical

conductivity, as well as a good adhesion and considerable ductility (as compared to ionic hard materials), in addition to the high hardness and phase stability, caused by covalent and ionic bonding components [12].

## 1.1. Friction

The friction coefficient ($\mu$) can be defined as the ratio of the friction force ($F_f$) to the normal force ($F_n$) = normal load $L$, i.e. $\mu = F_f/F_n$. The $F_f$ may be defined as the resistance encountered by one body in moving over another [5]. Simple explanation of friction at the macroscopic level is described by Guillaume Amontons and Charles-Augustin de Coulomb [15,16]. They observed that (1) the $F_f$ that resists sliding at an interface is proportional to the $F_n$, or force which presses the surfaces together, (2) the $F_f$ is independent of the apparent area of contact: A small block experiences as much friction as does a large block of the same material, so long as their weights are equal, and (3) the $F_f$ is independent of velocity for ordinary sliding speeds and roughness.

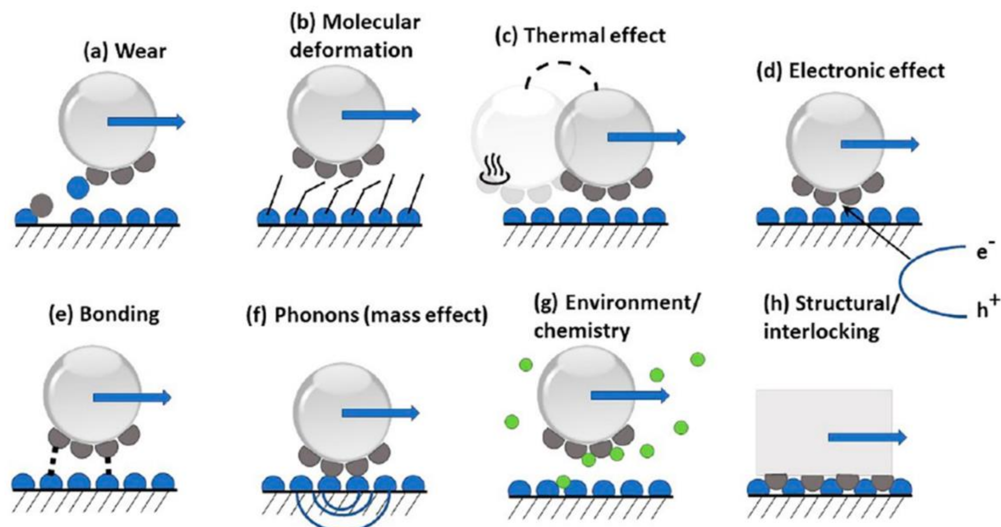


**Fig. 1.2.** Schematics representation of friction mechanisms of dissipation during sliding [17].

However, at the nanoscopic level, friction becomes far more complicated – different processes contribute to energy losses during sliding and thus lead to friction. Figure 1.2 illustrates some possible mechanisms of **frictional energy dissipation** and highlights the frictional response of the system. The frictional energy dissipation mechanisms can be briefly described as follows [17]: (a) **Wear** – energy is dissipated due to shear and removal of material from sliding surfaces and the wear-induced frictional losses are especially under conditions of high load, speed, and environmental effects; (b) **Molecular Deformation** – is associated with the elasto-plastic deformation of the large molecules present on or near the surface of sliding counterparts; (c) **Thermal Effect** – can be attributed to the thermal activation of the atoms to move around and across the interface as contacts are formed; (d) **Electronic Effects** – include charge generation, transfer and discharge. The static electricity buildup can influence friction between sliding surfaces, so electrostatic forces can increase friction; (e) **Bonding** (Chemical Bond Formation and

Breaking) – formation of chemical interactions at the asperity contacts (between sliding surfaces or top layer and substrate) cause the friction; (f) **Phonon Effects** (Mass Effect) – when heat is generated during sliding in the absence of wear, the energy dissipation on the atomic-level occurs to through lattice vibrations (so-called phonons), optical excitations (photons), electronic excitations (exoelectrons), etc. at near the surfaces of materials during sliding; (g) **Environmental/Ambient Chemistry Effects** – the surrounding environment, which contains specific gas (Air, nitrogen, etc.) and/or water, could significantly affect friction and wear by modifying the surface chemistry of the sliding surfaces; (h) **Structural Effects** – important in 2D materials; when the lattices of two ordered materials perfectly match one another, and are aligned in the direction of sliding at atomic-level, the interlocking and thereby strong adhesion and friction occurs. But real surfaces are not clean, and they are present small numbers of mobile atoms or molecules such as water or short-chain hydrocarbons at the interface.

## 1.2. Wear

The wear is the process of detachment of material from one surface. The wear from sliding surfaces generally occurs trough one or more of the following main mechanisms [18,19]: (1) **abrasive (fracture) wear** – hard counterface plows grooves into a softer surface, (2) **adhesive wear** – asperities from both surfaces in contact adhere, and material from the softer surface is sheared away as the counterface moves, (3) **fatigue (fracture) wear** – wear particles are detached due to cyclic crack growth of microcracks on the surface, and (4) **chemical wear** – wear particles are generated due to corrosion (oxidation) in a corrosive environment (e.g. humid air, etc.) by a chemical reaction. The fracture is a term describing failure of brittle material by a process starting from loss of cohesion between bond structures in the material, continuing as crack propagation and resulting in debris being liberated from the surface [19]. It should be noted that the cracking and wear of the film are mutually correlated phenomenon because crack (fracture) generation and propagation cause wear of the film. Moreover, the occurrence of the cracks leads to increase friction, science it provides an additional mechanism for the dissipation of energy at the sliding contact [5].

The wear rates ($k$) are quantified as the volume ($V$) of material removed by counterface normalized by the applied normal load ($L = F_n$) and the total distance of sliding ($l$) traveled by the wear counterpart. Typical $k$ values for solid lubricants with moderate wear resistance are between $10^{-6}$ and $10^{-5}$ mm$^3$/Nm [18].

### 1.2.1. Crack nucleation

The microstructures of films are, with few exceptions, never perfect. They include defects like dislocations, voids, pores, contamination, point or line crystal defects. The crack nucleation and initiation may take place according to several different mechanisms depending on the material microstructure, geometrical features and state of applied and residual stress. One possible mechanism for crack nucleation is that dislocations in a work-hardened region are piled up by shear stresses, resulting in a crack. In ceramic films typically with the columnar microstructure, the

cracks nucleate and propagate in the weakest place – between the columns [20]. Moreover, the film thickness and grain size play also important role. A coarser grained microstructure generally displays a lower cohesive strength as compared with a fine-grained microstructure. Thus, the fracture strength of the films increases with decreasing grain size and decreasing thickness [20].

## 1.3. Hardness

The hardness of the films is very important because influence the initiation of cracks and then wear. Higher is hardness of the films, higher is protection itself against scratching by a hard counterface or debris. Therefore, the hardness of protective films must be significantly higher than counterpart material. The hardness is not a physical quantity, is defined as resistance to localized plastic deformation induced by e.g. mechanical indentation. However, the materials (B, C, N and O based ceramics) with high strength (hardness) are less responsive to plastic deformations (see Fig. 1.3), i.e. are less ductile, which may result in brittle fracture due to crack initiation and/or propagation. In other words, the stronger (harder) is material, the less plasticity is available for (intrinsic) toughening. About toughening we will discuss in the next chapter (1.4.3) – Toughening approaches.

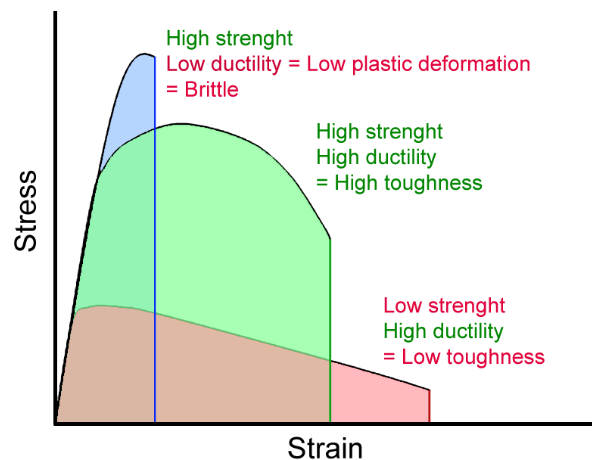


**Fig. 1.3.** Stress vs. Strain curves represent the difference between (i) high strength and brittle, (ii) high strength and ductile, and (iii) low strength and ductile materials. The hardness is proportional to strength.

The hardness of the film may be increased by following procedures: (1) **the compressive macro-stress** [21] – the hardness increases when the compressive macro-stress increases in the film. Compressive macro-stress is usually caused by defects in the film structure as vacancies, gas incorporation, interstitials, and dislocations, generated during the film growth process by energetic sputtered atoms, ions, and/or backscattered Ar neutrals (usually from high atomic mass target) at low sputtering-gas pressures [22]; (2) **the grain boundary strengthening** [23] – is described by Hall–patch relation (1.2), when the grain size ($D$) decreases (typically to ≤10 nm [24], see Fig. 1.4) to a size of the Frank–Read dislocation source, the dislocation cannot pile-up and propagate through the grain boundaries, the cohesive forces between the atoms and grains starts play significant role and then to strengthening of the films and their hardness enhancement occurs. Further decrease in the grain size leads to material softening, due to grain

boundary sliding; (3) **solid solution strengthening** [25,26] – adding of low content of another interstitial element (such as B, C, N, O and Si) or immiscible element into main element or into binary or ternary (or more complex) alloy or nitride system, leads to increase in the hardness, due to decrease grain size, (4) **the age hardening** – the hardness increases when the metastable nanocomposite, e.g. Ti-Al-N [12,27], is spinodally decomposed into c-AlN- and c-TiN-rich domains, when is exposed to high temperatures (≥800°C) where high atom diffusion occurs; and (5) **vacancy induced hardening** – due to pinning of dislocation at vacancies and thus inhibition of their motion [28,29], i.e. in substoichiometric $TiN_x$/MgO(001) ($0.67 \leq x \leq 1$) [30].

$$H(D) = H_0 + k\frac{1}{\sqrt{D}}; \qquad (1.2)$$

Where $H_0$ is hardness of single crystal or bulk sample, and $k$ is a constant.

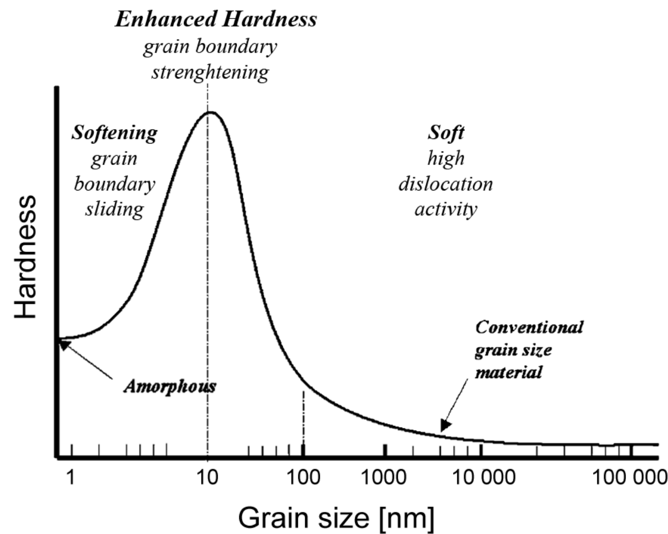


**Fig. 1.4.** Schematic illustration of coating hardness as a function of grain size [14].

It is important to note that aforementioned strengthening or hardening mechanisms that leading to high hardness, cause decreasing of the dislocation activity. In the absence of dislocations and grain boundary sliding the nanocomposites may show brittle behavior which means that the fracture strength (and hardness) is proportional to the elastic modulus of the material. The fracture stress of such material should then be determined by the critical stress $\sigma_c$ for the growth and deflection of microcracks, see eq. (1.3). However, one has to keep in mind that this model is very simplified. The mechanism of the toughening of nanocomposite ceramics is much more complex, including switching from intergranular cracking to transgranular cracking leading to crack deflection, and plastic zone shielding, etc [24]. About toughening of ceramic, we will discuss in the next chapter (1.4.3) – Toughening approaches.

$$\sigma_c = k_{crack}\sqrt{\frac{2E\gamma_s}{\pi a_0}}; \qquad (1.3)$$

where $E$ is the Young's modulus, $\gamma_s$ is the surface cohesive energy, and $k_{crack}$ is a constant which depends on nature and shape of the microcrack and kind of applied stress.

### 1.3.1. Nanocomposite films

The nanocomposite films comprise of at least two separated phases, a nanocrystalline phase with nanocrystalline (nc-) structure and a thin matrix phase, where the matrix can have either hard nanocrystalline or soft amorphous structure [14]. The general characteristics of nanocomposite film are that another material is homogeneously imbedded within a host material, result in formation of thin matrix phase that separate each nanocrystal of a host material. The thickness of the matrix phase must be 1–2 nm, i.e 1 monolayer (ML) [31]. In order to form such a biphasic system, both materials should must be immiscible (i.e., they must display thermodynamically driving segregation during deposition) and the cohesive energy at the interface between the both phases must be high [24]. The nanocomposite system, where nc-AlN grains are imbedded in a thin a-$Si_3N_4$ matrix, is schematically illustrated with Fig. 1.5. The nanocomposite films, due to very small (≤10 nm) nc- grains, exhibit remarkable high hardness, that significantly exceeding that is given by the rule of mixture [32]: $H(A_aB_b) = [a \times H(A) + b \times H(B)]/(a + b)$; where $H(A)$ and $H(B)$, and $a$ and $b$, are hardness and content of the pure A and B component, respectively. According to hardness the nanocomposite films can be divided into three groups [24,33]: (1) the hard films $H < 40$ GPa, (2) the superhard films 40 GPa $< H <$ 80 GPa, and (3) the ultrahard films $H > 80$ GPa.

At present, two groups of hard and superhard two-phases nanocomposite films are known: (1) nc-MN / hard phase (e.g. a-$Si_3N_4$, a-$TiB_2$, a-C, BN, etc.) [24], and (2) nc-MN / soft phase (e.g. Cu, Ni, Y, Ag, Au, etc.) [33]; where M = Ti, Zr, Hf, V, Nb, Ta, Cr, Mo, W, and Al.

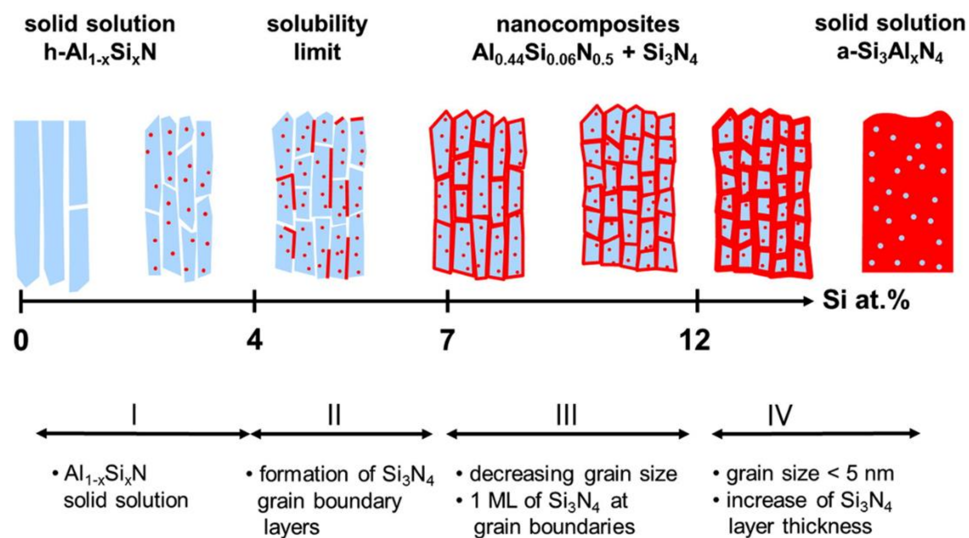


**Fig. 1.5.** Schematic diagram of evolution of the microstructure with increasing Si content over solubility limit in AlN crystal lattice in nanocomposite Al-Si-N system [36].

The most "dangerous" impurity within nanocomposite that limits their hardness is oxygen. High electronegativity of the oxygen causes weakening of the neighbor bonds thus forming fairly large defects, that are limiting the hardness of the nitrogen-based nanocomposites to about 35 GPa or even less, already at a relatively low concentration of ≥ 0.5 at.% [31,34,35]. Therefore, to deposit ultrahard nc-MN/a-$Si_3N_4$ films with $H > 80$ GPa, the oxygen impurity should be very low, up to 0.1 at.% O [31,34].

## 1.4. Toughness

In order to create a ceramic film with enhanced cracking resistance and enhanced wear resistance [3,8,9,37,38], the enhanced toughness of the film must be achieved. Toughness is defined as the ability of a material to absorb of deformation energy up to the fracture (cracks), i.e. means the material's resistance to fracture. Material toughness strongly depends on its strength and ductility or its ability to deform plastically [39]. In order to form tough material, the strength and ductility of such material must be high, see Fig. 1.3. Difference between the toughness and ductility is that: toughness is represented by area under stress-strain curve, while ductility is represented by maximum strain up to the failure point of the material. It should be noted, that as in the case of wear rate and friction, the both property of the toughness: strength and ductility are two mechanical properties that also tend to be mutually exclusive.

The toughness can be measured using the fracture-mechanics methods [40,41]: bending, buckling, scratching, indentation, nanoindentation, modified Vickers, tensile stress, or bending on the microcantilever beam [42], which evaluate the critical value of a crack-driving force, for example, the fracture toughness $K$, or critical energy (strain-energy) release rate $G$.

### 1.4.1. $H/E$ ratio ≈ toughness

The hence, for describing the film elasticity and toughness, only $H$ parameter is insufficient. Leyland et al. [8,9] proposed the parameter $H/E^*$ ratio where the higher is $H/E^*$ ratio, the toughness of a material is higher. The $H/E^*$ ratio is described in terms of "elastic strain of failure"; where $E^* = E/(1-v^2)$ is the effective Young's modulus, $E$ is the Young's modulus and $v$ is the Poisson's ratio. In order to achieve high toughness, i.e. large $H/E^*$ value, the hardness of the films should be enhanced, by aforementioned strengthening or hardening mechanisms, while maintaining low elastic modulus.

### 1.4.2. $B/G$ ratio and Cauchy pressure $C_{12} - C_{44}$ ≈ ductility

While $H/E^*$ ratio describes the material elasticity and is proportional to the material toughness, both quantities $B/G$ ratio – Pugh [43] and Cauchy pressure $C_{12} - C_{44}$ – Petiffor [44] classifying cubic material whether is ductile; where $B$ and $G$ are bulk and shear modulus, respectively and $C_{12}$ and $C_{44}$ are elastic tensors. Particularly, the shear elastic constant $C_{44}$ is proportional to the hardness of the material, and negative its value corresponds to mechanical instability of such material [45]. A material is considered ductile if it has $B/G \geq 2.0$ with positive Cauchy pressure $C_{12} - C_{44} > 0$ [44]. It should be noted that $G \approx H$, because during the indentation, the material is subjected to shear. Both quantities $B/G$ ratio and Cauchy pressure $C_{12} - C_{44}$ can be calculated by using the density function theory (DFT) [46]. Example of DFT results from binary TMN and ternary ($M_{0.5}{}^1M_{0.5}{}^2N$) metal nitrides with cubic structure is shown in Fig. 1.6; where M = Ti, Zr, Hf, V, Nb or Ta. The Fig. 1.6 shows that TMNs (with Ta, Nb, and V) with the high amount of metallic bonding, i.e. high number of valence electrons per (metal) atom (VEPMA), exhibit high ductility [47]. Above that, it was found that addition of Mo or W into ternary TMN also leads to enhance of material ductility [39,48]. Thanks to these DFT calculations new ternary or

quaternary TMN films with enhanced ductility and then enhanced toughness has been predicted, see Refs. [39,45,49,50].

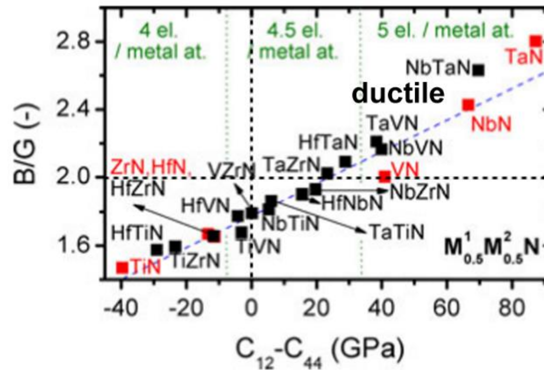


**Fig. 1.6.** Bulk to shear modulus ratio (*B*/*G*) and Cauchy pressure ($C_{12}$ - $C_{44}$) of material that represents the ductility [47].

S. Jhi et al. [28,51] recently reported that the maximum hardness of cubic TMN is achieved at a valence electron concentration (VAC) of ~8.4, it corresponds to binary or ternary Ti, Zr and Hf nitrides, carbides or carbonitrides, due to complete filling of the shear-resistive p–d–$e_g$ orbitals, while shear-sensitive d–$t_{2g}$ TM/TM states remained unoccupied. At higher VEC, the shear sensitive d–$t_{2g}$ orbitals begin to be filled, thus reducing the shear-resistance of the material and, in turn, reducing its hardness, while ductility increases. K. Balasubramanian et al. [45] more recently reported that maximum ductility and toughness are predicted for alloys with VEC between 9.5 and 10.5 – it corresponds to V, Nb and Ta nitrides or Cr, Mo and W carbides. It should be noted that it applies: VEPMA ≈ 1/2VEC. T. Reeswinkel et al. [52] found that lower the $C_{44}$ lower the shear strength of the material and then the friction coefficient is lower. According to K. Balasubramanian et al. [45] calculations, low friction materials (with $0 < C_{44} \leq 60$ GPa) should be: CrN, CrCN, VCrN, RuC, CoC, TaN, TaWN, NbMoN, MoCN, and WCN.

### 1.4.3. Toughening approaches

The toughness (≈ cracking resistance and wear resistance) depends not only on mechanical properties of the film, but strongly depends on the structure, microstructure, phase (metallic or ceramic) and macro-stress in such film. Recently, R. Ritchie [53] classified the toughening approaches in two types: **extrinsic** and **intrinsic**, schematically illustrated with Fig. 1.7. In order to achieve enhanced toughness, enhanced cracking and enhanced wear resistance, both extrinsic and intrinsic approaches should be achieved.

**Extrinsic toughening** [41,42,53–56] involves obstruction of the crack propagation (shielding) after its initiation (nucleation). Extrinsic toughening is the most used solution for achieving of the toughness in the hard-ceramic films. For example: (1) the prestressing by **compressive macro-stress** that prevents cracks formation by their closing [57], (2) incorporation of the **second phase** to cause crack deflection, crack bridging, crack splitting and fiber pullout at the grain boundary [58] or fiber/matrix interface [57] of (i) the chevron-like microstructure [42],

the nanograins, the nanocolumns, the nanocomposite structure (see Fig. 1.8a) composed of brittle ceramic nanograins in ceramic tissue phase (matrix) [36,59,60], the carbon nanotubes (see Fig. 1.8c) [61] or (ii) at the amorphous structure, and/or (iii) at the interface of the layers in the multilayer system (see Fig. 1.8b) [13,58,62,63] with ceramic/ceramic interface (with the same or different material layers constituents with different elastic modulus [64], different hardness or different macro-stress), or superlattice [65], (3) **phase transformation** (see Fig. 1.8d) from low-phase volume to high-phase volume leads to obstruct crack propagation or to healing the crack (e.g. in partially stabilized zirconia – transformation from tetragonal to monoclinic $ZrO_2$ structure is accompanied by a volume expansion of ~4 % [66]). Another way to enhance cracking resistance, is a very low film thickness (50–500 nm) [67,68]. The very thin films can exhibit (1) a fewer macro-defects leading to crack initiation and (2) a lower tensile strain applied to the film during the bending due to lower thickness.

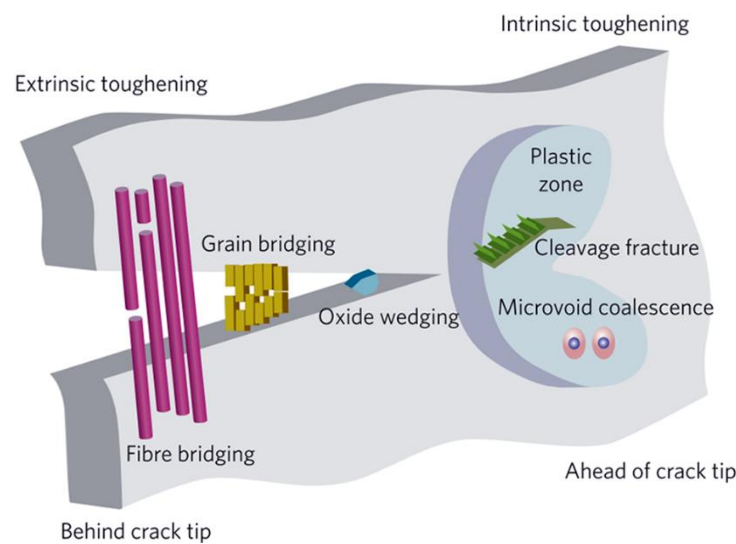


**Fig. 1.7.** Schematic illustration shows how strength and fracture behavior can be considered in terms of intrinsic (plasticity) versus extrinsic (shielding) toughening mechanisms associated with crack extension [53].

**Intrinsic toughening** suppresses crack initiation due to plasticity of the film [41,53], and plays dominant role in the ductile films. Let's recall: (1) the ductility depends on the amount of a metallic bonding in the films, and increase with increasing number of valence electron per (metal) atom [47], and (2) the film with cubic structure is ductile when $B/G \geq 2.0$ and $C_{12}$ - $C_{44}$ > 0. Intrinsic toughening can be achieved in the films within (1) nanocomposite structure, where addition low amount of the non-soluble (in the major phase) soft metallic phase into the brittle ceramic major phase resulting in formation of the nanocomposite structure (see Fig. 1.8a), (2) multilayer system ceramic/metal (see Fig. 1.8b). Enhancement of a ductility (amount of metallic bonds) in the films can be well achieved by either adding of (i) a non-soluble metals in the TMN (see Fig. 1.8e) such as 10.B group (Ni, Pd and Pt) and/or 11.B group (Cu, Ag, Au), and/or (ii) a soluble metals in TMN such as V.B (V, Nb and Ta) group and/or VI.B (Cr, Mo and W) group [39,47,69] resulting in high number of VEPMA (see Fig. 1.6), e.g. adding of Ta into Ti-Al-N [70]. Additionally, the ductility in the cubic TMN can be increased with decreasing the

N/Me ratio, where increasing concentration of N vacancies in $TMN_x$ leads to increases the density of metal–metal d–d orbitals, which, in turn, decreases the shear modulus [51].

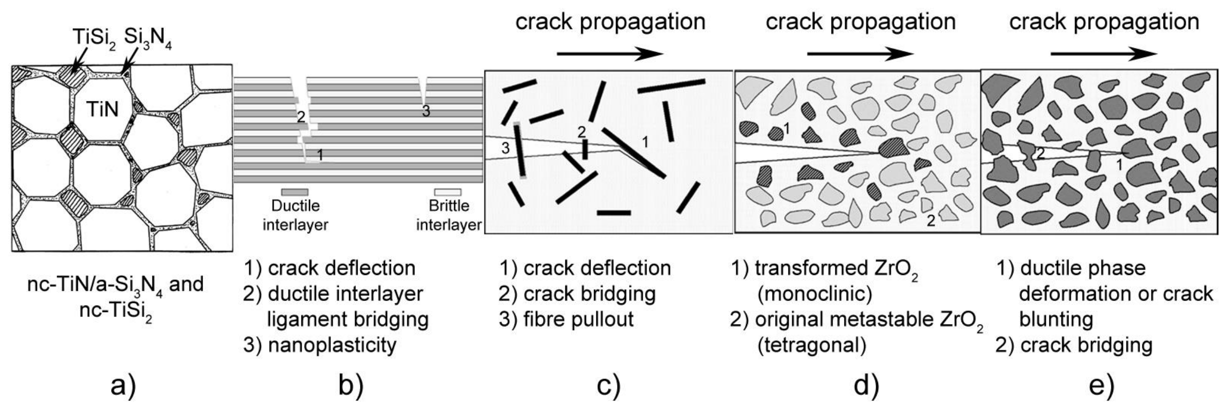


**Fig. 1.8.** Schematic illustration of toughening approaches: (a) nanograin (nanocomposite, e.g. nc-TiN/a-$Si_3N_4$ and nc-$TiSi_2$) structure toughening, (b) multilayers toughening, (c) fiber or nanotube toughening, (d) phase transformation toughening, and (e) ductile phase toughening [54].

# 2. Designing of films with enhanced cracking resistance

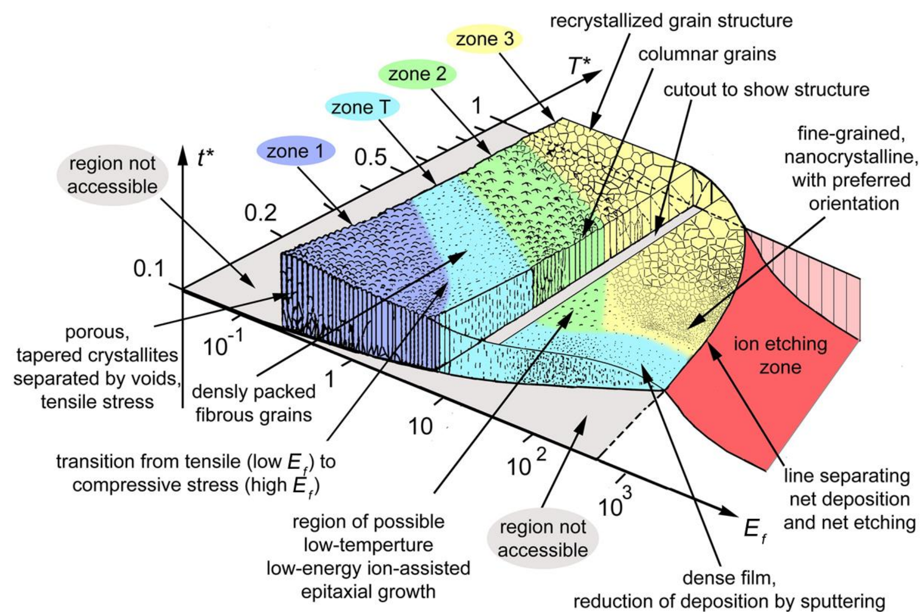


**Fig. 2.1.** Structure zone diagram applicable to energetic deposition: the generalized temperature $T^*$, the normalized energy flux $E_f$, and the film thickness $t^*$ [80].

Recently [55,71–78], in our laboratory, it was found that the ceramic (TM oxides, nitrides or oxynitrides) films with enhanced cracking resistance exhibit combination of the following conditions: (a) **compressive macro-stress** ($\sigma < 0$), is usually higher than -1 GPa, which suppress the crack propagation, (b) **non-columnar, dense, fine-grained or amorphous microstructure**, which is formed in the transition zone (zone T, see Fig. 2.1), unlike columnar where boundaries between the columns are the weakest place for the crack initiation and propagation (see, Fig. 2.2), and (c) high toughness, expressed by elastic strain to failure ratio $\boldsymbol{H/E^* > 0.1}$ and elastic recovery $\boldsymbol{W_e > 60}$ **%**, especially in the hard ($H > 15$ GPa) ceramic materials which are deformed predominantly elastically before cracking. Moreover, recently it was proved that both

quantities $H/E^*$ and $W_e$, describing the elastic deformation of the ceramic films, are strongly influenced by $\sigma < 0$; the higher is compressive macro-stress, the higher is value of both $H/E^*$ and $W_e$ [79]. It means that in such cases, the compressive macro-stress is one of the main toughening approaches in the films, which cause enhanced cracking resistance.

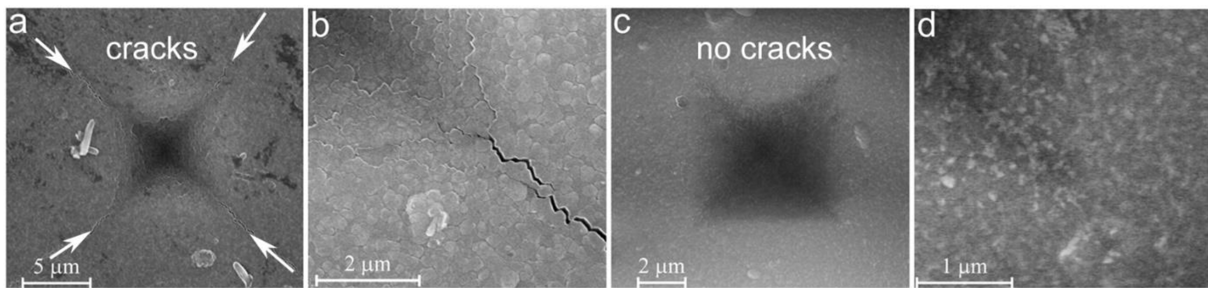


**Fig. 2.2.** Crack propagation after the indentation test at high load applied on to the film with (a,b) columnar microstructure, and (c,d) non-columnar dense and fine-grained microstructure [81]. Figures (b) and (d) represents enlarged right-lower corner of (a) and (c) imprint, respectively.

The films with enhanced resistance to cracking are considered to those, which do not crack after (1) the indentation test (see Fig. 2.2) at loads up to 1 N, where the penetration depth of an indenter exceeds 50 % (up to 100 %) of the films thickness, using a Vickers diamond indenter, nor (2) the bending test, where a tensile strain exceeds 1.0 % (up to 2.5 %).

These aforementioned conditions, for enhancement cracking resistance of the films, can be achieved by: (1) the addition of low content of one element into the base material, and/or (2) the optimization of the deposition parameters of the sputtered films.

In the first case, the doping of the TM or TMN by low content (approximately between 5 and 10 at.%) of interstitials B [26], C [26], N, O [77], and Si [36,82,83] elements results in the grains refinement of the TM or TMN in the film. Example, the addition of the Si into the AlN [36,83] leads to change of the microstructure (see Fig. 1.5) from (i) crystalline with columnar AlN grains (Si <7 at.%), through (ii) nanocomposite where a nanocrystalline (nc-) AlN grains are embedded in an amorphous (a-) $Si_3N_4$ matrix (Si 7–12 at.%) to (iii) amorphous (Si >12–15 at.%).

In the latter case, the deposition parameters related to energy delivered to growing film affect the film density, structure, microstructure [84,85], texture orientation [84,85], grain size and macro-stress [86]. This energy, according to Thornton [87] structure zone diagram modified by Anders [80] is shown with Fig. 2.1, in simple form, can be described by two variables: (1) a heating ($T^*$) that contains the sum of (i) homologous temperature ($T_h = T_s/T_m$; where $T_s$ is the substrate temperature and $T_m$ is the melting temperature of deposited film) and (ii) temperature from potential energy of energy-charged particles [80], and (2) the energy flux ($E_f$) that contains (i) a product of kinetic energy of arriving ions $E_i$ [85,88] and ratio of ion fraction to total fraction of arriving particles $n_i/n_a$ to film and their momentum transfer to growing film [89–91] and (ii) the product of kinetic energy of fast neutrals $E_n$ [89–91] that contains sputtered atoms and reflected atoms ($Ar^0$, $N^0$) from the target (significant in the case of high-mass sputtered targets) and ratio of sputtered atoms and reflected neutral atoms to total fraction of arriving particles

$n_0/n_a$ to film and again their momentum transfer to growing film. In particular, higher is the energy of the $E_i$, the higher can be the compressive macro-stress in the film [92], due to formation of the defects in its structure [22].

## 3. Al-Si films

In a term of globally reducing fuel consumption and reducing a production of the greenhouse ($CO_x$) gases, it is important not only increasing the engine efficiency, but also reducing weight in the aerospace and automotive applications. For several decades, the aluminum based alloys have been widely used to produce the engine block and engine parts due to their high strength over weight ratio [93].

Aluminum (Al) is a very soft and ductile metal with very low melting point $T_m$ = 660 °C. The values of hardness ($H$) and effective Young's modulus ($E^*$) of a bulk Al are low: $H_{Al}$ = 0.5 GPa and $E^*_{Al}$ = 75 GPa, respectively; $E^* = E/(1-\nu^2)$ where $E$ is the Young's modulus and $\nu$ is the Poisson's ratio. These low properties of the aluminum are due to its faced-centered cubic (fcc) crystal structure bound by weak metallic bonding Al–Al [94,95], where last three electrons are delocalized ([Ne] $3s^2 3p^1$) and involved in electrical conductivity. Thanks to this, the Al exhibits fourth highest high electrical conductivity of $3.77 \times 10^7$ S/m from metals. Moreover, Al has remarkable low density 2.70 g/cm$^3$ and ability to resist corrosion due to its passivation phenomenon – formation of the protective thin $Al_2O_3$ scale on its surface.

Silicon (Si) is a hard and brittle tetravalent metalloid (= properties between a metal and non-metal) with high melting point $T_m$ = 1414 °C. The values of $H$ and $E^*$ of bulk Si are high: $H_{Si}$ = 13 GPa and $E^*_{Si}$ = 150 GPa [96], respectively. These well properties of silicon are due to its face-centered diamond cubic structure bound by strong covalent bonding Si–Si [94,97]. In the Si ([Ne] $3s^1 3p^3$) one electron can be delocalized (at $T > 0$) and causes very low electrical conductivity of $4.35 \times 10^{-4}$ S/m, while four (at $T > 0$ – three) electrons are localized and involved in covalent bonds. Density of Si: 2.40 g/cm$^3$ is even lower than that of Al.

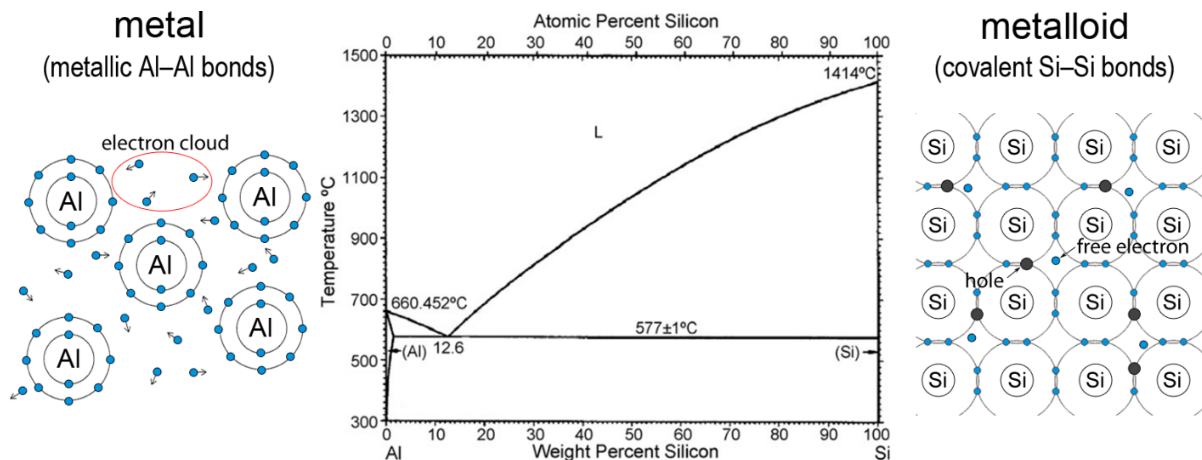


**Fig. 3.1**. The Al-Si binary alloy phase diagram [93], and schematically illustrated Al and Si bonding structures.

The equilibrium aluminum-silicone (Al-Si) alloy phase diagram shown with Fig. 3.1, is composed of two solid solutions [98]. There is apparent that Al-Si alloy does not form beta phases,

intermetallic phases and/or silicides (MSi, $M_2Si$, $MSi_2$, etc.); where M is metal. The maximum solubility of Si in Al is 1.5 at.% at the eutectic temperature (577 °C) and it decreases to 0.05 at.% at 300 °C [98]. The maximum solubility of Al in Si is 0.016 at.% at 1190 °C [98]. The solubility of Si in Al can be greatly extended by rapid liquid quenching [99]. This can be achieved by magnetron sputtering, due to its non-equilibrium process, where the alloy is: (1) extremely fast heated at the atomic level and then (2) extremely fast cooled down to RT ($10^{14}$ °C/s) [100,101]. Silicon reduces thermal expansion coefficient, friction coefficient (from 0.6 to 0.4) [102], increases corrosion and wear [102] resistance of the Al-Si [93]. Recently, the Al-Si coatings were prepared by various deposition techniques, such as: plasma spraying [102], cold spraying [103], electro spark deposition [104], selective laser melting [105–107] and magnetron sputtering [108]. In the aforementioned works, the highest hardness was 5.9 GPa (HV = 600) achieved at 70 at.% Si [102] or even 23.6 GPa at 25.2 at.% Si [108]. Enhancement of the hardness (>13 GPa) is very important in order to achieve higher scratching resistance and increase the wear (cracking) resistance of Al-Si films. Instead of solid solution strengthening – alloying of Al-Si alloy by Mg, Mn, Fe, Ni, Cu, etc. [93,109], the high hardness of Al-Si alloy can be achieved by: (1) adding higher amount of Si according to rule of mixtures (ROM) [32] – disadvantage of this approach is limitations by hardest compound (Si: 13 GPa); and/or (2) the grain boundary strengthening [23] – described by Hall–patch relation: when the grain size decreases to ≈ 10 nm, the dislocations cannot pile-up and propagate through the grain boundaries and then leads to increase of the $H$ to maximum values.

The main aim of this study is to find the condition under which the Al-Si alloy films exhibit the highest values of its $H$, $H/E^*$ and elastic recovery $W_e$. No one in more detail investigates the effect of the Si content in wide range and deposition parameters on the structure, microstructure and mechanical properties of the Al-Si films. In addition, the deposition parameters were investigated in terms of the energy delivered into the Al-Si films by (i) the substrate heating, and by (ii) the ion bombardment of the films. Particularly, the influence of the structure, microstructure and crystallite size on the mechanical and tribological properties of the Al-Si films were investigated. The cracking resistance evaluated by an indentation test and friction and wear using 100Cr6 ball of the films were investigated as well.

# 4. Al-Si-N films

Aluminum silicon nitride (Al-Si-N) films are *flexible, hard and multifunctional ceramic nanocomposite*, that combine recently studied unique combination of mechanical and physical properties such as: high hardness up to 34–39 GPa [83,110], thermal stability and oxidation resistance exceeding 1000 °C (previous results from our department) [111], high transparency [36,112,113], refractive index (2.00–2.16), good adhesion and protection of the substrate to cracking, wear, impact and corrosion [81,110,114–118]. A. Pélisson-Schecker [36,83] found that the addition of Si into the AlN leads to change of the microstructure from (i) crystalline with columnar AlN grains (Si <7 at.%), through (ii) nanocomposite, where a nanocrystalline (nc-) AlN grains are embedded in an amorphous (a-) $Si_3N_4$ matrix (Si 7–12 at.%) to (iii) amorphous (Si >12–15 at.%). The Al-Si-N films exhibit wide range of application from common

users to spacecraft, e.g.: (flexible) displays in the smartphones, watch, telescopes, solar cells, optical sensors, windows, lenses, mirrors, etc.

The Al-Si-N films were extensively studied and prepared using various methods of the deposition process such as: low pressure chemical vapor deposition (LPCVD) [119], filtered [59] and unfiltered cathode arc evaporation [110,115], DC magnetron sputtering (MS) [36,60,83], AC pulsed MS [81,84,111], radio frequency (RF) MS [112], high power impulse MS (HiPIMS) [113,120], and bipolar pulsed MS [116,117].

Previous our studies [81,84] dealt with the influence of the mechanical properties ($H$, $H/E^*$, $W_e$ and macro-stress $\sigma$), on the cracking resistance of the Al-Si-N films sputtered using Al/Si (90/10 at.%) target, but the influence of the mechanical properties on the wear resistance was not so far experimentally investigated. Recently studied tribological properties of the Al-Si-N films revealed that the films with Si content: (1) 6.9–8.1 at.% Si [110] exhibit the friction coefficient $\mu = 0.5–0.7$ and wear rate $k = 0.6–1.9 \times 10^{-6}$ mm$^3$/Nm using WC ball, and (2) 9 at.% Si [115] exhibit $\mu = 0.85$ and 0.67, and $k$ = not measured and $k = 27.2 \times 10^{-6}$ mm$^3$/Nm using steel ISO 683/13 ball and $Al_2O_3$ ball, respectively. But there is still lack in understanding of the origin of the high $k$ of the Al-Si-N films, even in the case of their high values $H \geq 30$ GPa and $H/E^* \geq 0.1$.

Recently in our department [55,71–78] it was found that the films with: (i) non-columnar, dense and void free microstructure and (ii) $H/E^* > 0.1$, $W_e > 60$ %, and (ii) compressive $\sigma < 0$, should exhibit an enhanced resistance to cracking. But the conditions under which the films should be resistant to wear were not so far clearly determined.

The main aim of this study is to show how (1) the elasticity parameters $H/E^*$ and $W_e$, and (2) the structure and microstructure, affects the resistance to wear of the Al-Si-N films prepared with different Si content. Moreover, the dry nitrogen 5 % and moist environment 82 % is used in order to assess the wear resistance of the Al-Si-N films in different environment conditions.

## 5. W films

Tungsten (W) [121] exhibits the highest melting point (3422 °C) amongst pure metals and is one of the hardest transition metals (6.7 GPa as a bulk material and up to 32.2 GPa [122] as a nanocrystalline film). These superior properties of the tungsten are due to its relatively covalent character caused by half-filled d orbital ([Xe] $4f^{14}5d^5 6s^1$). Thanks to these properties, tungsten is very attractive for combinations with other elements (B, C, N, S, etc.) in binary (W-N [123,124], W-C [125–127], W-S [128]) and ternary (W-S-C [129–131], W-S-N [132–134], W-B-N [135], W-C-N [136,137]) systems which exhibit very interesting mechanical and tribological properties such as a high hardness, low friction coefficient ($\mu$), etc. Tungsten is also widely used as a doping element of DLC coatings, improving their hardness and high-temperature tribological properties [138–141] at preserved low $\mu$ and high wear resistance. Moreover, tungsten is widely used in the microelectromechanical systems (MEMS) [142], and is considered

the best candidate as plasma facing material in both magnetic and laser fusion reactors [143,144].

Mechanical properties of W bulk or W film depend on the type of preparation (powder metallurgy, arc cast, electron beam melted, zone refined, chemical vapor deposition [CVD], physical vapor deposition [PVD] – magnetron sputtering [121]). The summary of the mechanical properties of the deposited W films in recent publications [122,145–148] and W bulk is given in Table 5.1. Table 5.1 shows that the mechanical properties of the W films are strongly influenced by the phase, microstructure (crystallite size $D$), and compressive macro-stress ($\sigma < 0$).

W crystallizes in both stable α- and metastable β-phases, with different properties. In the case of W films deposited by magnetron sputtering, the phase may strongly depend on the deposition parameters and impurity content (O > 14 at.%  [149–152]). For example, the α-phase was predominantly found at low argon pressures 0.2–1.0 Pa, while β-phase is formed at high pressures >3 Pa [148].

Tungsten metal is stable in dry and humid air only at the moderate temperature. It starts to oxidize at about 400 °C [153]. The oxide layer is not dense and does not offer any protection against further oxidation. Above 700 °C the oxidation rate increases rapidly, and above 900 °C, sublimation of the oxide takes place, resulting in catastrophic oxidation of the metal. Any moisture content of the air enhances the volatility of the oxide [121].

**Table 5.1** Comparison of the mechanical properties of W films or bulk achieved elsewhere. Where $h$ is the thickness of the film, $\sigma$ is the macro-stress in the film, $D$ is a crystallite size in the film, and $P_{ta}$ is average target power (per period).

| Ref. | material | phase | substrate | $h$ [nm] | $H$ [GPa] | $E^*$ [GPa] | $H/E^*$ | $\sigma$ [GPa] | $D$ [nm] | $P_{ta}$ [W] | power supply |
|---|---|---|---|---|---|---|---|---|---|---|---|
| [145] | Bulk | α-W | | | 3.9 | 411 | 0.009 | | | | |
| our exp. | Bulk | α-W | | | 6.7 | 410 | 0.016 | | | | |
| [148] | Film | β-W | Si (100) | 500–1 310 | 4–8 | | | | 5–12 | 50–300 | DC |
| [148] | Film | α-W | Si (100) | 300–820 | 12–14 | | | -1 | 40–70 | 50–300 | DC |
| [147] | Film | α-W | Si (100) | 2 000 | 14 | 350 | 0.040 | -4 | | 48 | DC |
| [147] | Film | α-W | steel | 1 800 | 15 | 340 | 0.044 | < 0 | | 47 | DC |
| our exp. | Film | α-W | Si (100) | 2 230 | 17.2 | 292 | 0.059 | -2.8 | 30 | 200 | DC |
| our exp. | Film | α-W | Si (100) | 3 000 | 21.5 | 296 | 0.073 | -2.6 | 14 | 600 | AC |
| [122] | Film | α-W | Si | 400 | 23.2 | 251 | 0.092 | < 0 | 66.8 | 100 | DC |
| [146] | Film | α-W | Si (100) | 460 | 24.5 | 400 | 0.061 | -0.9 | 32.5 | 100 | DC |
| [122] | Film | α-W | Si | 400 | 32.2 | 289 | 0.111 | < 0 | 39.5 | 100 | HiPIMS |

The main aim of this study is to find the conditions under which the W film exhibits enhanced hardness. To deposit the films a classical DC power supply with a low-density discharge, or AC unipolar pulsed power supply with a high-density discharge was used. The effect of the deposition conditions on the structure, microstructure and mechanical properties of the W films

was investigated in detail. The key problem of the deposition of several microns thick W films is their very high compressive macro-stress (up to 4 GPa) and their adhesion to the substrates. Therefore, the conditions of the substrate plasma etching were investigated as well.

# 6. Ti-W films

Beta titanium bulk alloys are widely used in biomedical application and aerospace due to their light weight, low Young's modulus, high strength excellent biocompatibility, ductility and corrosion resistance and these properties can be tuned by alloying of Ti with various elements [154,155]. These properties depend on the chemical composition and phase stabilization of the Ti alloy. The elements that stabilize β-Ti phase are denoted to "stabilizers". It is well known that β-Ti stabilizers β-Ti(Me), empirically obtained, in a bulk titanium alloy materials are: Me = V, Nb, Ta, Cr, Mo, W, Mn, Fe, Co, and Ni [156].

**Stabilizing β-Ti phase in films deposited by magnetron sputtering**

The β-Ti films represent a new group of advanced films with unique aforementioned properties. The β-Ti films are composed of the stabilized high-temperature (high-T) β-Ti phase with body centered cubic (bcc) crystal system which differs from the low-temperature (low-T) α-Ti phase with hexagonal (h) crystal system.

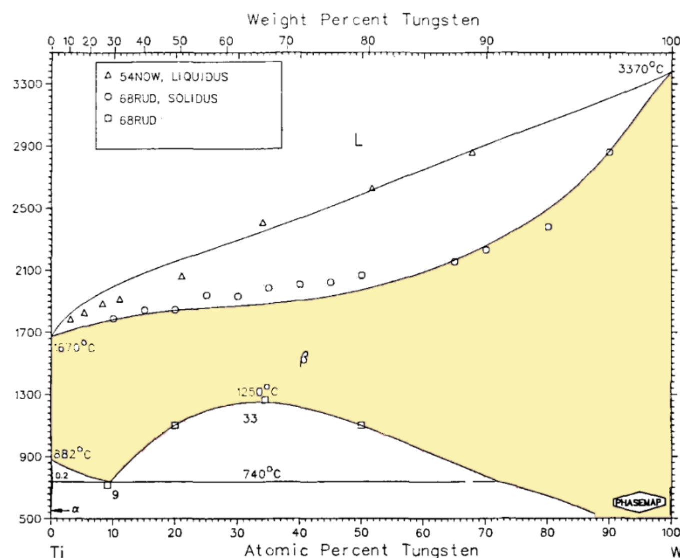


**Fig. 6.1**. Phase diagram of the Ti-W [157] alloy shows region of temperatures and compositions (yellow region) in which high-T β-phase alloy with the bcc structure, i.e. the high-T β-Ti(W) alloy can be formed.

It is well known which elements are β-Ti stabilizers [156], however, it is not clear why only certain elements can stabilize the β-Ti phase. From binary phase diagrams (Ti-W, see Fig. 6.1) it can be clearly seen that in order to stabilize the β-Ti phase, the bulk material should be quenched from the beta-phase field [154] (see yellow region). Then, while cooling to room temperature, the second phase (usually α-phase) will precipitate on the grain boundaries of β-phase, because β-phase is metastable [156]. This means that in order to deposit β-Ti phase film with bcc crystal structure, three main conditions should fulfill: (1) stabilizer must have a very

similar crystal structure as β-Ti has, i.e. bcc, (2) the material of the created film must be heated to high temperatures lying in the regions of the phase diagrams of alloys and compounds where the β-Ti of the alloy or compound material is thermodynamically stable, see Fig. 6.1, and (3) the created β-Ti film must be rapidly quenched down to room temperature (RT). The first condition is always fulfilled when the proper element with the proper crystal structure is chosen. The second and the third conditions may be also fulfilled by using the magnetron sputtering process, which take place at the atomic level, i.e. are formed by condensing atoms. In this process the condensing atoms and bombarding ions deliver into very small regions of atomic size the sufficient amount of energy $E = E_{bi} + E_{fn}$ leading to extremely high heating in the close their incident vicinity and then immediate extremely fast cooling down to the deposition temperature. The energy $E$ delivered into the growing coating by the bombarding ions $E_{bi}$ (tens of eV) and/or the condensing fast neutrals $E_{fn}$ (several eV) into very small areas of about 0.04 nm$^2$ is very high (1 eV = 11 600 K); the energy $E_{fn}$ can be dominant at the low sputtering gas pressures $p < 0.2$ Pa.

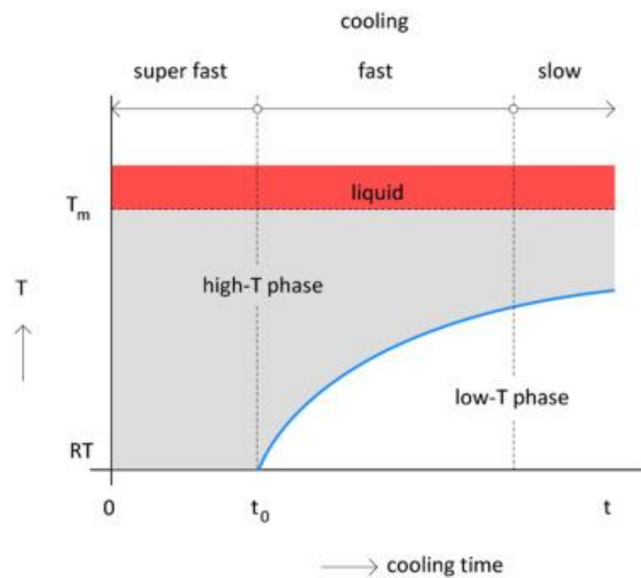


**Fig. 6.2**. Schematic illustration of the structure of a solid material (film) as a function of the temperature $T$ (between the melting temperature $T_m$ and RT) and the cooling time $t$ [101].

From aforementioned stabilizers, the β-Ti films were recently prepared by magnetron sputtering: Ti-Nb [158–162], Ti-Ta [163,164], Ti-Cr [101,165–168], Ti-W [169] and [101] – this work, Ti-Fe [166]. Moreover, an addition of more alloying elements into the Ti, can lead to formation of the super-elastic material or film called “Gum metals”, firstly elaborated by Satio et al. [170]. This kind of materials excel in their high strength and low Young’s modulus. Examples of such films are: Ti-Nb-Zr [171], Ti-Nb-Zr-Ta [172], and Ti-Nb-Zr-Ta-(O) [173] exhibiting high elasticity expressed by hardness to effective Young’s modulus ratio $H/E^*$ exceeding 0.1. The Ti-Zr-O [77] films deposited in our laboratory exhibit very similar mechanical properties such a Gum metals, i.e. $H$ up to 16 GPa, $H/E^* = 0.105$ at the O content of 15 at.%. However, there is no information why these elements: V, Nb, Ta, Cr, Mo, W, Mn, Fe, Co, and Ni stabilize the β-Ti phase. Also, there is no explanation how the high temperatures are necessary to reach the β-Ti phase region in the phase diagrams of binary alloys are achieved.

Figure 6.2 shows schematically how the structure of the material, after being cooled down from an initial very high temperature above the melting temperature $T_m$, depends on the final temperature $T$ and the cooling time $t$. From this figure it is seen that the β-phase films stable down to RT can be formed only in the case when the cooling of the created material is very fast, i.e. when the cooling time is very short $t \leq t_0$; here $t_0$ is the maximum time at which the β-phase film exhibits no conversion to the low-T α-phase film. In the case when the cooling is slower, i.e. $t > t_0$, a two-phase film, composed of both the high-T and low-T phases, is formed. The content of the low-T α-phase in the coating increases with increasing cooling time within which the β-phase is partially converted (transformed) into the α-phase with different crystal structure than that of the β - phase.

The key problem in the formation of the stable β-Ti phase film is, however, their thermal stability, because the β-Ti phase film is metastable and has tendency to its conversion of the stabilized β-Ti(Me) phase into a two α-Ti phase and β-Ti(Me) phases during the post-deposition thermal heating (annealing). Therefore, investigation the thermal stability of the β-Ti films is very important from the point of view of its practical application, and to find the maximum temperature or temperature range at which the conversion of the β-Ti phase occurs, is also important.

# 7. $WN_x$ films

Tungsten nitride ($WN_x$) belongs to a class of refractory metal nitrides and exhibits excellent combination of mechanical properties (hardness over 40 GPa and high elasticity expressed by high ratio $H/E^*$ over 0.1 [123,124,174]), good chemical stability, excellent adhesion on steel substrates [174–176] and good tribological properties (wear resistance) [123,124,177]. Therefore, $WN_x$ constitutes a potential candidate for protective films of automotive engine parts and structural components, etc. $WN_x$ film is thermally stable up to 800 °C in $N_2$ atmosphere and starts oxidize at temperatures above 400 °C in air [153,178,179]. The oxidation resistance is very important in the cutting tools in dry and high-speed machining, where the flash temperatures can be over 1000 °C [1].

However, the development of stable harsh-environment protective films requires the investigation of the film oxidation and its effect on the tribological properties. There are several studies [124,131,135,141,180,181] dealing with tribological properties of W-based films at high temperatures ($T$). Figure 7.1 shows a review on the corresponding friction coefficient ($\mu$) values obtained in a range of testing conditions including relative humidity of 20–50%, normal loads of 3–5 N, sliding distance of 37–188 m, sliding velocity of 2.1–12 cm/s, etc. The figure shows that hard ($H \geq 20$ GPa) W, $WN_x$ and $WN_x$-based films exhibit qualitatively similar concave $\mu(T)$ dependencies, at significantly higher $\mu$ values compared to those achievable for soft ($H \leq$ 10 GPa) $WC_x$ and $WC_x$-based films with dominant sp$^2$ (graphite-like) bonds.

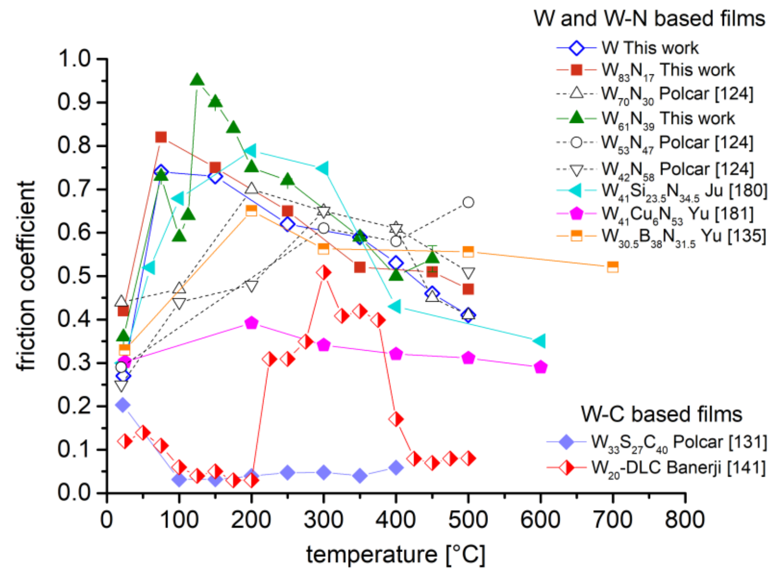


**Fig. 7.1.** Comparative study of the friction coefficient values at high test temperatures of W, W-N and W-C based films found in literature [202].

The main aim of this study is to investigate the oxidation and temperature-dependent tribological properties of $WN_x$ films measured using long test time (333 min) and sliding distance (1000 m) in a wide range of compositions (N content from 0 up to 60 at.% , i.e. $x$ = [N]/[W] up to 1.5) and temperatures (up to 500 °C). This is contrary to the previous studies which deal with either only the room temperature [123] or only a limited range of N contents ($x \geq 0.4$) [124,177], let alone short sliding distances up to 200 m. In order to explain the evolution of the tribological properties (especially the oxidation wear at high temperatures) of $x \leq 0.20$ and $x \geq 0.27$ $WN_x$ films, the oxidation of these films is investigated in detail. In particular, we focus on ellipsometric characterization of the corresponding $WO_3$ scale formed on the film surface. The effect of the structure, microstructure and $H$ on the $\mu$, and the effect of the $H/E^*$ on the wear rate are investigated as well.

# II. Aims of the thesis

The Ph.D. thesis deals with the preparation of Al-Si alloy films, Al-Si-N films, β-phase films based on Ti, W films and $WN_x$ films by DC and AC pulsed magnetron sputtering and the investigation of their properties as a function of elemental composition and deposition conditions used in their deposition.

The aims of the Ph.D. thesis are following:

A. To investigate the effect of Si content in the Al-Si alloy films on their mechanical properties and to find the conditions under which the Al-Si alloy film exhibits the highest values of its hardness *H* and the ratio $H/E^*$; where $E^*$ is the effective Young's modulus.

B. To investigate the effect of the microstructure of the ceramic Al-Si-N films with different Si content on their wear resistance.

C. To sputter pure W films and find the conditions under which its *H* exceeds 15 GPa.

D. To sputter β-(Ti,W) films and investigate their thermal stability.

E. To sputter $WN_x$ films and investigate their tribological properties and oxidation resistance.

# III. Experimental details

## 1. Film preparation

### 1.1. Magnetron sputtering

The magnetron sputtering is a physical-vapor deposition (PVD) technique, widely used in the industrial coating application, and also is used for purpose deposition of all films in this Ph.D. thesis.

Briefly, **sputtering** [182] is the process where the atoms from the surface of the solid target (cathode) plate are ejected (emitted) after the collision (bombardment) of the energetically charged particles – ions (mostly used argon [$Ar^+$] ions with the energy typically ranging from 100 to 1000 eV) with this surface. These ejected atoms from the target plate may then condense on a substrate as a thin film. Secondary electrons (SE) are also ejected from the target surface as a result of the ion bombardment, and these electrons play an important role in maintaining the plasma discharge.

**Magnetron** [182,183] (in the sputtering) is the special arrangement of the permanent NdFeB magnets behind the target, where a magnetic field (B; typically 0.03–0.04 T on the target surface) parallel to the target surface restrains diffusion-out of the SE to the anode, and prevent SE from escaping the target region before they produce a number of ions. The magnets in planar geometry (in our case) consist of two magnets and are arranged in such way, that one pole (Ø 10 mm) is positioned at the central axis of the target and the second pole forms outer ring magnet (Ø 100 mm in our case) or is formed by the small magnets around the outer edge of the target. Trapping the electrons in this way substantially increases the probability of an electron-atom collision resulting in the higher plasma ionization. The increased plasma ionization results in a dense plasma in the target region. This, in turn, leads to increased ion bombardment of the target, giving higher sputtering rates and, therefore, higher deposition rates at the substrate. Additionally, higher plasma ionization caused by the magnetron allows the discharge to be maintained at the lower operating pressures (typically 0.2–1 Pa, compared to 2–10 Pa) and lower operating voltages (typically, -400 – -700 V, compared to -2 – -5 kV) than it is possible in DC diode discharge [183].

To maintaining the plasma discharge, the $N$ ions going from the cathode must produce at least one SE:

$$\gamma_{eff} \cdot N = 1, \qquad (1.1)$$

where $\gamma_{eff}$ is an effective secondary emission coefficient for reabsorption of the emitted SE at the cathode (after one or more gyro orbits); usually: $\gamma_{eff} = 1/2\gamma_{se}$, and $N$ (1.2) is the number of electron-ion pairs created by each SE which is trapped in the ring.

$$N \approx \frac{eU_{dc}}{\varepsilon_c}; \quad (1.2)$$

where $U_{dc}$ is the applied voltage which is dropped across the cathode sheath, $\varepsilon_c$ is the energy lost per electron-ion pair created by each secondary electron (15.75 eV for $Ar^+$, but average energy is 2–3 times higher), which is accelerated in the sheath and then trapped within the ring ($\varepsilon_c \approx 30$ eV). After substitution (1.1) into (1.2):

$$U_{dc} \approx \frac{2\varepsilon_c}{e\gamma_{se}}; \quad (1.3)$$

Where $\gamma_{se} = 0.1–0.2$ for metals.

The electron gyroradius $r_{ce}$ (1.4) caused by accelerated an electron from the target by the negative potential $U_{dc}$ on the target and pushed electron into the curved path by the Lorentz force is approximately:

$$r_{ce} = \frac{1}{B}\sqrt{\left(\frac{2m_e U_{dc}}{e}\right)}; \quad (1.4)$$

Where $m_e$ is the electron mass.

**Unbalanced magnetron** [182,183] is characterized by stronger outer magnet ring, that has more magnetic material and/or significantly stronger magnetic field than the central magnet. In this case not all the magnetic field lines are closed between the central and outer poles in the magnetron, but some are directed towards the substrate, and some SE are able to follow these field lines. Electrons that follow these field lines towards the substrate charge an insulating or floating substrate to a negative potential, which then attracts ions from the plasma to the substrate. This leads to high ion currents toward the substrate, and thus to densifying the film structure. More information about magnetron sputtering is given in: B. Window and N. Savvides (1986) [184], B. Window (1995) [185], R. Powell and S. Rossnagel (1998) [186], W. Westwood (2003) [183], M. Ohring (2005) [187], J. Musil, J. Vlček, and P. Baroch (2006) [188], D. Mattox (2010) [189], C. Bishop (2011) [190] and J. Greene (2017) [191].

## 1.2. Experimental setup

All experiments were done in the cylindrical stainless-steel experimental deposition chamber (Ø 500×400 $mm^2$), schematically illustrated in Fig. 1. The chamber was electrically grounded. The flow rates of the working gases, prior to their introduced into the chamber by inlet, were controlled by Mass-Flow controller driven by Multi gas controller 647C unit (MKS Instruments). In order to kept constant total pressure ($p_T$) during the sputter-deposition, the throttle (butterfly) valve between the chamber and the pumping system was used.

The magnetron-to-substrate configuration is clearly seen from the Fig. 1. The substrate holder was electrically insulated from the chamber and substrate heater. The substrate heating was carried out by the infrared radiation from the tungsten coil placed in the heater, which was located two centimeters beneath the substrate holder. The heater body was water-cooled in order to avoid itself from over-heating, and the chamber heating and subsequent desorption of the atoms and molecules from it during deposition. The substrate temperature was controlled by

the feedback controller and measured by thermocouple type K (electrically isolated from the chamber) mounted on the top of the substrate holder next to the substrates.

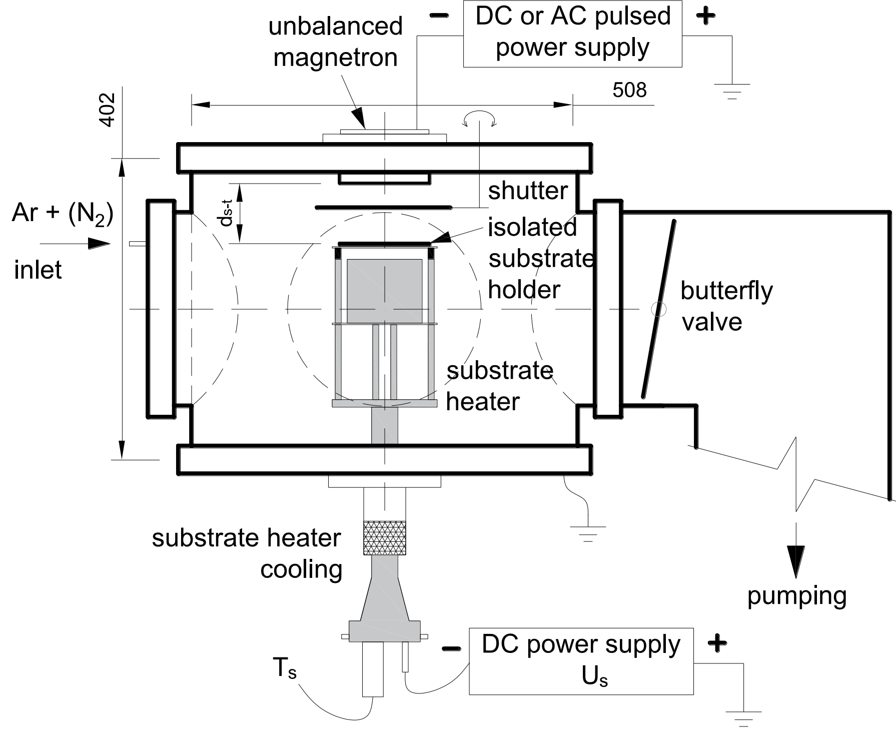


**Fig. 1.** Schematic illustration of the deposition chamber.

**Table 1**: Parameters of the AC pulsed power supply DORA/1.

| Parameters | values |
|---|---|
| maximum discharge voltage in micro-pulse $U_{d\ max\ (pulse)}$ (V) | -900 |
| maximum discharge current in micro-pulse $I_{d\ max\ (pulse)}$ (A) | 13 |
| maximum discharge power in micro-pulse $W_{t\ pulse}$ (kW) | up to 10 |
| constant AC pulsing frequency in a DC (unipolar) regime $f_{dc}$ (kHz) | 126 |
| constant repetition frequency $f_r$ (kHz) | 1 |

The target power density averaged per macro-pulse ($W_{ta}$) (packet of micro-pulses) was calculated:

$$w_{ta} = \frac{1}{\tau_{on}} \int_0^{\tau_{on}} U_d(t) I_d(t) dt; \qquad (1.5)$$

Where $U_d$ and $I_d$ are discharge voltage and current, respectively.

The deposition-averaged target power in a period ($P_{ta}$) was evaluated with the use of the formula:

$$P_{ta} = \frac{1}{T_p} \int_0^{T_p} U_d(t) I_d(t) dt; \qquad (1.6)$$

Where $T_p$ is a period.

All films were sputtered from an unbalanced magnetron (Ø 100 mm). The magnetron was powered either by the DC or AC pulsed unipolar power supply (DORA/1 Power System, Poland

[192]). The AC pulsed unipolar power supply combines (i) macro-pulses, i.e. pulsing of wave packets with a repetition frequency $f_r = 1/T_p = 1$ kHz, with (ii) micro-pulses, i.e. unipolar medium-frequency pulsing at a frequency $f_{dc} = 1/\tau_p = 126$ kHz inside each macro-pulse (see typical waveforms in Fig. 2), where $T_p$ is period. Parameters of the DORA/1 power supply are given in Table 1. Discharge power in the pulse $W_{t\ pulse}$ cannot be controlled, and depends on the plasma conductivity, magnetic field, total pressure, target material, etc. The AC pulsed unipolar magnetron discharge was controlled by the duty cycle $\tau_{on}/T_p$, that controls the number of the micro-pulses in packet (Fig. 2).

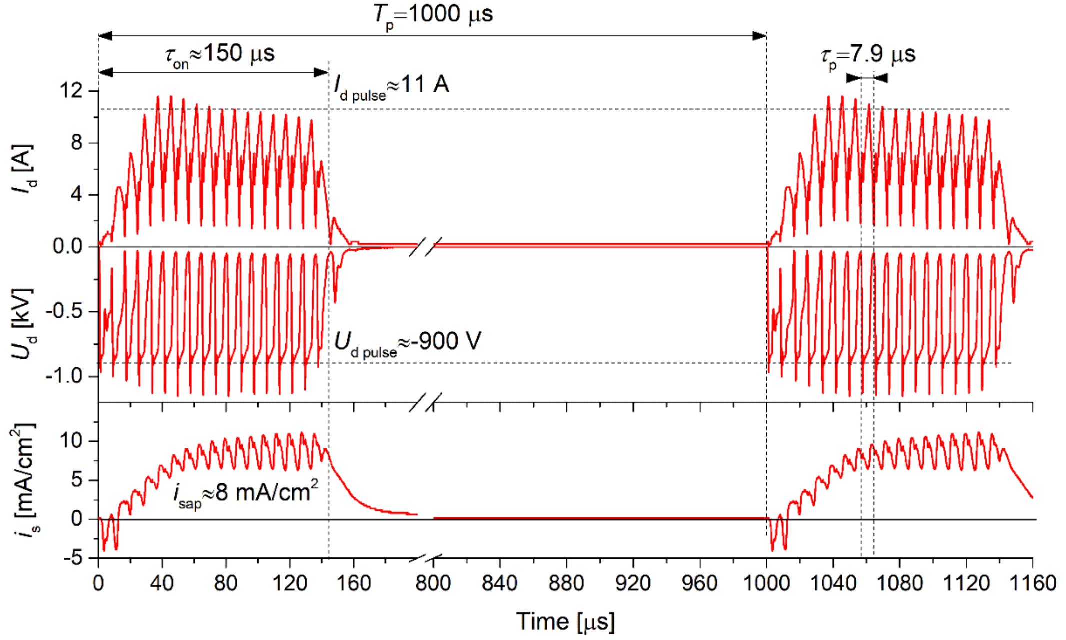


**Fig. 2.** Typical waveforms of the packets of micro-pulses with width $\tau_{on} = 150$ µs and period $T_p = 1000$ µs (duty cycle $\tau_{on}/T_p = 0.15$) from $WN_x$ deposition at $p_{N2} = 0.125$ Pa. Here $I_d$ and $U_d$ are discharge current and voltage, $I_{d\ pulse}$ and $U_{d\ pulse}$ are discharge current and voltage in the macro-pulse, and $i_s$ is the substrate current density ($i_{sap}$ averaged per macro-pulse) at DC bias -50 V.

## 1.3. Substrates and preparation prior to deposition

All depositions were carried out onto Si (100) plates (15×15×0.63 mm$^3$) and strips for stress measurement (25×5×0.63 mm$^3$) with hardness $H_{Si} = 14$ GPa and effective Young's modulus $E^*_{Si} = 150$ GPa. Besides Si, the 31CrMoV9 (15330) steel (Ø 25/2 mm) was used as a substrate. The substrates were ultrasonically cleaned in acetone for 10 minutes. Before the plasma ignition, the chamber was pumped simultaneously with substrate heating (typically to 300 °C) to desorb water molecules from the substrates. In order to improve the adhesion (removal of contaminants especially surface oxides), the substrates prior to each sputter deposition were etched in Ar plasma either (1) created by DC magnetron discharge at opened shutter (W based films – chapter IV.B, C, and D), or (2) created by DC pulsed power supply on the substrate holder at closed shutter (Al-Si based films – chapter IV.A). The adhesion was sufficient to prevent any delamination during the tribological experiments. In the first case, the etching was carried out at the magnetron discharge power $W_t = 0.75$ W/cm$^2$, substrate bias $U_s = -800$ V (high $Ar^+$ current density to substrate of ~0.4 mA/cm$^2$), argon pressure $p_{Ar} = 1$ Pa, substrate-to-target distance $d_{s-t}$

= 80 mm for 4 min. In the second case, the etching was carried out by a pulsed plasma (DC MDX power supply with Advanced Energy Sparc-LE pulsed unit) at discharge current to the substrate of 1 A, repetition frequency $f_r$ = 40 kHz, duty cycle 40 %, $p_{Ar}$ =2 Pa, $d_{s-t}$ = 80 mm for 10 min. Before the deposition, the target was sputter-cleaned at $p_{Ar}$ = 0.5 Pa and at an average current per period $I_{da}$ = 2 A for 3 min at the shutter closed. More information about adhesion improvement by plasma etching is given in chapter IV.B.

## 1.4. Deposition conditions

### 1.4.1. Al-Si films

The Al-Si films (2.3 ± 0.2 µm thick) were non-reactively sputter deposited in a pure Ar atmosphere. The magnetron was equipped with (i) Al/Si (70/30 at. %) alloy target, or (ii) composed target, i.e. round Si (99.95 % purity) plate overlapped by an Al (99.95% purity) ring with inner diameter $Ø_i$ of 40, 60 and 66 mm, leading to $Al_{73}Si_{27}$, $Al_{38}Si_{62}$ and $Al_{25}Si_{75}$ percentage fraction in the erosion zone, respectively. The magnetron was powered by an AC pulsed unipolar power supply. Deposition parameters are given in Table 2.

**Table 2:** Deposition parameters of Al-Si films.

| Parameters | values |
|---|---|
| total pressure $p_T = p_{Ar}$ (Pa) | 0.5 and 2.0 |
| base pressure before a deposition $p_0$ (Pa) | $1\times10^{-3}$ |
| substrate-to-target distance $d_{s-t}$ (mm) | 80 |
| peak target power density in pulse $W_{t\,peak}$ (W/cm$^2$) | 100 |
| averaged target power density per pulse $W_{ta}$ (W/cm$^2$) | 30 – 40 |
| duty cycle $\tau_{on}/T_p$ | 0.064 |
| substrate potential $U_s$ (V) | -50 – -350 |
| substrate temperature $T_s$ (°C) | 50 – 500 |

### 1.4.2. Al-Si-N films

**Table 3** Deposition parameters of Al-Si-N films. Where $U_{fl}$ is the floating potential.

| Parameters | values |
|---|---|
| total pressure $p_T = p_{Ar} + p_{N2}$ (Pa) | 0.5 |
| partial pressure $p_{N2}$ (Pa) | 0.1 |
| base pressure before a deposition $p_0$ (Pa) | $2\times10^{-3}$ |
| substrate-to-target distance $d_{s-t}$ (mm) | 80 |
| duty cycle $\tau_{on}/T_p$ | 0.14–0.15 |
| target power density averaged per macro-pulse $W_{ta}$ (W/cm$^2$) | 50 |
| substrate potential $U_s$ (V) | $U_{fl}$ ~ -50 |
| substrate temperature $T_s$ (°C) | 300 |

The Al-Si films were reactively sputter deposited in an Ar + $N_2$ gas mixtures. The magnetron was equipped with (i) Al/Si (90/10 at. %) and (70/30 at. %) alloy target, or (ii) composed target, i.e. round Si (99.95 % purity) plate overlapped by an Al (99.95% purity) ring with inner diameter $Ø_i$ of 66 mm, leading to $Al_{25}Si_{75}$ percentage fraction in the erosion zone. The magnetron

was powered by an AC pulsed unipolar power supply. Deposition parameters are given in Table 3.

### 1.4.3. W films

The W films (1.9–3.0 µm thick) were non-reactively sputter deposited in a pure Ar atmosphere. The magnetron was equipped with a W target (Ø 100×6 $mm^2$), which was sputtered using a DC and AC pulsed unipolar power supply. Deposition parameters are given in Table 4.

**Table 4:** Deposition parameters of W films.

| | DC | AC pulsed |
|---|---|---|
| Parameters | values | values |
| total pressure $p_T = p_{Ar}$ (Pa) | 0.5 and 1.0 | 0.5 |
| base pressure before a deposition $p_0$ (Pa) | 1.7 | |
| substrate to target distance $d_{s\text{-}t}$ (mm) | 80 | |
| target power density $W_t$ ($W/cm^2$) | 2.3 | - |
| target power density averaged per macro-pulse $W_{ta}$ ($W/cm^2$) | - | ~50 |
| duty cycle $\tau_{on}/T_p$ | - | 0.15 |
| DC substrate potential (bias) $U_s$ (V) | -50 – -200 | |
| substrate temperature $T_s$ (°C) | 300 | |

### 1.4.4. Ti-W films

**Table 5:** Deposition parameters of Ti-W films. Where $U_{fl}$ is floating potential.

| Parameters | values |
|---|---|
| total pressure $p_T = p_{Ar}$ (Pa) | 1.0 |
| base pressure before a deposition $p_0$ (Pa) | $1–2\times10^{-3}$ |
| substrate-to-target distance $d_{s\text{-}t}$ (mm) | 60 |
| target power density $W_t$ ($W/cm^2$) | 5.5 |
| Discharge current $I_d$ (A) | 1 |
| substrate potential $U_s$ (V) | $U_{fl}$, -50 – -250 |
| substrate temperature $T_s$ (°C) | 450 |

The Ti-W films (2.5–3.0 µm thick) were non-reactively sputter deposited in a pure Ar atmosphere. The magnetron was equipped with W target (Ø 100×6 $mm^2$) overlapped with Ti ring (Ø100×3 $mm^2$) with inner $Ø_{i\ Ti}$ = 30 mm and powered by DC power supply. Deposition parameters are given in Table 5.

### 1.4.5. $WN_x$ films

The $WN_x$ films (2.7±0.3 µm thick) were reactively sputter deposited in a wide range of Ar + $N_2$ gas mixtures. The magnetron was equipped with a W target (Ø 100×6 $mm^2$), which was sputtered using an AC pulsed unipolar power supply. See an overview of all deposition parameters in Table 6.

**Table 6:** Deposition parameters of $WN_x$ films.

| Parameters | values |
|---|---|
| total pressure $p_T = p_{Ar} + p_{N2}$ (Pa) | 0.5 |
| partial pressure of nitrogen $p_{N2}$ (Pa) | 0-0.5 |
| base pressure before a deposition $p_0$ (Pa) | $2\times10^{-3}$ |
| substrate to target distance $d_{s\text{-}t}$ (mm) | 80 |
| peak target power density in pulse $W_{t\ peak}$ (W/cm$^2$) | ≈100 |
| target power density averaged per macro-pulse $W_{ta}$ (W/cm$^2$) | ≈50 |
| duty cycle $\tau_{on}/T_p$ | 0.15 |
| DC substrate potential (bias) $U_s$ (V) | -50 |
| substrate temperature $T_s$ (°C) | 300 |

# 2. Film characterization

## 2.1. Profilometry

The film thickness ($h$) and macro-stress ($\sigma$) were measured using a stylus profilometer (DEKTAK 8 Stylus Profiler, Veeco), using the Stoney's formula (2.1) [193] in the latter case. The error of the measurement of $\sigma$ was 5 %.

$$\sigma = \frac{E_s}{1-\nu_s}\frac{h_s^2}{6h_f}\left(\frac{1}{R} - \frac{1}{R_0}\right); \quad (2.1)$$

Where $E_s$, $\nu_s$ and $h_s$ are Young's modulus, Poisson's ratio and thickness of the substrate, respectively, $h_f$ is the films thickness, $R$ and $R_0$ are the curvature radii of the substrate after and before deposition, respectively. The residual macro-stress in thin films $\sigma_{tot}$ (2.2) comprises the following structure-dependent components [194]:

$$\sigma_{tot} = \sigma_i + \sigma_{th} + \sigma_e; \quad (2.2)$$

where $\sigma_i$, $\sigma_{th}$, and $\sigma_e$ are the intrinsic, thermal and extrinsic stress, respectively. Thermal stress $\sigma_{th}$ (2.3) component can be calculated by:

$$\sigma_{th} = \frac{E_f}{1-\nu_f^2}(\alpha_f - \alpha_s)(T_s - T); \quad (2.3)$$

where $E_f$ and $\nu$ are Young's modulus and Poisson's ratio of the film, respectively, $\alpha_f$ and $\alpha_s$ are film and substrate thermal expansion coefficients, respectively, $T_s$ and $T$ are substrate temperature and temperature at which the $\sigma$ is measured, respectively.

## 2.2. Structure - XRD

The film structure was characterized using an XRD spectrometer (PANalytical X Pert PRO) in Bragg–Brentano configuration using CuKα radiation ($\lambda$ = 0.154 nm).

The mean size $D$ in [nm] of the ordered crystallite domains (which may be smaller or equal to grain size) was roughly estimated from broadening of the diffraction peaks using the Scherrer equation (2.4) [195]. Crystallite domains mean a coherent diffraction area perpendicular to the film surface.

$$D = \frac{k \cdot \lambda}{\beta \cdot \cos \Theta};\qquad (2.4)$$

Where $k$ is a dimensionless shape factor, typically from 0.8 to 0.9; $\lambda$ is the X-ray wavelength; $\beta$ is the line broadening at half the maximum intensity in radians (FWHM – "full width at half maximum"); $\Theta$ is the Bragg angle in radians.

## 2.3. Elemental composition

The elemental composition was obtained by a scanning electron microscope (SEM) (Hitachi SU-70) with energy-dispersive X-ray (EDX, UltraDry, Thermo Scientific) detector and/or with wave-dispersive X-ray (WDX, Magnaray, Thermo Scientific) detector. The error of the measurement of EDX and WDX was around 5 %.

## 2.4. Surface morphology and cross-section

The surface morphology, cross-section, observation of the indentation imprints and images of the wear track was taken by (1) a light optical microscope (LOM) (Axio Imager.Z2m) using brightfield or Circular polarized light – differential interference contrast (C-DIC) [196], or (2) a SEM (Hitachi SU-70) using secondary or reflected electrons (in the case of imaging of indentation images).

## 2.5. Mechanical properties

The mechanical properties (hardness $H$, effective Young's modulus $E^*$ (2.5) and elastic recovery $W_e$) were determined from load vs. displacement curves measured using (1) a micro-hardness tester (Fischerscope H100 VP) with a Vickers diamond indenter at a load of 10 mN (Al-Si films – chapter IV.A), 20 mN (Ti-W films – chapter IV.D) and 30 mN (Al-Si-N films – chapter IV.B), or (2) a nano-hardness tester (Hysitron TI 950 triboindenter) with a Berkovich diamond indenter at a load of 10 mN used in the case of chapter IV.C and E. To investigate the mechanical properties, 30 indentations into each sample was performed. The indentation depth was below 10 % of $h$ to avoid affecting of the measurement by the substrate. The error of the measurement of $H$ and $E^*$ was less than 10 %, typically in most measurements around 5 %. The mechanical properties were measured according to Oliver-Pharr model [197].

$$E^* = \frac{E}{1-\nu^2};\qquad (2.5)$$

Where $E$ and $\nu$ are Young's modulus and Poisson's ratio, respectively.

## 2.6. Cracking resistance

The cracking resistance was conducted by the high indentation load test [71], using the Vickers diamond indenter and applied load from 0.4 to 1 N on the films deposited on Si (100) substrate. In order to assess the cracking resistance, at least 10 indentations were performed.

## 2.7. Tribological properties

The friction coefficient $\mu$ and wear rate $k$ were evaluated using a pin-on-disk tribometer (CSM Instruments) at temperatures $T$ (constant during each test) from room (RT) up to 500°C. Most of the tribological measurements were done in an ambient air (relative humidity, RH = 30–50 %) using $Al_2O_3$ or 100Cr6 balls (Ø 6 mm) under a load $L$ = 2 N at a velocity $v$ = 5 cm/s and sliding distance $l$ = 1000 m (53052 cycles). For investigation of the effect of the film surface hydration on $\mu$ and $k$, some tribological tests at RT were performed in RH = 5% (dry nitrogen atmosphere) and RH = 82 % (moist environment). The test time of each tribological experiment, $l/v$, was 333 min. The $\mu$ was determined as a mean value from the steady-state period (described in each chapter) before the film got worn through. The wear rate was determined from the formula (2.6).

$$k = \frac{V}{l \times L}; \qquad (2.6)$$

where $V$ is the wear volume.

## 2.8. Spectroscopic ellipsometry

The thickness of the $WO_3$ scale ($h_{WO3}$) on the surface of the $WN_x$ films after the tribological tests at high $T$ was determined by variable angle spectroscopic ellipsometry (J.A. Woollam Co. Inc. instrument). The opaque bulk $WN_x$ (characterized before the tribological test) was represented by a combination of Lorentz oscillators, and the transparent $WO_3$ was represented by the Cauchy dispersion formula.

# IV. Results and discussion

The following results of the Ph.D. thesis are presented in the form of five chapters, where the first three (A, B and C) are unpublished or are in preparation for publication, and the last two chapters (D and E) are already published in prestigious international journals. These works contain the most important results that have been obtained during my Ph.D. study at the Faculty of Applied Science, University of West Bohemia in Pilsen since September 2015.

I carried out all depositions of (1) Al-Si films presented (A), (2) Al-Si-N films presented (B), (3) W films presented (C), (4) β-(Ti,W) films presented (D), and (5) W-N films presented (E).

I measured the film properties and interpreted the results obtained for the profilometry (thickness, roughness and stress in the films), the micro-indentation tests (mechanical properties), the topography obtained by optical microscope and scanning electron microscopy (SEM) (some part of results), the cracking resistance tests (indentations at high loads), the spectral transmittance (these data are not included into the thesis, they were published in the form of the first paper [Al-Si-N] – see chapter VIII, further publications of candidate), and part of the elemental composition measurement (SEM – EDX and WDS). The interpretation of the results includes calculation of the energy $E_{bi}$ delivered to the film by ion bombardment, for the purpose to explain evolution of the structure, microstructure, macro-stress and mechanical properties of the films. Moreover, I actively participated in the interpretation of the results obtained for (i) the phase composition (XRD), (ii) the elemental composition (SEM, EDX, and WDS), (iii) the tribological properties, and (iv) the optical properties and thickness of the films (spectroscopic ellipsometry).

# A. Mechanical and tribological properties of Al-Si films deposited by magnetron sputtering

# 1. Elemental content

The structure, microstructure and mechanical properties of Al-Si films strongly depend on: (i) deposition parameters, particularly $T_s$ and $U_s$, used in their preparation; and (ii) Al and Si fraction in the composed or alloy target. Al content was either (i) fixed in the case of Al/Si (70/30 at. %) alloy target, or (ii) controlled by $Ø_{i\ Al}$ of Al ring of the composed target.

Elemental content of the sputtered Al-Si films from the $Al_{73}Si_{27}$, $Al_{70}Si_{30}$, $Al_{38}Si_{62}$, and $Al_{25}Si_{75}$ targets is shown in Fig. 1. The oxygen content resulting from residual atmosphere was ranging from 2 to 4 at. %, while Ar content resulting from ion ($Ar^+$) bombardment was 1–4 at. %. The sum of O and Ar content in the films was between of 4–8 at. %. For simplicity, the Si or Al content in the films is expressed in the following text as $Al_{100-x}Si_x$, and vice-versa, where Ar and O content is neglected. It was found that Al content can be tuned by $U_s$. Fig. 1c,d shows that with increasing the $U_s$, the Al content in the films with Si > 60 at.% content decrease. It can be explained by re-sputtering of weakly bonded Al–Al and Al–Si with mainly metallic bonding [94,95], then that of strongly covalently bonded Si–Si in the Si dominant structure [97]. The experimentally calculated binding energy of the Al–Al, Al–Si, Si–Si, are 1.55, 2.60 and 3.21 eV [198], respectively. The re-sputtering of Al is more pronounced when the $T_s$ is higher. This can be explained by softening of metallic Al in the films at high $T_s$ (with regard to its low $T_m$). Additionally, the formation enthalpies of aluminum and silicon oxides are: $\Delta H_{Al2O3}$ = -1675.69 kJ/mol (= -558.6 kJ/mol per one O atom) and $\Delta H_{SiO2}$ = -910.86 kJ/mol (= -455.4 kJ/mol per one O atom). It means that aluminum has higher $\Delta H$ with O than per one O atom that of silicon, and therefore the hard $Al_2O_3$ phase can be preferentially formed.

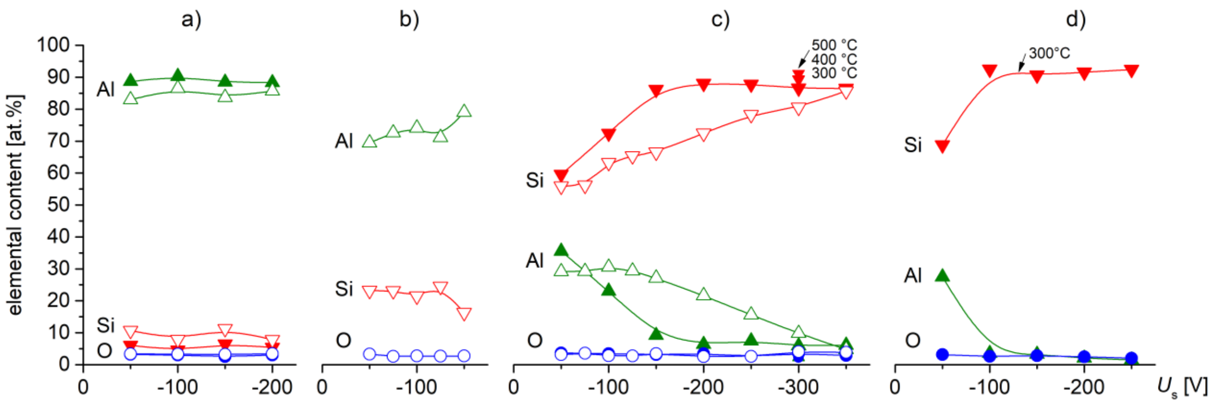


**Fig. 1.** Elemental content of Al-Si films sputtered on Si (100) from (a) $Al_{73}Si_{27}$, (b) $Al_{70}Si_{30}$, (c) $Al_{38}Si_{62}$, and (d) $Al_{25}Si_{75}$ target, as a function of substrate bias $U_s$. Filled symbols correspond to a heated substrate ($T_s$ = 200 °C) and empty symbols correspond to an unheated substrate.

# 2. Structure and microstructure

First of all, in order to investigate the effect of the structure on the $T_s$, the Al-Si films were unheated and heated up to $T_s$ = 500 °C during the deposition. Let recall, that $T_s$ significantly affects the structure of the films, because Al exhibits very low melting point $T_m$ = 660 °C, as compared with Si: $T_m$ = 1414 °C. The homologous temperature [22] $T_h = T_s/T_m$ at $T_s$ = 200 °C

for a pure Al film is $T_h$ = 0.30, while for a pure Si film is $T_h$ = 0.14. The Al-Si films were sputtered within a broad Si content ranging from 6 to 98 at.%. The structure of the Al-Si films with Si content <30 at.% and Si content >60 at.%, obtained by XRD, is shown in Figs. 2 and 3, respectively. There is shown that all films are composed of two fcc-Al and fcc-Si clearly separated phases. The mean crystallite (grain) size $D$(at.% Si, $T$, $U_s$), roughly estimated from broadening of the diffraction peaks Al (111) and (220), and Si (111) using the Scherrer equation [195], is shown in Fig. 4. It should be recalled that the grain size refinement plays important role in enhancing of the film hardness due to the grain boundary strengthening described by Hall–Patch relation. Fig. 4 shows that increasing Si content in the films leads to decreasing of $D$ below 10 nm.

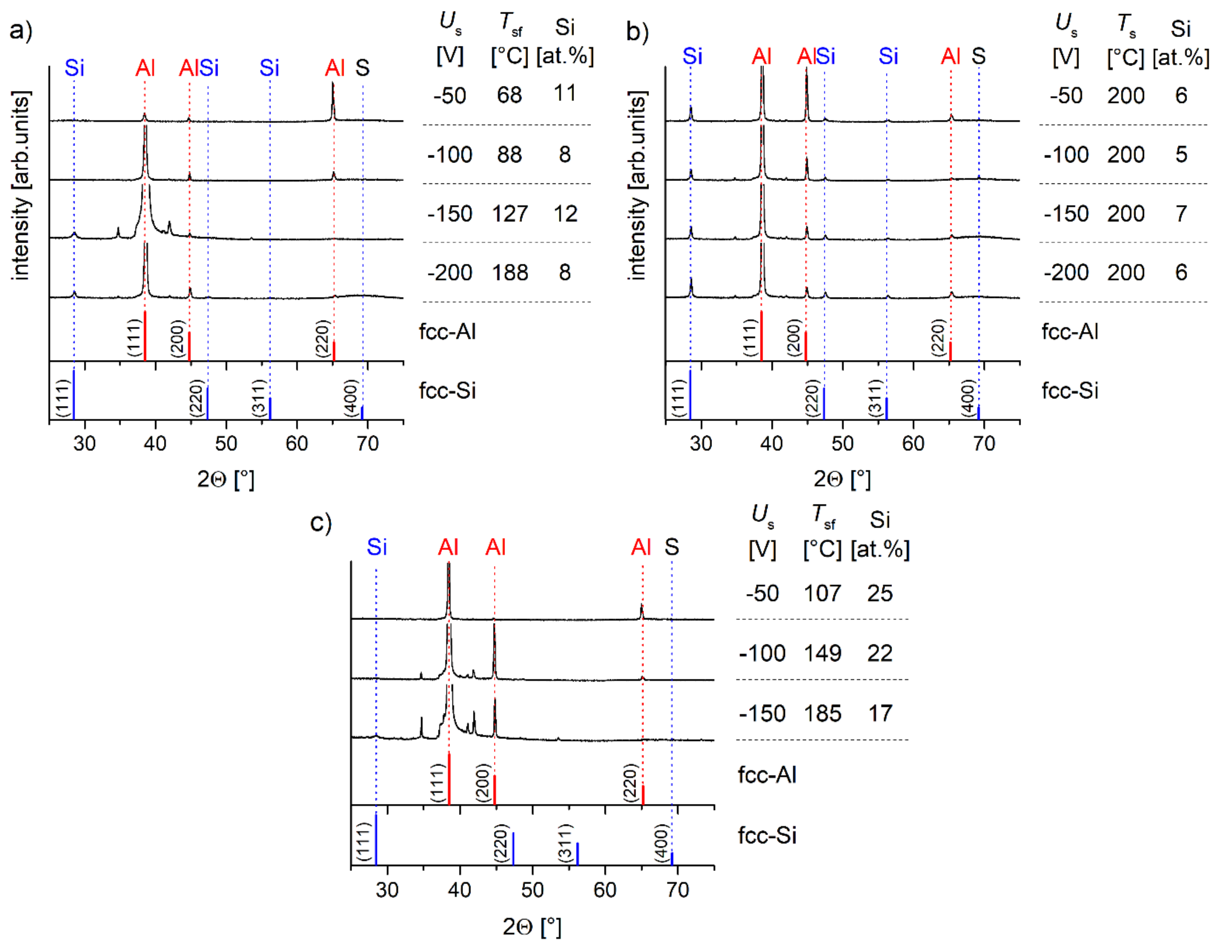


**Fig. 2.** XRD patterns of the Al-Si alloy films with Si < 30 at.% content deposited on Si (100) substrate from (a-b) $Al_{73}Si_{27}$, and (c) $Al_{70}Si_{30}$ target. Where $T_{sf}$ is the final substrate temperature at the end of deposition.

The structure of the fcc-Si phase in the Al-Si films depends mainly on $T_s$, where Si is either (1) amorphous (a-) at low $T_s$ up to ≈180 °C (unheated substrate) see Figs. 2 and 3a, or (2) nanocrystalline (nc-) with fcc-Si (111) preferred orientation at $T_s$ higher than ≈180 °C, see Fig. 2b,c,d. It was observed that during the deposition, the unheated substrates were self-heated by plasma, and the final substrate temperature $T_{ef}$ increases from 50 °C to 190 °C (measured at the end of the deposition) with increasing $U_s$ from -50 V to -200 V, respectively. Particularly, with increasing $U_s$, the ion current ($i_s$) to the substrate increases and then $T_s$ increases.

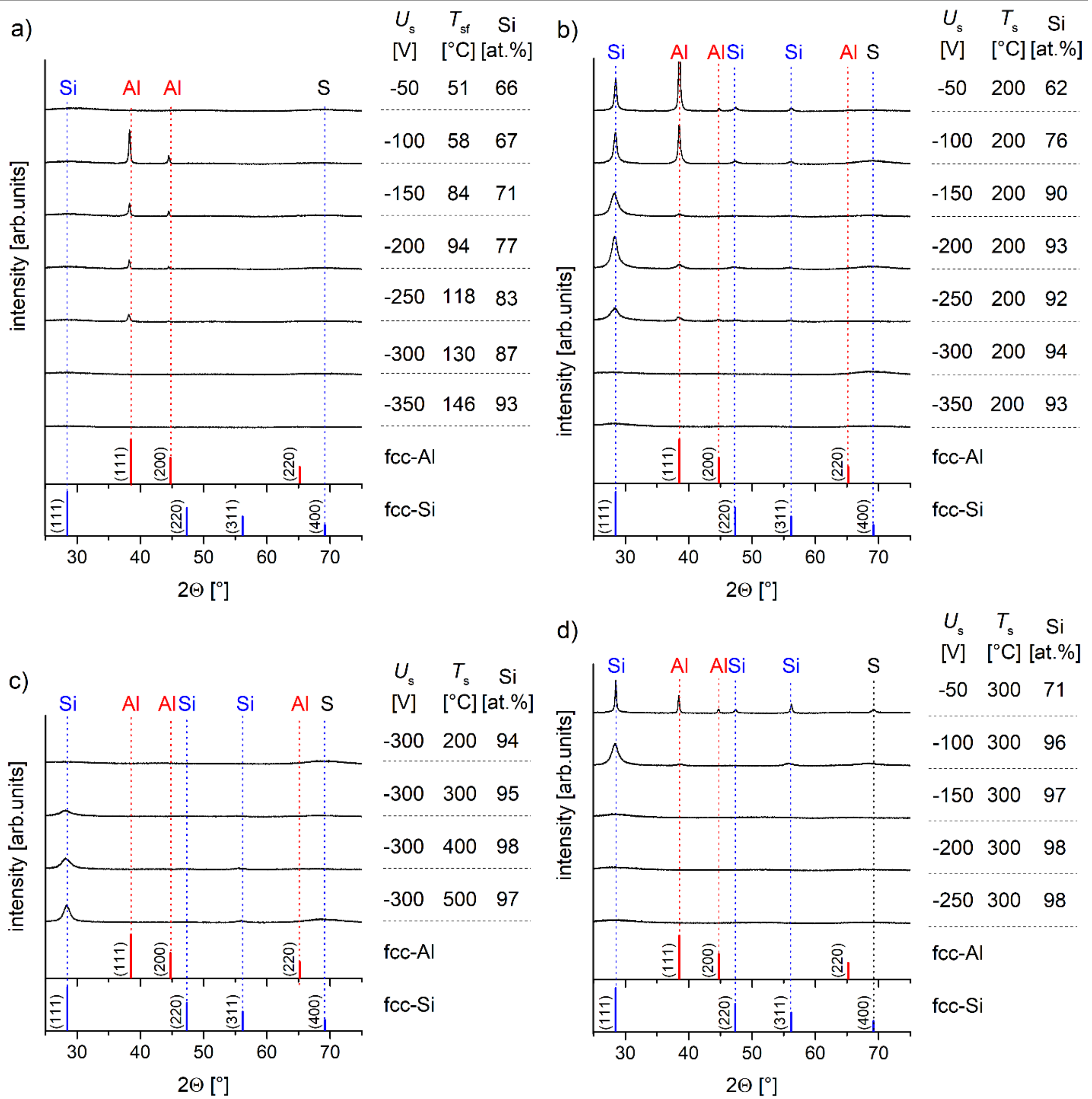


**Fig. 3.** XRD patterns of the Al-Si alloy films with high Si > 60 at.% content deposited on Si (100) substrate from (a-c) $Al_{38}Si_{62}$, and (d) $Al_{25}Si_{75}$ target. Where $T_{sf}$ is the final substrate temperature at the end of deposition.

The Al-Si films with low Si content <30 at.% Si, shown in Fig. 2, exhibit a polycrystalline structure composed mainly of nc-Al crystallites ($D_{Al}$ = 41–61 nm) with strong fcc-Al (111) preferred orientation and a weak contribution of (200) and (220) planes. It was observed that the crystallite size of Al did not reach $D \leq 10$ nm, despite the low $T_s$ = 68 and 100 °C and even low $U_s$ = -50 V or high $U_s \geq$ -200 V ion bombardment which can slow down a grain growth. The reason why it is difficult or almost impossible to achieve $D_{Al} \leq 10$ nm is the fact that Al has a low $T_m$ = 660 °C, and hence readily crystallize even at a low $T_s$ of ≈70 °C. Due to almost non-solubility of Si in Al, we assume that nc-Si or a-Si surrounds the nc-Al grains. Therefore, two nanocomposite structures of the Al-Si films at Si < 30 at.% were formed: (i) nc-Al/a-Si (at $T_s$ < 180 °C) or (ii) nc-Al/nc-Si (at $T_s$ > 180 °C).

The Al-Si films with approximately Si content from 62 to 83 at.% Si, shown in Fig. 3a,b, exhibit a polycrystalline structure composed of a mixture of low amount of nc-Al ($D_{Al}$ = 21–37 nm) and high amount either (1) a-Si at $T_s \leq 120$ °C (unheated substrates), or (2) nc-Si ($D_{Si}$ = 12–30 nm) with Si (111) texture at $T_s$ = 200–300 °C (heated substrates).

The Al-Si films with high Si content ≥87 at.% Si sputtered at either: (1) low $T_s \leq 200$ °C and $U_s \geq$ -300 V, or (2) high $T_s$ = 300 °C and $U_s$ = -150 – -250 V exhibit x-ray amorphous structure a-Si/a-Al, see Fig. 3. The amorphous structure is the result of either insufficient heating energy for to crystallize films and/or high ion bombardment of the films suppress grain growth during their grow. We assume that low content of Al, and/or O and Ar gas atoms (both up to 8 at.%) in the films also contribute to suppression the Si crystallite growth, due to segregation of these atoms on the Si crystallite boundaries. At the conditions of the high $Ar^+$ ion bombardment at $U_s$ ≥ -300 V, the Ar atoms are entrapped by the film structure and remain there even at a high ad-atom mobility at $T_s \geq 200$ °C.

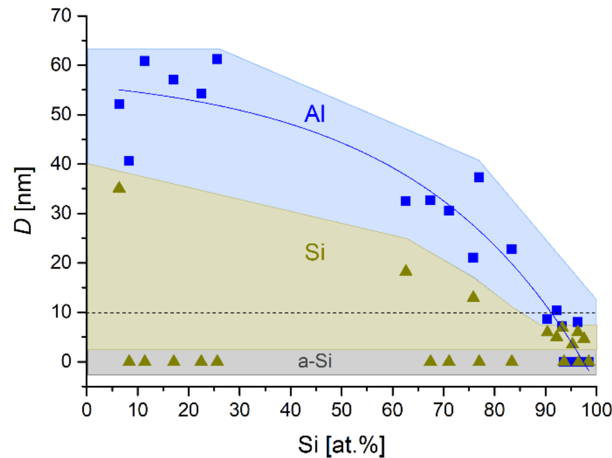


**Fig. 4.** Evolution of the mean grain (crystallite) size *D* evaluated from broadening of diffraction peaks Al (111) and Si (111) of the Al-Si films. Square and triangle symbols correspond to Al and Si crystallinities, respectively.

The Al-Si films with high Si content ≥90 at.% Si exhibit a nanocomposite structure with $D \leq 10$ nm (see Fig. 4) which is formed by either: (1) nc-Si/nc-Al at low energy deposition conditions: $T_s$ = 200–300 °C and $U_s$ = -100 – -250 V or (2) nc-Si/a-Al at high energy deposition conditions: $T_s \geq 300$ °C and $U_s$ = -300 V. We assume that a hard nc-Si phase in the films is surrounded by a non-soluble (in Si) (i) Al grains or a-Al tissue phase, and/or (ii) aforementioned Ar and O gas atoms.

Figure 5 shows cross-section SEM images of the Al-Si films with high Si > 60 at.% content and their structures represented by XRD patterns are shown in Figs. 2 and 3. It can be seen that these films exhibit a fine-grained, non-columnar, dense and void free microstructure which well correlate with mean crystallite size which is lower than $D$ = 40 nm shown in Fig. 4.

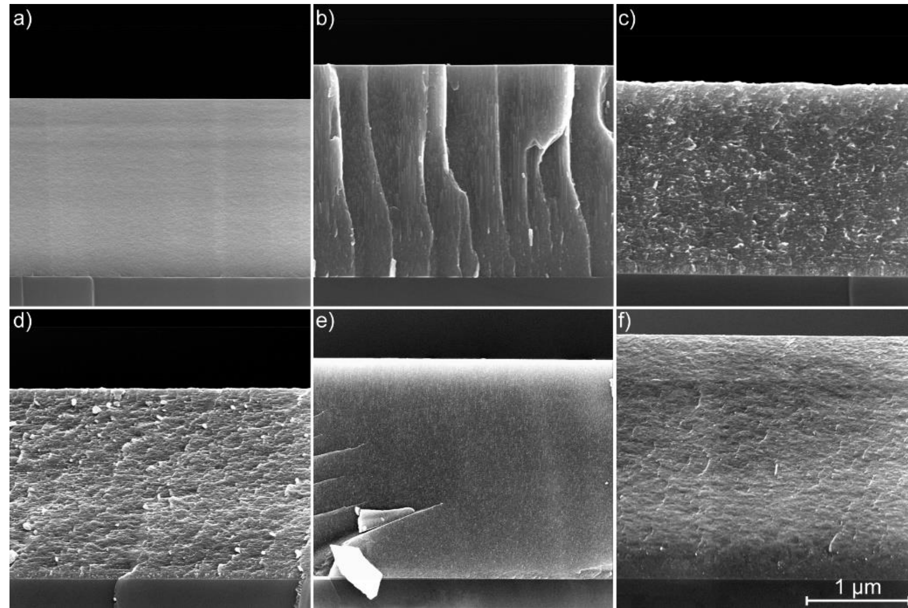


**Fig. 5.** Cross-sectional SEM images of the Al-Si films with high Si (a) 67 at.% Si, (b) 71 at.% Si, (c) 76 at.% Si, (d) 90 at.% Si, (e) 95 at.% Si, and (f) 96 at.% Si, sputtered on Si (100).

## 3. Mechanical properties

Mechanical properties ($H$, $H/E^*$ and $W_e$) of the sputtered Al-Si films as a function of the Si content in the films is shown in Fig. 6a, b. Moreover, the evolution of the residual macro-stress $\sigma$ with Si content in Al-Si films are shown in Fig. 6a. It was found that with increasing Si content in the films from 6 to 94 at.%, the $H$, $H/E^*$ and $W_e$ values of such films increasing from 2 GPa, 0.02 and 13 % to 12 GPa, 0.10 and 63 %, respectively. Where $H$ and $H/E^*$ values of the bulk Al and Si, are 0.5 GPa and 0.007, and 13 GPa and 0.087, respectively. In addition, the $E^*$ values of all deposited Al-Si films, not shown here, gradually increases from 102 to 128 GPa with increasing Si from 5 to 98 at.%, respectively. The hardness $H_{calc}$ according to rule of mixture (ROM) shown in Fig. 6a, was calculated by using formula: $H_{calc} = Al_{100-x} \times H_{bulk\ Al} + Si_x \times H_{bulk\ Si}$; where $Al_{100-x}$ and $Si_x$ represent elemental content of such elements. The evolution of the $H_{exp}$ values well correlate to $H_{calc}$ values, where the differences between $H_{exp}$ and $H_{calc}$ values can be explained by the grain size effect in the nanocrystalline and amorphous structure of the films. The $\sigma$ values in the films change from tensile +0.5 GPa to low compressive -0.5 GPa with increasing Si content in the films. The significant effect of $\sigma$ on the mechanical properties of the films was not observed. Low values of tensile or compressive $\sigma$ in the Al-Si films may be explained by high mobility of the weakly bounded Al atoms in the Al structure with low $T_m$ = 660 °C compared to Si atoms in Si structure with high $T_m$ = 1414 °C, due to: (1) high $T_s$ up to 500 °C, and (2) atomic scale heating caused by ion bombardment $U_s$ up to -350 V, that leave behind relaxed structure with less disorders in a crystal lattice of the films.

Enhanced mechanical properties up to $H$ = 14–15 GPa, $H/E^*$ = 0.11–0.12 and $W_e$ = 69–74 % (see Fig. 6) were observed in the Al-Si films: (1) sputtered at high energy deposition conditions: $U_s \geq$ -100 V and $T_s \geq$ 300 °C, and (2) with high Si ≥ 95 at.% content. At these conditions the nanocomposite or amorphous Al-Si films composed of either (1) nc-Si/a-Al with $D_{Si}$ = 3–6 nm

at $U_s$ = -300 V, or (2) nc-Si/nc-Al with $D_{Si}$ = 6 nm and $D_{Al}$ = 8 nm at $U_s$ = -100 V, or (3) a-Si/a-Al at $U_s$ = -150 – -250 V, were formed. Low Si crystallite size in Al-Si films results in increase of the their surface at the expense of their volume and then (a) the surface energy, and (b) the cohesive forces between the atoms start play dominant role and the $\sigma$ and $H$ increases from ±0.5 GPa to -0.7 – -1.1 GPa and from 12 GPa up to 15 GPa, respectively. Increase of the $H$ at sustain same $E^*$ = 122–127 GPa leads to an increase of the elastic deformation of the films, i.e. the quantities of elasticity $H/E^*$ and $W_e$ increase.

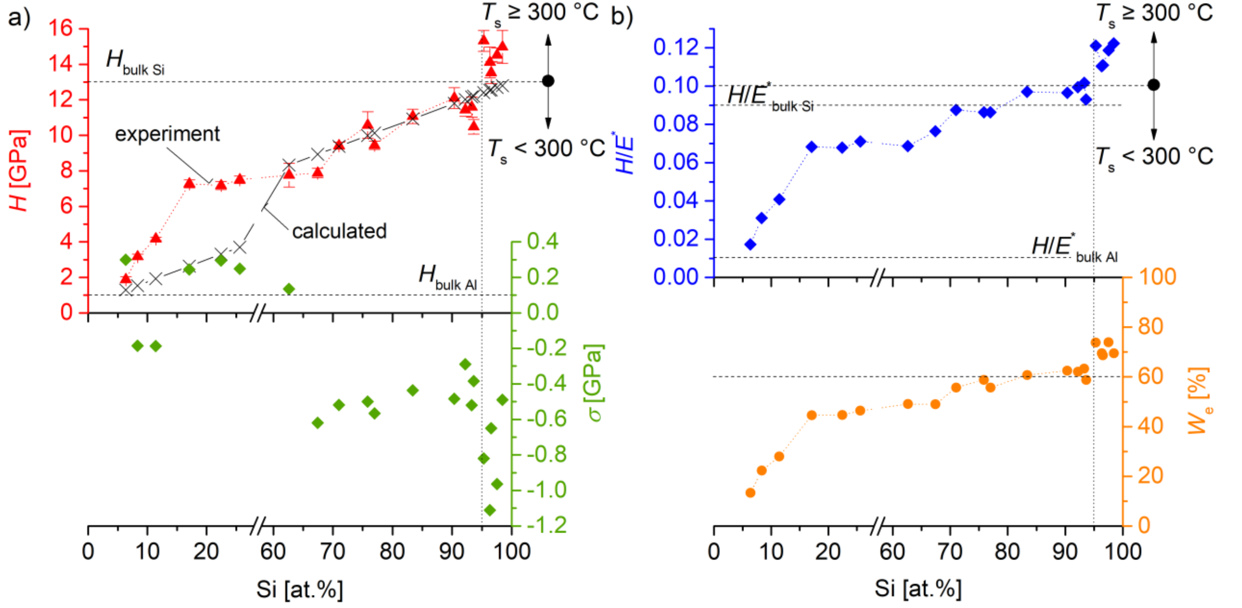


**Fig. 6.** (a) Hardness $H$ and macro-stress $\sigma$, and (b) $H/E^*$ and $W_e$ as a function of Si content in Al-Si alloy films.

Enhanced hardness of 7.0–7.5 GPa two times higher than considered ROM values of 3–4 GPa was observed in the Al-Si films with 17–25 at.% Si, see Fig. 6a. It can be explained by a formation of the nanocomposite structure nc-Al/a-Si with $D_{Al}$ = 54–61 nm, where Al crystallites are embedded in a-Si matrix. We assume that further decrease of the Al crystallites to <10 nm should lead to increasing of the hardness over 7.5 GPa.

Comparing both dependencies shown in Figs. 4 and 6a, we can observe that increasing of the hardness from 2 GPa up to 15 GPa with Si content well correlate with decreasing of the Al and Si crystallite size from $D_{Al}$ = 50–61 nm and $D_{Si}$ = 30–37 nm to nanocrystalline $D$ = 1–10 nm or $D$ < 1 nm (amorphous).

*In summary*, the Al-Si films with low Si content <30 at.%, with structures nc-Al/a-Si and nc-Al/nc-Si with high $D_{Al}$ up to 61 nm and $D_{Si}$ up to 25 nm and a-Al/a-Si, did not show high $H$ over 13 GPa. Because in the crystallites of these films the dislocation can pile-up and propagate and thus the grain boundary strengthening not occurs. However, the films with high Si content ≥95 at.%, with structures nc-Si/a-Al or nc-Si/nc-Al with low $D$ = 3–8 nm or a-Si/a-Al exhibit enhanced $H$ up to 15 GPa. These films were deposited at the high energy deposition conditions: $T_s$ ≥ 300 °C and $U_s$ ≥ -100 V, with low content of Al, O and/or Ar atoms that inhibit Si grain growth – similar results were obtained elsewhere [26].

## 3.1. Effect of the O content on the mechanical properties

Addition the low O content to the films is one of the ways how to decrease of the grain growth and thus increase the hardness of the films. Low O content in the structure (1) segregates at the grain boundaries of the film and decrease their growth, and (2) replaces weak metallic bonding (Me–Me) by strong ionic bonding (Me–O) which contribute to hardness enhancement. Recently [77] we have shown that the addition of low O content (up to 15 at. %) into the Zr-Ti alloy films enhanced their $H$ and $H/E^*$ three times: from 5 GPa and 0.043 to 16 GPa and 0.105, respectively. A.A. Voevodin et al. [199] showed $H$ = 17 GPa of the stoichiometric O/(Al+Si) = 1.9–2.1 Al-Si-O films with low Si content of 8 at.%. K. Bobzin et al. [200] found that with increasing the O content in the $AlO_x$ films, the $H$ and $E^*$ values increases from 2 GPa and 110 GPa to 26 GPa and 310 GPa, respectively. L. Šimurka et al. [201] showed $H$ = 8.5 GPa and $E^*$ = 75 GPa of the dense and stoichiometric $SiO_2$ films. However, the Al-Si films in this study (without additional O content) exhibit a very low O content up to 4 at.%, which can be insufficient to $H$ enhancement.

**Table 1** Deposition parameters and mechanical properties of Al-Si-(O) films deposited at: $U_s$ = -100 V, $p_T = p_{Ar} + p_{O2}$ = 0.5 Pa. Where $p_{O2}$ is partial pressure of the oxygen.

| $T_s$ [°C] | $p_{O2}$ [Pa] | $\sigma$ [GPa] | $H$ [GPa] | $E^*$ [GPa] | $H/E^*$ | $W_e$ [%] | Al [at.%] | Si [at.%] | O [at.%] | O/(Al+Si) | Si/Al | $D_{Si}$ [nm] | structure |
|---|---|---|---|---|---|---|---|---|---|---|---|---|---|
| 300 | 0.013 | -0.3 | 11 | 119 | 0.092 | 55 | 15 | 54 | 27 | 0.39 | 2.4 | <1 | a-(Al,Si,O) |
| | 0.05 | -0.4 | 11 | 90 | 0.121 | 73 | 2 | 32 | 66 | 1.97 | 13.3 | <1 | a-(Al,Si,O) |
| 700 | 0.01 | -0.3 | 15 | 142 | 0.106 | 66 | 10 | 59 | 30 | 0.44 | 6.1 | ~4 | nc-Si + a-(Al,Si,O) |
| | 0.025 | -0.3 | 10 | 87 | 0.120 | 71 | 1 | 33 | 66 | 1.93 | 26.7 | <1 | a-(Al,Si,O) |

Table 1 shows the mechanical properties and deposition parameters of the Al-Si films with low ~30 at.% O and high 66 at.% O content, deposited at low $T_s$ = 300 °C and high $T_s$ = 700 °C. Fig. 7 shows structure of the Al-Si-(O) films deposited at condition given in Table 1. It was found that only the Al-Si film deposited at $T_s$ = 700 °C with 30 at.% O content exhibits enhanced $H$ = 15 GPa, while other films exhibit $H \leq 11$ GPa, due to its amorphous structure. Enhanced $H$ of such film is due to nano-crystallization (see Fig. 7) of nc-Si to $D_{Si}$ = 4 nm at $T_s$ = 700 °C from under-stoichiometric O/(Al+Si) = 0.44 < 2.0 structure, where lack of O content is not enough to formation of a-(Al,Si,O) structure as well as in other films shown in Table 1.

*In summary*, addition of the O content of ~30 at.% nor 66 at.% into the Al-Si films deposited at $T_s$ = 300 °C, did not lead to enhance their $H$ over 13 GPa, due to a-(Al,Si,O) structure. Enhanced hardness to 15 GPa was observed only in the under-stoichiometric O/(Al+Si) = 0.44 < 2.0 Al-Si-(O) film deposited at $T_s$ = 700 °C, due to a formation of nc-Si with $D_{Si}$ = 4 nm surrounded by the a-(Al,Si,O) matrix. In both cases of the Al-Si and Al-Si-(O) films their $H$ did not exceed 15 GPa. The $H$ = 23.6 GPa and $E^*$ = 178 GPa of the Al-Si film with 25.2 at.% Si reported in [108] was not achieved in our Al-Si films deposited at a broad range of (1) the Si contents from 6 to 98 at.%, (b) the substrate temperatures from RT to 500 °C, and (3) the negative DC substrate bias from 50 to 350 V.

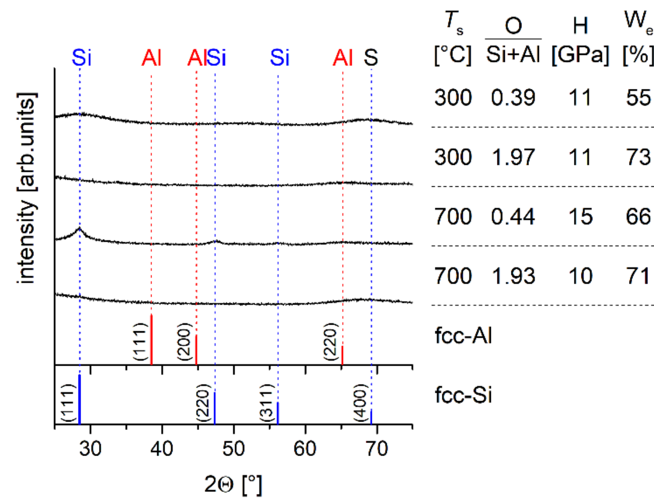


**Fig. 7.** XRD patterns of the Al-Si-(O) films as a function of Ts and stoichiometry O/(Al+Si) deposited on Si (100) substrate.

## 4. Resistance to cracking

In order to better understand the wear resistance of the Al-Si films, the cracking resistance was investigated. The cracking and wear resistance are mutually correlated, because during the loading of the film by a sliding ball, the crack formation and propagation causes wear of the film. Recently, in our department, it was found that the films with (1) high elasticity expressed by: $H/E^* > 0.1$, $W_e > 60$ %, i.e. high toughness [8], (2) compressive macro-stress ($\sigma < 0$), and (3) dense, non-columnar fine grained or amorphous microstructure, should exhibit an enhanced resistance to cracking [55,77,85] and enhanced resistance to wear [202].

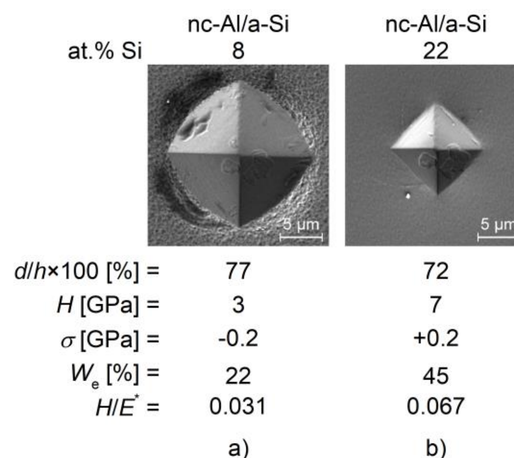


**Fig. 8.** Surface images obtained by SEM of the imprints after the indentation test at a high load of 0.4 N applied on the Al-Si films with high Al > 70 at.% content sputtered on Si (100).

Typical surface images of the imprints after measured resistance to cracking at a high indentation load of 0.4 N and 0.6 N applied on the Al-Si films deposited onto Si (100) with low Si and high Si content, are shown in Figs. 8 and 9, respectively. It was found that the Al-Si films with high Al content >70 at.% (see Fig. 8) exhibit no radial cracks even at (i) high $d/h > 70$ %, (ii) low elasticity: $H/E^* < 0.08$ and $W_e < 50$ %, and (iii) tensile $\sigma$ up to +0.5 GPa. SEM images of the indentations in the Al-Si films with low Si content < 30 at.%, exhibiting prominent material

pile-up around the indents indicating plastic flow characteristic of ductile materials, are shown in Fig. 8. Additionally, ductile material is characterized by a high plastic deformation (high deformation capacity). In ductile films, the tensile stress generated during an indentation test is absorbed by a plasticity of the films, i.e. the tensile stress is transferred into the local plastic deformation – irreversible deformation that does not cause the crack propagation (see pile-up in Fig. 8a).

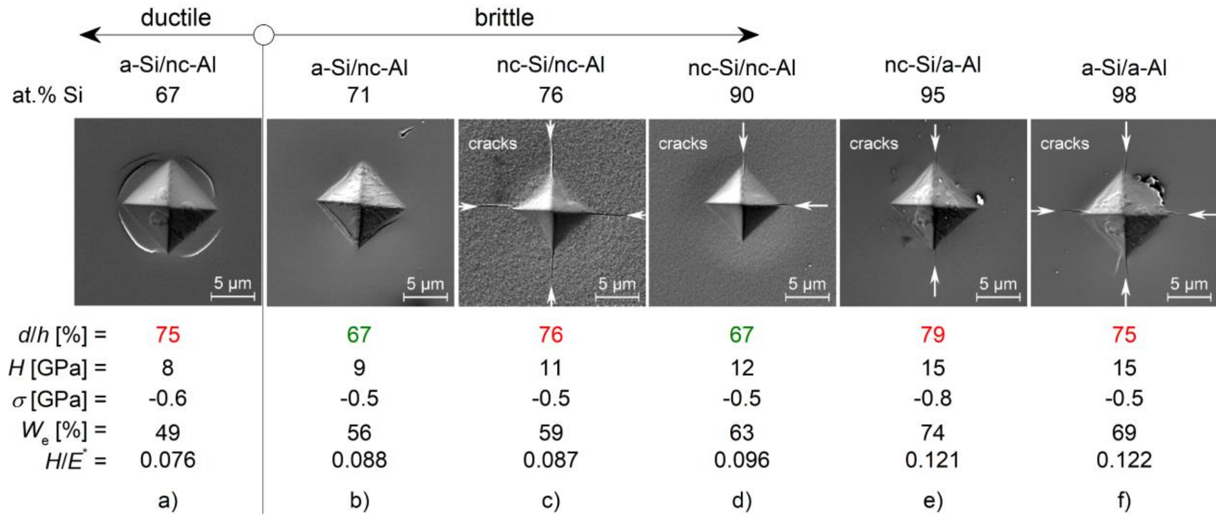


**Fig. 9.** Surface images obtained by SEM of the imprints after the indentation test at a high load of 0.4 N and 0.6 N applied on the Al-Si films with high Si > 60 at.% content sputtered on Si (100).

The Al-Si film with Si content of 70 at.% shown in Fig. 9a exhibits round pile-up (shear bands) due to its ductility, while the Al-Si films with Si content >70 at.% shown in Fig. 9c,d,e,f exhibit cracks along indent corners, even at $H/E^* > 0.08$ and $W_e > 50$ % and compressive macro-stress up to -0.5 GPa. Fig. 9b shows that the film with Si content of 71 at.% tested at the lower penetration depth $d/h \leq 67$ % of the indents did not cracks, due to its amorphous microstructure and generation of lower tensile stress in the indent corner by the indenter, while at $d/h > 70$ % the cracks were observed in the films, see Fig. 9c,e,f. It was observed that the films with Si content above 90 at.% Si and with high elasticity $H/E^* \geq 0.10$ and $W_e \geq 60$ % exhibit smaller cracks compared to the film with Si content of 76 at.% and low elasticity $H/E^* = 0.087$ and $W_e = 59$ %, see Fig. 9d,e,f and Fig. 9c, respectively. It means that in order to avoid cracking of the Al-Si film, its compressive macro-stress and/or elasticity must be sufficiently high to cover the tensile stress generated during an indentation test. We assume that the Al-Si films with Si > 70 at.% are brittle, even at (i) high $H/E^* \geq 0.10$ and $W_e \geq 60$ %, and (ii) non-columnar, dense and void free microstructure, and exhibit low resistance to cracking. This hypothesis is based on the fact that with increasing content of a brittle Si decreasing content of a ductile Al in the films. Moreover, higher compressive macro-stress, higher than 1 GPa can enhance cracking resistance of the Al-Si film [203], using extrinsic toughening approach [41].

*In summary*, the soft ($H \leq 8$ GPa) Al-Si films with Al content of ≥ 33 at.% Al are ductile and resistant to cracking, due to their low elasticity $H/E^* < 0.08$ and $W_e < 50$ %, and high plastic flow (pile-up) that inhibit crack formation. While, the hard ($H \geq 9$ GPa) Al-Si films with high Si content of > 70 at.% Si are brittle and resistant to cracking when the elasticity ($H/E^* > 0.08$

and $W_e > 50$ %) and the compressive macro-stress ($\sigma < 0$) are sufficiently high to prevent crack formation and propagation.

## 5. Friction and wear

Investigation of the tribological properties at a dry sliding was performed on the Al-Si films with Si content from 4 at.% to 98 at.% using 100Cr6 ball at RT and a load of 2 N. Typical evolution of the friction coefficient ($\mu$) of Al-Si film with Si content of 95 at.% with the sliding distance ($l$) up to 1000 m is shown in Fig. 10a. Figure shows that $\mu$ gradually increases with increasing $l$. The steady-state is achieved approximately after first 50 m of sliding.

Fig. 10b shows the mean values of the $\mu$ through steady-state, and wear rate ($k$) of the Al-Si films as a function of Si content. It was found that the Al-Si films with Si content <95 at.% were immediately worn through to the substrate already at a sliding distance lower than 10 m, due to low $H < 12$ GPa and nanocrystalline microstructure with $D > 4$ nm of the films. Therefore, $\mu$ and $k$ values of the films with Si content <95 at.% are unknown and cannot be given in Fig. 10b. Whereas, the films with Si content ≥95 at.% endured of 1000 m sliding and thus exhibit enhanced wear resistance. These films exhibit moderately high $\mu = 0.85$ and $k = 1$–$2 \times 10^{-6}$ mm³/Nm. Similar results of $k$ (0.9–1.4 × $10^{-6}$ mm³/Nm) were measured by Feng Xu et al. [108] in the Al-Si films, while they were measured lower $\mu = 0.23$ at testing temperature of 400 °C using $Si_3N_4$ ball. Enhanced wear resistance of the Al-Si films with Si content ≥ 95 at.% is result of: (1) higher $H > 12$ GPa (see Fig. 6a) of the Al-Si films than $H$ of the 100Cr6 ball ($H_{100Cr6} \approx 10.5$ GPa and $E^*_{100Cr6} = 210$ GPa), (2) high elasticity $H/E^* = 0.11$–$0.12$ and $W_e = 69$–74 %, and (3) dense non-columnar fine-grained nanocomposite nc-Si/a-Al structure with $D_{Si} \leq 4$ nm or amorphous microstructure of the films (see Figs. 4 and 5) where the crack generation and propagation along the grain boundaries are obstructed.

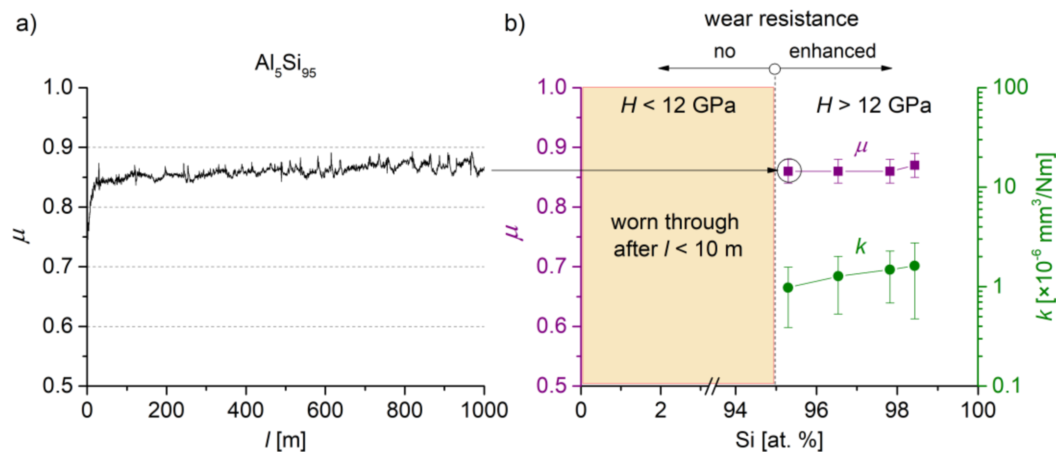


**Fig. 10.** (a) Typical evolution of the friction coefficient ($\mu$) with sliding distance ($l$) of the $Al_5Si_{95}$ film, and (b) the $\mu$ and wear rate ($k$) of Al-Si films as a function of Si content, at RT and RH = 25–33 % and $L = 2$ N.

The Al-Si films with ≥95 at.% Si exhibit comparable $k$ value to W film ($k_W = 0.8 \times 10^{-6}$ mm³/Nm) presented in our previous work [202], while $\mu$ value of W films is more than 3 times lower ($\mu_W = 0.26$), due to formation of lubricious $WO_3$ ($H_{WO3} = 5$ GPa, $H/E^*_{WO3} = 0.05$) in

wear track at RT and RH = 30–50 %. The $WN_x$ films [202] with $x$ = N/W ≥ 0.64 exhibited even lower $k_{WNx}$ = 0.01–0.06 × $10^{-6}$ $mm^3$/Nm and more than 2 times lower $\mu_{WNx}$ = 0.26–0.4 than Al-Si films.

The qualitative composition of the wear track shown in Fig. 11 and wear track profile and surface LOM images shown in Fig. 12 allow one to observe two different wear mechanism such as: abrasion and adhesion, that lead to formation of the crater and hill, respectively, in one wear track of the $Al_5Si_{95}$ film.

High $\mu$ = 0.85 values of the Al-Si films with ≥95 at.% Si can be explained by a formation of the high friction oxides [204]: $FeO_x$ (from the ball) and $AlO_x$ (from the film) in the wear track (see Fig. 11) during the sliding in the ambient air (RH = 25–33 %) at RT. The $\mu$ values can be considered to be a sum of (1) an adhesive part, due to the formation of asperity junctions, and (ii) an abrasive (deformation) part, due to ploughing or other forms of deformation caused by mechanical interlocking with a rough surface [205].

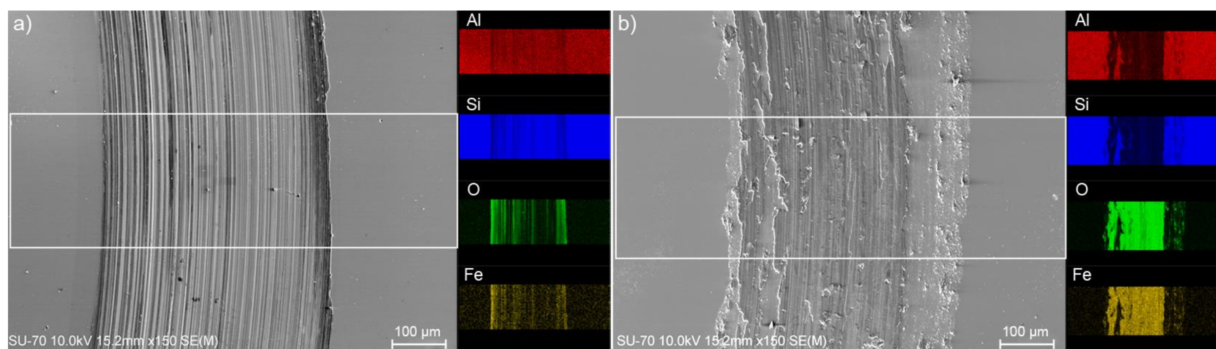


**Fig. 11.** Qualitative composition (Al, Si, O and Fe) of the wear track (a) crater, (b) hill, of the $Al_5Si_{95}$ film using 100Cr6 ball. The EDX measurement location area is given by the white rectangle.

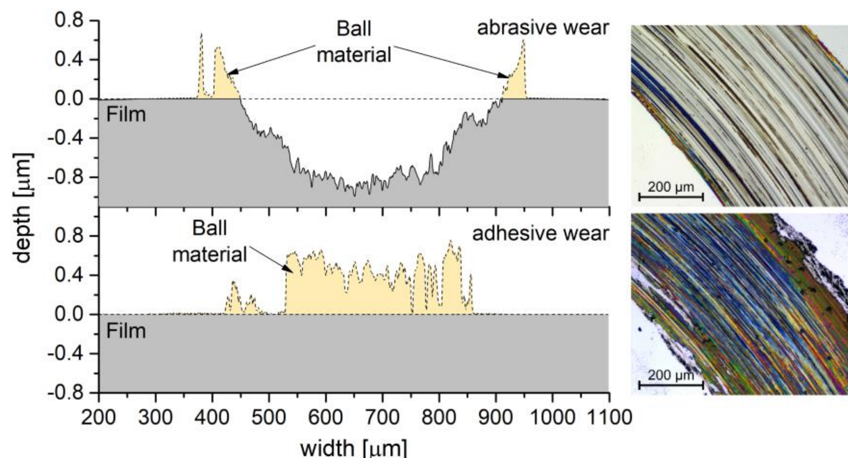


**Fig. 12.** Wear track profile (left) and surface LOM images (right) of the $Al_5Si_{95}$ film (2.18 µm thick) using 100Cr6 ball.

Moderate high $k$ = 1–2 × $10^{-6}$ $mm^3$/Nm of the Al-Si films with ≥95 at.% Si (compared to $WN_x$ films [202] with $x$ = N/W ≥ 0.64) may be explained by (1) a strong adhesive junctions between the ball and the films, (2) an abrasion of the film by a hard ball and/or hard third body ($FeO_x$) from the ball [1], and (3) not significantly higher $H$ of the films 14–15 GPa, compared to $H$ of the ball 10.5 GPa. High deviations (error bars) in wear rate, shown in Fig. 10, can be explained

by inhomogeneously worn films due to combination of abrasive and adhesive wear. Fig. 12 shows the wear track profiles of the $Al_5Si_{95}$ film, where both abrasive wear (see crater) and adhesive wear (see hill) were observed. High adhesive wear results in a large transferring of the 100Cr6 ball material into the wear track accompanied by formation of $FeO_x$ there. The oxide patterns in the wear track of the $Al_5Si_{95}$ film were observed and identified by (1) SEM and EDX mapping shown in Fig. 11, and (2) LOM as the colorful interference patterns, see right Fig. 12.

*In summary*, the Al-Si films with high Si content ≥95 at.% exhibiting high hardness $H$ up to 15 GPa, high $H/E^*$ up to 0.12 and $W_e$ up to 74 % and moderate wear rate $k = 1–2 \times 10^{-6}$ mm$^3$/Nm can be potentially used in the automotive as a protective coating for prolongation lifetime of the engine blocks and pistons in the case of its lubrication working (due to high friction of 0.8 during dry sliding). Where $H$ of the Al-12 wt.% Si alloy used for engine blocks is 103 HV (~1 GPa) [93], it is lower than $H$ of our Al-Si films with high Si content ≥95 at.%.

## B. On the significance of the microstructure in wear resistance of ceramic films

# 1. Structure and microstructure

Optimization of the microstructure is important not only to achieve enhanced oxidation resistance of the film [111], but also to achieve enhanced mechanical properties of the film [36]. Here we show that microstructure plays important role in the wear resistance of the ceramic films. Previously it was found that microstructure can be tuned by energy delivered into the films by the ion bombardment [84,85,203]. In this study we show that the microstructure of the Al-Si-N films, besides the energy, can be tuned by the incorporation of the Si content into the film over the solubility limit of such films.

**Table 1** Physical, chemical and mechanical properties of the Al-Si-N films. Where $x$ = N/(Al+Si) is the stoichiometry, $a_D = h/t_D$ is the deposition rate, $t_D$ is the deposition time, and $D_{AlN}$ is the crystallite size of AlN crystallites estimated from Scherrer equation. The films were deposited at $T_s$ = 300 °C, $p_T = p_{Ar} + p_{N2}$ = 0.4 + 0.1 = 0.5 Pa, $d_{s-t}$ = 80 mm, $U_s = U_{fl}$ using AC pulsed DORA/1 power supply and duty cycle was $\tau_{on}/T_p$ = 0.14–0.15.

| Si [at.%] | Al [at.%] | N [at.%] | O [at.%] | $x$ = N/(Al+Si) | $h$ [nm] | $a_D$ [nm/min] | $\sigma$ [GPa] | $H$ [GPa] | $E^*$ [GPa] | $H/E^*$ | $W_e$ [%] | $D_{AlN}$ [nm] | Microstructure |
|---|---|---|---|---|---|---|---|---|---|---|---|---|---|
| 4 | 43 | 50 | 2 | 1.05 | 2 250 | 11 | -1.8 | 30 | 210 | 0.144 | 80 | ~30 | Columnar |
| 10 | 31 | 57 | 2 | 1.37 | 4 200 | 28 | -1.6 | 33 | 213 | 0.157 | 88 | 1–10 | Non-columnar |
| 30 | 6 | 64 | 1 | 1.79 | 4 430 | 49 | -1.2 | 28 | 206 | 0.136 | 79 | <1 | Amorphous |

The Al-Si-N films were sputtered from three targets $Al_{90}Si_{10}$, $Al_{70}Si_{30}$, and $Al_{25}Si_{75}$ with different Si fraction in the erosion zone leading to Si content 4, 10 and 30 at.% in the films, see Table 1, respectively. The stoichiometry $x$ = N/(Al + Si) of the deposited films with Si content of 4, 10 and 30 at.% corresponds to 1.05, 1.37 and 1.79, respectively. Additionally, the stoichiometry of $Si_3N_4$ and AlN are $x$ = 1.3 and $x$ = 1.0, respectively. Considering the error of the WDS composition measurement, the Al-Si-N films with ≤10 at.% Si are stoichiometric, while the film with 30 at.% Si is overstoichiometric. The oxygen content resulting from the residual atmosphere is between 1–2 at.% O. The formation enthalpies of the aluminum and silicon oxides and nitrides are $\Delta H_{Al2O3}$ = -1675.69 kJ/mol and $\Delta H_{SiO2}$ = -910.86 kJ/mol, $\Delta H_{AlN}$ = -318.6 kJ/mol and $\Delta H_{Si3N4}$ = -745.1 kJ/mol, respectively. Lower Si content in the Al-Si-N films than that of in the targets can be explained by lower formation enthalpy of the $Si_3N_4$ (-186.275 kJ/mol) per one N atom than that of the AlN.

The phase structure obtained by XRD is shown in Fig. 1a. The film with 4 at.% Si is polycrystalline, while the films with 10 and 30 at.% are nanocrystalline (nc-) and X-ray amorphous (a-), respectively. In addition, the Si content up to 6 at.% is soluble in the h-AlN and form a solid solution h-$Al_{44}Si_6N_{50}$ [83]. Therefore, we consider that these 4 at.% Si are dissolved in the h-AlN phase of the film and form h-$Al_{43}Si_4N_{50}$ crystallites. The film with 10 at.% Si, see Fig. 1a, exhibits a nanocrystalline structure with low intensity of the h-AlN phase with (100), (002) and (110) planes. The presence of the crystalline $Si_3N_4$ phase is not observed by XRD in the film with 10 at.% Si, and we assume that the $Si_3N_4$ phase is present in the form of the amorphous thin tissue phase [36]. The film with Si content of 10 at.% Si is formed by the nc-$Al_{44}Si_6N_{50}$

crystallites surrounded by the thin a-$Si_3N_4$ matrix. The film with Si content of 30 at.% is completely amorphous composed of β-$Si_3N_4$ phase where peaks from the h-AlN were not observed.

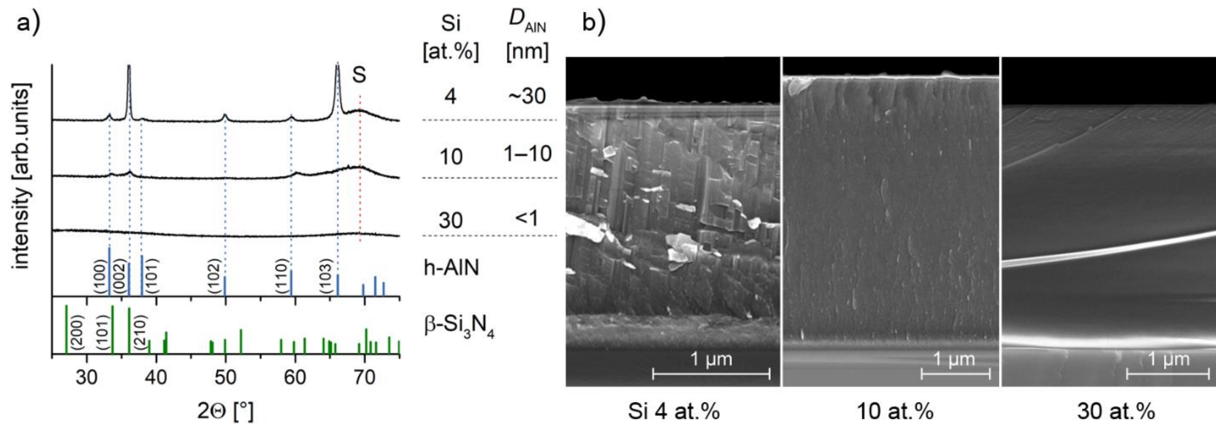


**Fig. 1.** (a) XRD patterns, and (b) cross-sectional SEM microstructure of Al-Si-N films deposited on Si (100) substrate as a function of the Si content. Where S is the substrate, and $D_{AlN}$ is the crystallite size of the AlN crystallites.

The mean crystallite size *D* (perpendicular to the film surface) of the films was roughly estimated from broadening of the diffraction peaks shown in Fig. 1a using the Scherrer equation [195]. The crystallite size *D* was calculated from h-AlN peaks (100), (002) and (110). The *D* of the film with 4 at.% Si is ~30 nm, while with further increasing Si content to 10 and 30 at.%, the *D* gradually decreases below 10 nm up to amorphous structure ($D < 1$ nm), respectively. This finding well correlates with the microstructure obtained by SEM cross-section images shown in Fig. 1b. The Al-Si-N films with Si content of 4, 10 and 30 at.% exhibit (1) a columnar microstructure with $D = 30$ nm, (2) a non-columnar nanocomposite microstructure where nc-$Al_{44}Si_6N_{50}$ crystallites ($D = 1$–$10$ nm) are surrounded by a-$Si_3N_4$ tissue phase, and (3) an amorphous microstructure composed of a-$Si_3N_4$ dominant phase, respectively. The evolution of the microstructure with different Si content in the Al-Si-N films was also observed elsewhere [36,83,115].

## 2. Mechanical properties

The mechanical properties ($H$, $E^*$, $H/E^*$, $W_e$ and $\sigma$) of the Al-Si-N films are shown in Table 1. Increasing of the Si content in the films from 4 at.% to 10 at.% Si results in increasing of the $H$, $H/E^*$ and $W_e$ values from 30 GPa, 0.144 and 80 % to 33 GPa, 0.157 and 88 %, respectively, due to nanocomposite structure nc-AlN / a-$Si_3N_4$ with $D = 1$–$10$ nm of the film [36,83]. With further increasing of the Si content in the film to 30 at.% Si, the $H$, $H/E^*$ and $W_e$ values decrease to 28 GPa, 0.136 and 79 %, due to amorphous microstructure of its film. All Al-Si-N films exhibit $E^* = 206$–$213$ GPa; where pure AlN and $Si_3N_4$ have $E^*_{AlN} = 200$ GPa and $E^*_{Si3N4} = 218$ GPa [206], respectively. Thanks to low $E^* \approx 200$ GPa values of the films and high $H > 25$ GPa, the Al-Si-N films exhibit very high elasticity ($H/E^*$ and $W_e$), i.e. they are deformed mainly elastically. The reasons leading to high $H > 25$ GPa values of the Al-Si-N films are (1) the nanocomposite structure, where the grain boundary strengthening (according to Hall-Patch relation [23]) occurs – within $D$ of 1–10 nm, the dislocation motion is hindered, and (2) the strong

bonding Al–N and Si–N [207] – a mixture of covalent and ionic nature (high contribution of ionic bonds is proved by high difference of Pauling electronegativity of Al [1.61 eV], Si [1.90 eV] and N [3.04] near to 1.7 eV).

All Al-Si-N films exhibit a compressive macro-stress ($\sigma < 0$) ranging from 1.2 to 1.8 GPa. Possible explanation of the $\sigma < 0$ in the films, can be "peening effect" [22,208] representing bombardment of the film by the energetic sputtered (Al, Si) atoms and their ions (not significantly scattered by working gas due to low product $p_T \times d_{s\text{-}t}$ shown in Table 1). In particular, presence Si content, in the Al-N film leads to a formation of the $\sigma < 0$, see Ref. [83]. Moreover, the presence of the $\sigma < 0$ in the nanocomposite ceramic film is very important in order to obstruct the crack propagation in the film by their closing.

## 3. Wear resistance

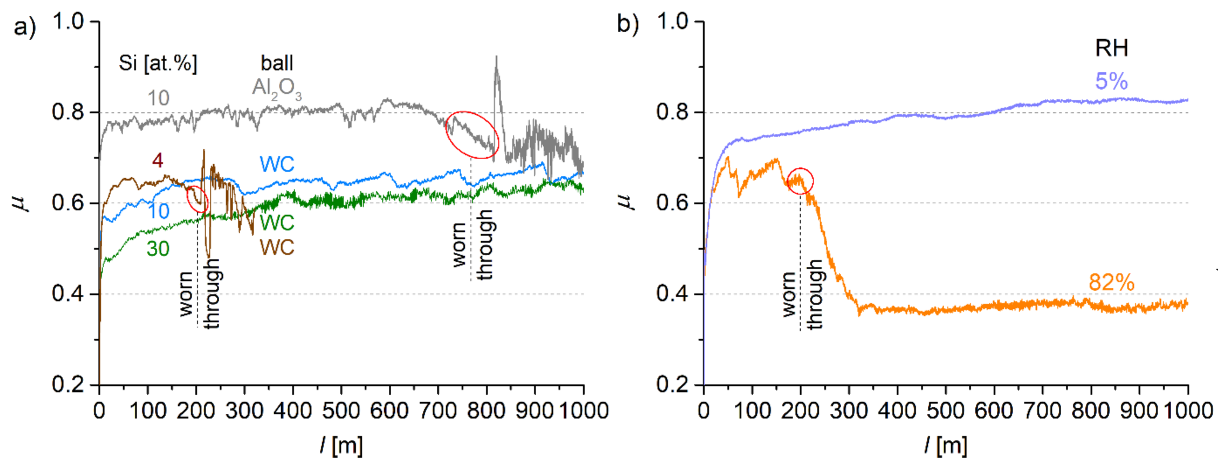


**Fig. 2.** Friction curves of Al-Si-N films with different Si content as a function of sliding distance $l$ of $Al_2O_3$ or WC ball. (a) Film with 4, 10 and 30 at.% Si tested by $Al_2O_3$ or WC balls at relative humidity RH of ~43 %, and (b) film with 10 at.% Si tested at RH of 5 and 82 %.

Typical friction curves $\mu(l)$ using $Al_2O_3$ and WC balls as counterpart of the Al-Si-N films with 4, 10 and 30 at.% Si content tested at RT and RH ~ 43 %, are shown in Fig. 2a. It was found that the films with Si content ≥10 at.% Si withstood the sliding of 1000 m. However, the film with Si content 4 at.% Si, despite of its high elasticity $H/E^* = 0.14$, high $H = 30$ GPa and $\sigma = -1.8$ GPa, failed at 200 m, due to its columnar microstructure, see Fig. 1b, where the cracks nucleation and propagation along the columns cause high wear.

The Al-Si-N film (3.8 μm thick) with Si content of 10 at.% Si tested by the $Al_2O_3$ ball was worn through after ~730 m, but the same film tested by the WC ball withstood the sliding of 1000 m, see Fig. 2a. Based on the fact that the $\mu$ and $k$ are correlated quantities, the higher $k$ of the film tested by the $Al_2O_3$ ball can be explained by its higher $\mu = 0.8$ than the $k$ of the film tested by the WC ball with its lower $\mu = 0.65$. It should be noted that the film surface, counterpart surface, or generally tribological contact between the film and counterpart with low shear strength exhibit a low $\mu$ [3,4], i.e. the shear strength is proportional to $\mu$ [2,5]. Such material with low $\mu$ is referred to as easy-to-shear. From classical model for sliding friction, in the case of metals, the shear strength at a first approximation is proportional to $H$ [5]. Here, the $Al_2O_3$ ball is formed

by strong Al–O bonds of covalent and ionic nature, resulting in high $H_{Al2O3\ ball}$ = 29 GPa and $E^{*}_{Al2O3\ ball}$ = 370 GPa, and the WC ball is also formed by strong covalent and soft metallic bonds W–W and W–C (and eventually C–C) result in $H_{WC\ ball}$ = 21 GPa and $E^{*}_{WC\ ball}$ = 500 GPa [5]. In particular, lower $\mu$ at using the WC ball than the $Al_2O_3$ ball is the result of (1) lower $H$ of the WC ball (21 GPa), and (2) the contribution of the metallic bonds to the ductility and plastic deformation of the WC ball. In other words, the WC ball is less abrasive than that of the $Al_2O_3$ ball during the sliding of the Al-Si-N film. Therefore, the further tribological experiments were performed by the WC ball as a counterpart.

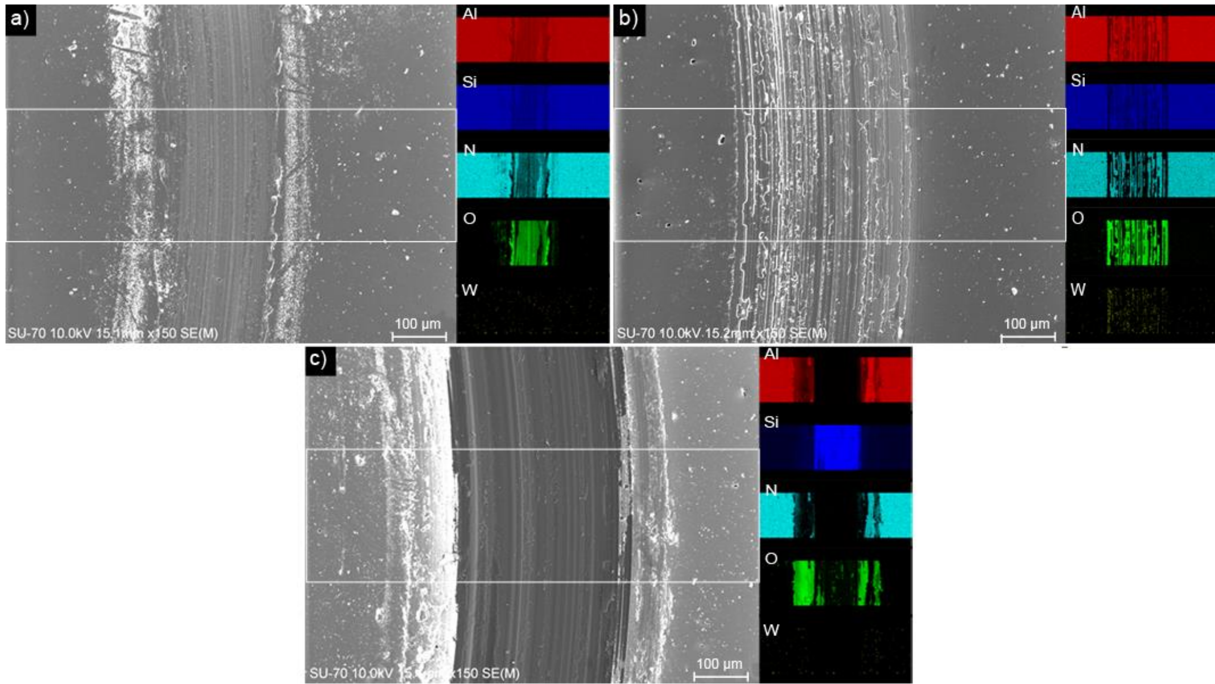


**Fig. 3.** Qualitative composition (Al, Si, O, N and W) of the wear track of the Al-Si-N film with 10 at.% Si deposited on Si (100) substrate tested at (a) RH = 5 %, (b) RH = 43 %, and (c) RH = 82 %, using WC ball. The EDX measurement location area is given by the white rectangle.

Typical friction curves $\mu(l)$ of the Al-Si-N film with 10 at. % Si tested at the relative humidity of 5 % (dry nitrogen) and 82 % (moist environment), are shown in Fig. 2b. The qualitative composition (Al, Si, O, N and W) analysis, conducted by EDX, of the film wear track tested at RH = 5 %, 43 % and 82 % is shown in Fig. 3a,b, and c, respectively. It was found that at RH from 5 % to 50 %, the film withstood the sliding of 1000 m, while at RH = 82 % the film was worn through after 200 m (see only Si patterns in the wear track in Fig. 3c), due to surface oxidation and formation of the abrasive $Al_2O_3$ [1,204] in the wear track (see Fig. 3b) as a product of hydration: $2AlN + 3H_2O \rightarrow Al_2O_3 + 2NH_3$ of the film with 10 at.% Si. The mean coefficient of friction (before worn through the film) for RH = 5 % and 82 % is $\mu$ = 0.8 and 0.65, respectively. Low $\mu$ (0.65) of the film tested at RH = 82 % is due to water droplets lubrication [209]. Fig. 3b displays that during the sliding of the WC ball over the surface of the Al-Si-N film with 10 at.% Si at RT and RH = 43 % occurs to (i) the oxidative wear, the $Al_2O_3$ and $SiO_2$ compounds are formed in the wear track, and (ii) the adhesive wear, the ball material is transferring (see W patterns in Fig. 3b) into the film surface.

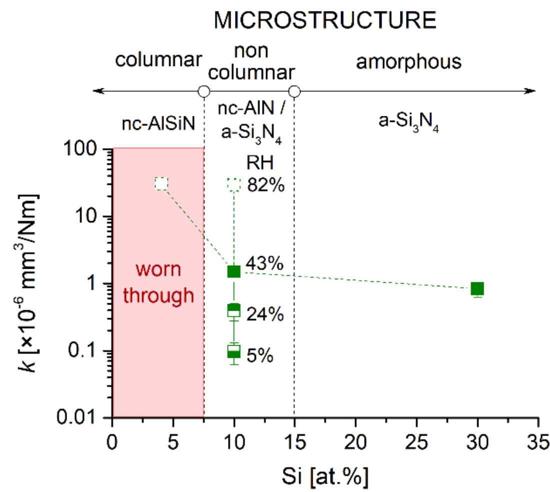


**Fig. 4.** Wear rate $k$ as a function of Si content in Al-Si-N films with 4, 10 and 30 at.% Si tested by WC ball at RT. Full symbols correspond to relative humidity RH of ~43 %. Empty symbols correspond to worn through film.

Figure 4 summarizes the effect of the Si content on the wear rate $k$ and microstructure of the Al-Si-N films tested by WC ball at RT and $L$ = 2 N. Fig. 4 shows that the film with low Si content of 4 at.% Si was worn through (the $k$ value is approximately determined to ~$30\times10^{-6}$ $mm^3$/Nm), while high Si contents from 10 to 30 at.% Si in the film result in an enhanced its wear resistance. This is due to change of the film microstructure from columnar at 4 at.% Si, through non-columnar dense nanocrystalline microstructure at 10 at.% Si, to amorphous micro-structure at 30 at.% Si. Increase of the Si content in the film from 4 at.% to ≥10 at.% Si results in a significant decrease in $k$ from ~$30\times10^{-6}$ $mm^3$/Nm to ~$1.0\times10^{-6}$ $mm^3$/Nm, respectively. It means that both the nanocrystalline film with $D$ = 1–10 nm and amorphous film are more re-sistant to wear compared to the columnar film.

It was found that $\mu$ and $k$ values of the Al-Si-N films are strongly dependent on the RH, see Fig. 2a,b and Fig. 4, respectively. Particularly, with decreasing RH from 38–50 % (ambient air) to 5 % (dry nitrogen), $\mu$ increases from 0.63 to 0.79, but $k$ decreases from $1.49\times10^{-6}$ $mm^3$/Nm to $0.096\times10^{-6}$ $mm^3$/Nm, respectively, in the film with 10 at.% Si. It can be explained by the low amount of lubricious water molecules [5,210] at RH = 5 %, which leads to low formation of products of an oxidation that cause higher wear of the sliding surface.

Moderately high $\mu$ and $k$ values of the Al-Si-N films, tested at RT and RH = 35–82 %, can be explained by (1) high $H$ = 31–34 GPa and aforementioned strong covalent/ionic bonds Al–N and Si–N which are hard-to-shear, and (2) formation of the high friction $Al_2O_3$ [204] and abra-sive [1] products of oxidation ($Al_2O_3$ and $SiO_2$) in the wear track. While the Al-Si-N film tested in dry nitrogen RH = 5 % exhibit very low $k$ ~ $0.1\times10^{-6}$ $mm^3$/Nm.

*In Summary*, the tribological experiments of the Al-Si-N films have clearly shown that the elas-ticity parameters $H/E^*$ and $W_e$ have less significance than that of the microstructure of the film on the film wear resistance. Particularly, the Al-Si-N film with 4 at.% Si content with a colum-nar microstructure exhibited no wear resistance even at its high $H/E^*$ = 0.14 and $W_e$ = 80 %, while the films with ≥10 at.% Si with a nanocomposite nc-AlN/a-$Si_3N_4$ microstructure ($D$ = 1–

10 nm) or amorphous microstructure, where the cracks propagation is obstructed, exhibited enhanced wear resistance.

## C. Hardness enhancement in W films deposited by magnetron sputtering

# 1. Adhesion

In order to deposit several microns thick W films at low working gas Ar pressure ($p_T \leq 1$ Pa), at the substrate temperature $T_s$ = 300 °C (corresponding to zone T in Thornton zone model [22]), the problem with adhesion had to be solved. Several studies [211,212] showed that the sputtering of >100 nm thick films at a Ar pressure <1 Pa led to generation of the high compressive macro-stress in the films that exceeds -2 GPa. This high macro-stress led to delamination and buckling of the W films from the substrate (Si). Several authors investigated different approaches to deposit the W film, exhibiting large compressive macro-stress. They usually improved the adhesion of the films to the substrate and/or decreased the macro-stress of the film by using: deposition under oblique angles [213], 10–30 nm thick Cr or Ti sticking layer [146,214], low sputtering power (≤ 50 W) [147], high power impulse magnetron sputtering (HiPMS) [122], high working pressure of 2 Pa [215], substrate plasma etching [216].

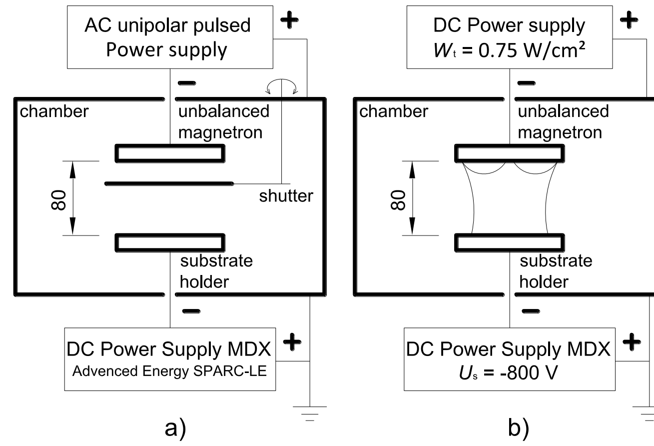


**Fig. 1.** Schematic illustration of the powering of the magnetron and substrate holder during the substrate plasma etching by (a) the DC pulsed plasma at the discharge current to the substrate of 1 A, repetition frequency $f_r$ = 40 kHz, duty cycle 40 %, $p_{Ar}$ = 2 Pa, and (b) low power ($W_t$ = 0.75 W/cm$^2$) magnetron discharge DC plasma, DC substrate bias $U_s$ = -800 V (high Ar+ current density to substrate of ~0.4 mA/cm$^2$), and $p_{Ar}$ = 1 Pa.

**Table 1:** Etching conditions and comparison of the etching rate $a_E$ of the Si (100) and steel 15330 substrate. Substrate holder was biased by DC power supply to $U_s$, while the target was sputtered at low power density ($W_t$). The substrates were etched at: target power $P_t \approx 60$ W, $p_{Ar}$ = 1.0 Pa, $d_{s\text{-}t}$ = 80 mm, $T_s$ = 300 °C for 10 min. Where $i_s$ is the ion current density to substrate. Post-etching substrate roughness ($R_a$) was measured by AFM.

| | | | | Si (100) | | Steel 15330 | |
|---|---|---|---|---|---|---|---|
| $U_s$ | $i_s$ | $W_t$ | $h_E$ | $a_E$ | $R_a$ | $h_E$ | $a_E$ |
| [V] | [mA/ cm$^2$] | [W/ cm$^2$] | [nm] | [nm/ min] | [nm] | [nm] | [nm/ min] |
| -200 | 0.25 | 0.71 | n.m. | n.m. | n.m. | -100±40 | 10 |
| -400 | 0.31 | 0.71 | n.m. | n.m. | n.m. | -370±40 | 37 |
| -600 | 0.31 | 0.70 | -500 | 50 | 4.4 | -500±80 | 50 |
| -700 | 0.35 | 0.73 | -590 | 59 | 5.2 | -610±40 | 61 |
| -800 | 0.37 | 0.73 | -640 | 64 | 8.2 | -680±90 | 65 |
| -1000 | 0.39 | 0.76 | -770 | 77 | 4.5 | -670±30 | 67 |

n.m. denotes to not measured

From aforementioned methods of the W adhesion improvement to Si (100) or steel 15330 substrates, there is suitable, in our case, just only last method – substrate plasma etching. Because, our aim is to find the conditions under which at least 2 μm thick W film exhibit enhanced $H$ > 15 GPa. Thus, it requires to use high energy deposition conditions ($p_T \leq 1$ Pa, sputtering powers >150 W and high negative substrate biases) of the W deposition, and high deposition rates >20 nm/min. However, these conditions lead to high compressive macro-stress in the W film.

Figure 1a and b schematically illustrate the powering of the magnetron and substrate holder during the substrate plasma etching by (1) the DC pulsed plasma, and (2) the DC plasma generated from low power magnetron discharge, respectively.

In the first method of the plasma etching, prior to the deposition of the W film, the substrates were etched by the DC pulsed plasma (see Fig. 1a) for 10 min, with closed shutter. Unfortunately, insufficient plasma density at the DC pulsed regime led to the delamination of the W film from the substrate, due to insufficient removing of the contaminants (oxides) from the substrate surface. Typical surface image of the delaminated W film (>1.5 μm thick), deposited at DC target power density $W_t = 2$ W/cm$^2$, $p_{Ar} = 0.5$ Pa, and $U_s = -50$ V, from the steel 15330 substrate, is shown in Fig. 2. Therefore, it was developed the second method of plasma etching, see Fig. 1b, where the shutter was opened, and the substrates were etched together with low DC power ($W_t = 0.75$ W/cm$^2$) magnetron discharge to increase plasma density in front of the substrates. The $W_t$ was selected very low, to achieve a stable magnetron discharge and low deposition rate ($a_D < 5$ nm/min – without substrate bias). The $Ar^+$ ions from the magnetron discharge were extracted and accelerated by high negative substrate DC bias ($U_s$) in direction of the substrate. Due to high energy of the $Ar^+$, controlled by the $U_s$, the substrates were re-sputtered (etched) with etching rate ($a_E$). In Table 1 are given etching conditions and values of $a_E$, etched depth ($h_E$) and surface roughness ($R_a$) after the etching, of the Si (100) and steel 15330 substrates. Fig. 3a,b shows $h_E$ and $a_E$ as the function of the $U_s$ after the etching of the Si (100) and steel 15330 substrate, respectively, for 10 min. Figure shows that substrates were effectively etched already at $|U_s| \geq 400$ V (at conditions: $W_t \approx 0.75$ W/cm$^2$, $p_{Ar} = 1.0$ Pa, $d_{s\text{-}t} = 80$ mm, $T_s = 300$ °C). Therefore, in further depositions of the W films and W-based films, with regard to reasonable etching rate, the substrates were etched at $U_s = -800$ V for 4 min. As a result, it has been removed from the surface of the substrates approximately 200–250 nm of the surface layer (contaminants).

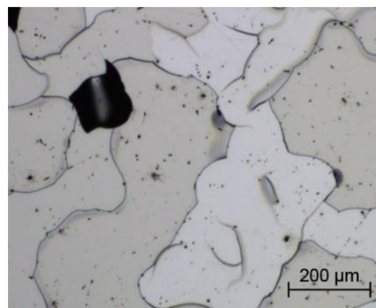


**Fig. 2.** LOM surface image of the W film delamination. The film was etched only by the pulsed plasma shown in Fig. 1a.

The roughness of the Si (100) surface has increased two times from $R_a$ = 2–4 nm to $R_a$ = 4.4–8.2 nm after the plasma etching with low power magnetron discharge, measured by AFM (see Table 1). The AFM surface morphology of etched Si (100) surface and step of covered and uncovered etched Si (100) surface at $U_s$ = -600 V is shown in Fig. 4.

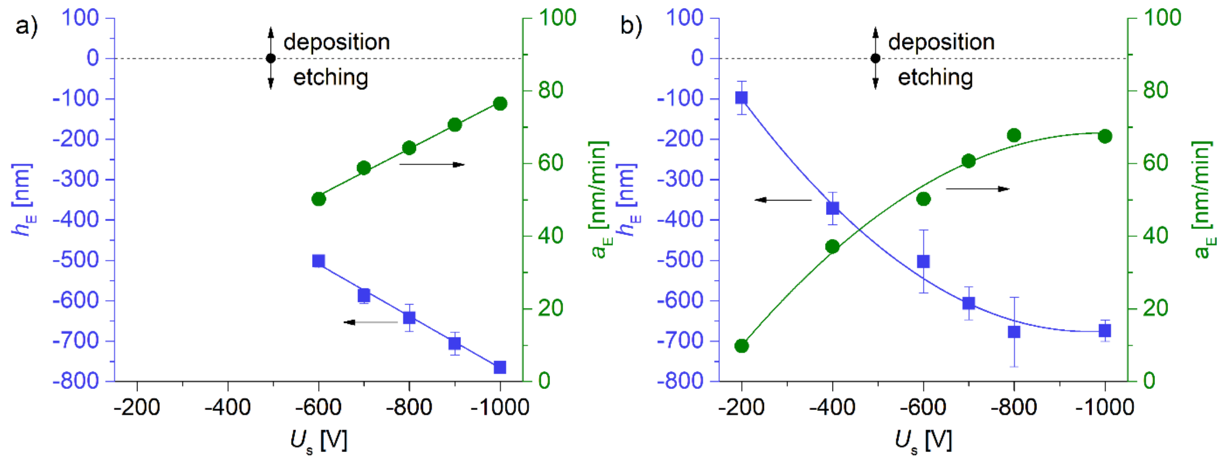


**Fig. 3.** Etching rate $a_E$ and etched depth $h_E$ in (a) Si (100) substrate and (b) steel 15330 substrate as a function of the etching substrate bias voltage $U_s$. The substrates were etched at low target power density $W_t \approx 0.75$ W/cm$^2$, $p_{Ar}$ = 1.0 Pa, $d_{s\text{-}t}$ = 80 mm, $T_s$ = 300 °C for 10 min.

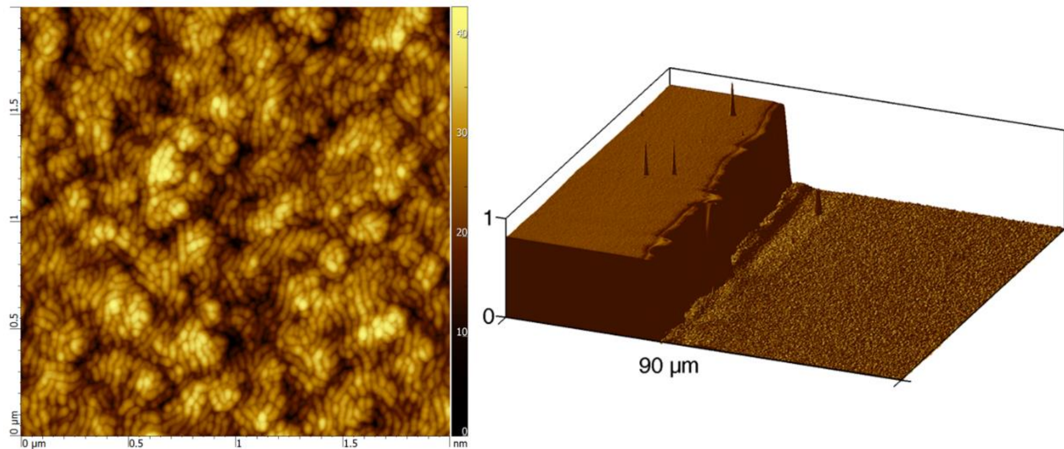


**Fig. 4.** (a) The typical AFM surface morphology and (b) 3D cross-section of the step after the etching of Si (100) substrate at the DC bias voltage $U_s$ = -600 V.

*In summary*, the adhesion of the W films deposited on Si (100) and steel 15330 after their DC plasma etching at $U_s$ = -800 V, and low power $W_t \approx 0.75$ W/cm$^2$ magnetron discharge, is very good. Neither delamination, nor buckling in the films up to 3 µm thick with high compressive macro-stress up to 3 GPa were observed.

## 2. Deposition conditions

It is well known that film microstructure (grain/crystallite size), structure (texture), mechanical and physical properties (hardness, $H/E^*$, elastic recovery, macro-stress, density, adhesion, roughness, etc.) are influenced by the energy $E$ delivered into the growing film by the film-forming particles (atoms and ions) and substrate temperature [85,88,217,218]. Therefore, in order to deposit hard W film with $H$ > 15 GPa, the microstructure of such film must be non-

columnar or with nanocolumns, dense, without voids, and fine-grained with crystallite size approaching to ~10 nm [219]. This microstructure requirement corresponds to aforementioned transition zone T in structure zone diagram (SZM) according to Thornton [87] or later SZM modified by Anders [80].

In order to investigate the effect of the microstructure on the $H$ of the W films, the films were deposited at (1) low density (LD) discharge conditions using DC power supply (PS), and (2) high density (HD) discharge conditions using AC unipolar pulsed PS, see Fig. 5. The target power density $W_t$ was 2.3 W/cm$^2$ in case of the film series deposited at the LD conditions, while the target power density in a micro-pulse $W_{t\,pulse}$ was 40 times higher, i.e. ~100 W/cm$^2$ and the average target power density in a macro-pulse $W_{ta}$ was 50 W/cm$^2$ in case of the film series deposited at the HD conditions. Additionally, in both cases of discharge conditions, the films were deposited at the varied DC negative substrate biases $U_s$. Deposition conditions, physical and mechanical properties of the W films deposited on Si (100) substrate are summarized in Table 2.

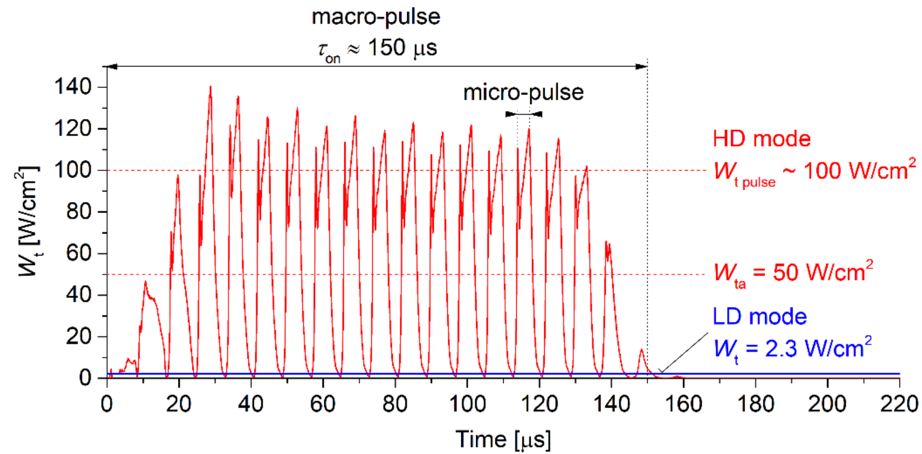


**Fig. 5.** Waveforms of the target power density $W_t$ for low-density discharge (LD) and high-density discharge (HD), generated by DC and AC unipolar pulsed power supply, respectively, using the W target.

The energy $E$ was delivered into the W films in two ways, by: (1) ion bombardment and their energy $E_{bi}$, and (2) high density discharge with high ion ($W^+$ and $Ar^+$) flux to substrate. Because, the films grown at low ion energy and high flux have a different structure and different properties from films deposited with high ion energy but low ion flux [80]. In the first way, the energy $E_{bi}$ was controlled by the $U_s$ and calculated from the formula $E_{bi} = (U_s i_s)/a_D$; where $i_s$ is the substrate ion current density and $a_D$ is the deposition rate of the film [220]. Both values $i_s$ and $a_D$ are given in Table 2. In the latter case, both the $a_{Dp}$ and $i_{sap}$ averaged per a macro-pulse are more than 15 times higher in a case of the W film deposition at the HD conditions than at the LD conditions, see Table 2. In addition, I. Velicu et al. has recently measured the fraction of ionized W metals ($W^+$) in the DC sputtering at $W_{ta}$ = 5 W/cm$^2$, which is low 3 % [122]. Therefore, we assume that fraction of $W^+$ in a case of the HD conditions, with regard to very similar discharge in [122], can be 10–20 %. Higher fraction of $W^+$ at the expense of $Ar^+$, leads to higher film densification, due to higher momentum transfer of the $W^+$ to the film, where the atomic masses of W and Ar, are 184 amu and 40 amu, respectively.

**Table 2**: Deposition conditions, physical and mechanical properties of the W films deposited on Si (100) substrate. The films were sputtered at: $T_s$ = 300 °C, $d_{s-t}$ = 80 mm, DC substrate bias using (i) DC PS with target power density $W_t$ = 2.3 W/cm$^2$ or (ii) AC pulsed unipolar PS DORA/1 with average target power density in a macro-pulse $W_{ta}$ = 50 W/cm$^2$ at $\tau_{on}/T$ = 0.15. Mechanical properties were measured on Si (100) substrate at a load of 10 mN using Berkovich indenter. Where $i_{sap}$ and $a_{Dp}$ are the ion current density in a pulse and deposition rate in a pulse, respectively, in the case of use AC PS. Deposition rate averaged per period $a_D$ can be calculated by using the formula: $a_D = a_{Dp} \times \tau_{on}/T$.

| $p_T$ | $U_s$ | $i_s$, $i_{sap}$ | $a_D$, $a_{Dp}$ | $E_{bi}$ | $i_{sap}/a_{Dp}$ | $h$ | $\sigma$ | $H$ | $E^*$ | $H/E^*$ | $W_e$ | $D$ | discharge |
|---|---|---|---|---|---|---|---|---|---|---|---|---|---|
| [Pa] | [V] | [mA/cm$^2$] | [nm/min] | [MJ/cm$^3$] | [Amin/mm$^3$] | [nm] | [GPa] | [GPa] | [GPa] | | [%] | [nm] | conditions |
| 0.5 | -50 | 0.63 | 32 | 0.6 | 0.012 | 2 230 | -2.8 | 17.2 | 292 | 0.059 | 38 | 30 | Low-density |
| 1.0 | -50 | 0.44 | 27 | 0.5 | 0.010 | 2 440 | -2.1 | 16.2 | 300 | 0.054 | 36 | 33 | |
| 1.0 | -75 | 0.59 | 33 | 0.8 | 0.011 | 3 130 | -2.5 | 15.6 | 308 | 0.051 | 33 | 31 | |
| 1.0 | -100 | 0.63 | 32 | 1.2 | 0.012 | 2 890 | -1.9 | 14.7 | 310 | 0.047 | 30 | 33 | |
| 1.0 | -150 | 0.66 | 21 | 2.8 | 0.019 | 1 980 | -1.9 | 13.7 | 299 | 0.046 | 30 | 23 | |
| 1.0 | -200 | 0.72 | 16 | 5.6 | 0.028 | 2 090 | -2.1 | 16.2 | 297 | 0.055 | 36 | 19 | |
| 0.5 | -50 | 11.6 | 507 | 0.7 | 0.014 | 3 000 | -2.6 | 21.5 | 296 | 0.073 | 45 | 14 | High-density |
| 0.5 | -75 | 12.0 | 453 | 1.2 | 0.016 | 2 680 | -2.5 | 21.2 | 299 | 0.071 | 44 | 16 | |
| 0.5 | -100 | 12.1 | 391 | 1.9 | 0.019 | 2 000 | -2.1 | 20.8 | 293 | 0.071 | 44 | 16 | |
| 0.5 | -125 | 13.0 | 234 | 4.3 | 0.034 | ≈1 900* | ~-2.0 | 19.7 | 288 | 0.069 | 42 | 17 | |
| 0.5 | -150 | 13.3 | 204 | 5.3 | 0.036 | ≈1 000* | ~-1.5 | 19.2 | 274 | 0.070 | 43 | 16 | |

*the film is not uniform due to its high re-sputtering caused by high $E_{bi}$

## 3. Structure and microstructure

The structure and crystallite size $D$ of the W films deposited on Si (100) and steel 15330 substrate were characterized by X-ray diffraction. Figs. 6 and 7 show the evolution of XRD patterns and $D$ of the W films deposited on Si (100) and steel 15330 substrate, respectively, as a function of the ion bombardment controlled by $U_s$. Moreover, Fig. 6a,b shows and compares XRD patterns of the W films deposited on Si (100) at the LD and HD conditions, respectively. All W films deposited with varied $|U|_s \leq 50$ V and at both conditions (LD and HD), exhibit the thermodynamically stable (low-$T$) α-phase with body-centered-cubic (bcc) structure and strong preferred orientation (110) and a weak contribution of (200), (211) and (220) planes. Presence of metastable β-phase was observed neither in Fig. 6 nor in Fig. 7. Let us to recall, that metastable β-phase occur only when (1) the total pressure $p_T$ during deposition exceeds 3 Pa [148] and/or (2) the oxygen impurity content in the film is high ~14 at.% [149–152]. The oxygen content measured by EDX in all our deposited W films is lower than 10 at.%. It well correlates with the aforementioned presumption where the β-phase in the W films with O content <10 at.% is not observed.

Figure 6 shows that with increasing $U_s$ above -75 V, the (110) peak intensity of α-W phase in the film deposited on Si (100) decreasing, suggesting that the crystallinity of the films decreasing. Decreasing in crystallinity is due to generation of the defects and disorders in the film microstructure caused by high ion bombardment at $|U_s| \geq 100$ V. Similar result was observed elsewhere [151]. All XRD diagrams, see Figs. 6 and 7, show a shift in the diffraction patterns to lower 2Θ angles, due to compressive stress in the W films.

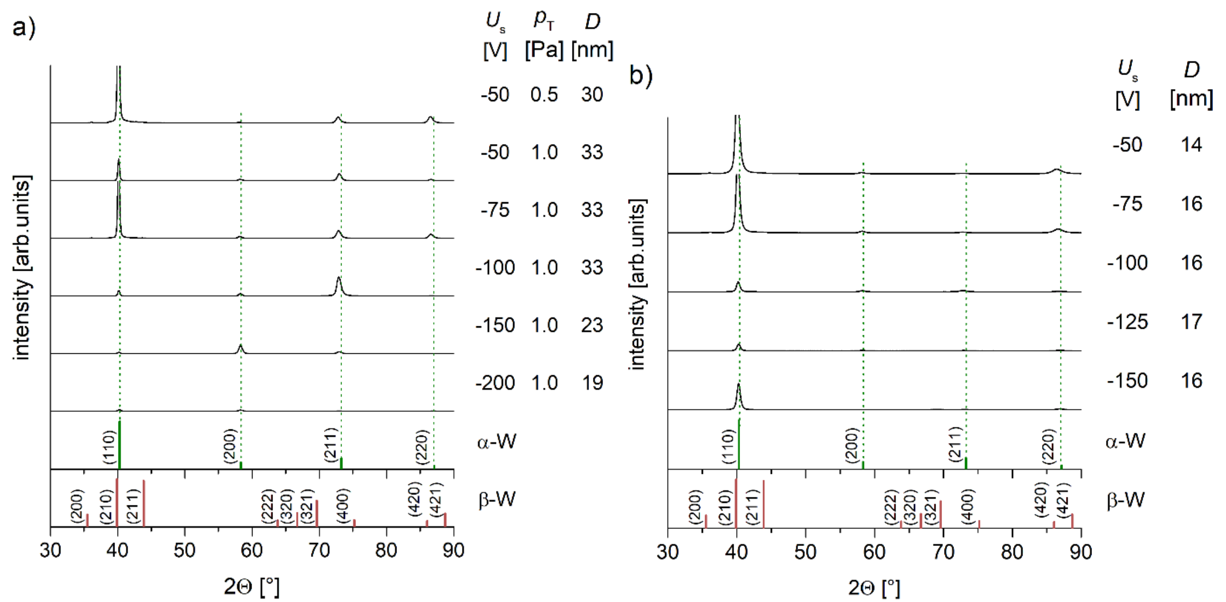


**Fig. 6.** XRD patterns of W films deposited at (a) the LD conditions, and (b) the HD conditions onto Si (100) substrates as a function of the substrate bias $U_s$.

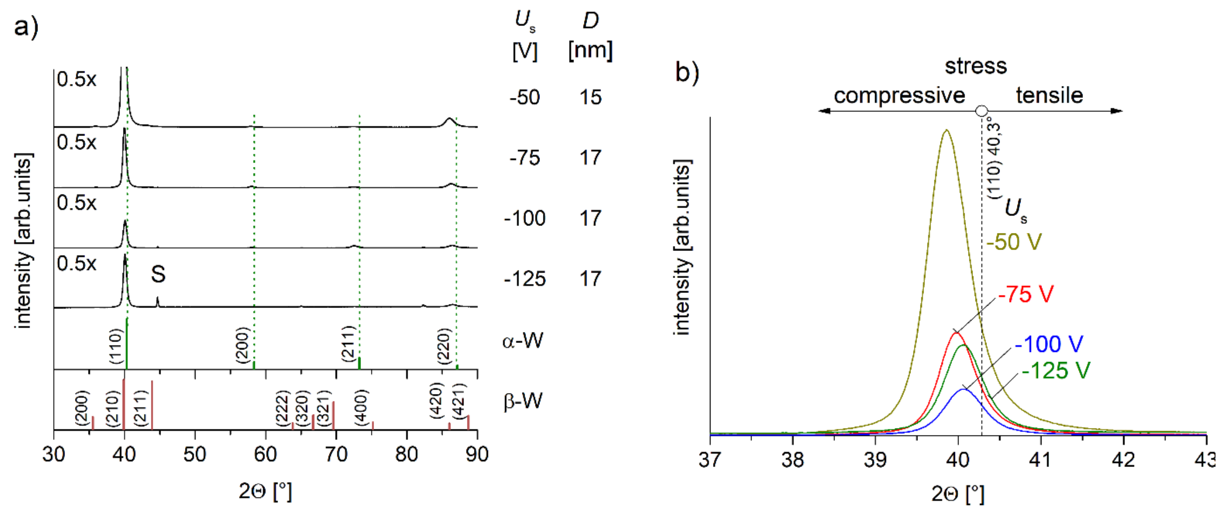


**Fig. 7.** XRD patterns of W films in (a) the 2Θ range 30–90°, and (b) the α-W (110) region, deposited at the HD conditions onto steel 15330 substrates as a function of the substrate bias $U_s$. The W film sputtered at $U_s$ = -150 V is not given due to its high re-sputtering.

It was found that increasing $U_s$ did not lead to significant change in the crystallite size of the W films deposited at the HD conditions, while $D$ decreased in the films deposited at the LD conditions with increased $U_s$. Whereas, the films deposited at the HD conditions exhibited two times lower $D_{HD}$ ~ 16 nm than that of the films with $D_{LD}$ ~ 33 nm deposited at the LD conditions, see Fig. 8. The W films deposited at the HD conditions onto steel 15330 substrate exhibit the same crystallite size $D_{HD}$ ~ 17 nm to those films deposited onto Si (100) substrate, see Figs. 7 and 6b, respectively.

Lower crystallite size in the W films deposited at the HD conditions than that of in the films deposited at the LD conditions is due to higher momentum transfer by aforementioned higher flux (approximately more than 4 times higher) of the $W^+$ with high atomic mass (184 amu) than Ar (40 amu) into the film.

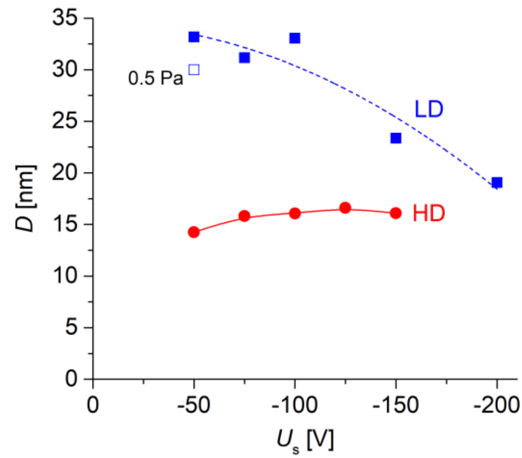


**Fig. 8**. Crystallite size $D$ of W films deposited at the LD and HD conditions onto Si (100) as a function of substrate bias $U_s$. Deposition conditions are summarized in Table 2.

## 4. Mechanical properties

The mechanical properties ($H$, $E^*$, $H/E^*$, and $W_e$) and macro-stress ($\sigma$) of the deposited W films as a function of $U_s$, are summarized in Table 2. The $H$, $H/E^*$, and $W_e$ as a function of $D$ is shown in Fig. 9a,b. Table 2 shows that increasing of the $U_s$ occurs to decreasing of the $H$ in the W films deposited at the LD conditions, while increasing $U_s$ has no significant effect on the mechanical properties of the W films deposited at the HD conditions on Si (100). Fig. 9 shows that decreasing $D$ result in increasing $H$, $H/E^*$, and $W_e$ of the films. Decreased of the $D$ up to ~14 nm in the W film deposited on Si (100), result in increased $H$ up to 21.5 GPa, $H/E^*$ up to 0.073 and $W_e$ up to 45 %. Enhanced $H$ of the W film is due to grain boundary strengthening described by Hall–Patch relation [23]. When the grain size decreases, in the nanocrystalline material up to ~10 nm, the dislocation has no space for motion, the pile-ups and formation of Frank-Read sources, thus to the strengthening of those material occurs.

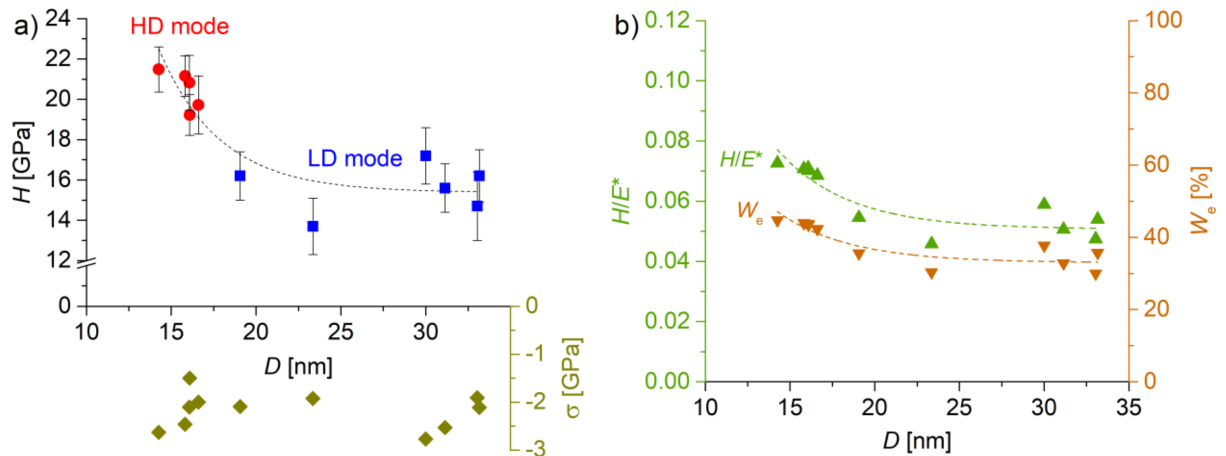


**Fig. 9**. (a) Hardness $H$ and macro-stress $\sigma$, and (b) $H/E^*$ and elastic recovery $W_e$ of the W films deposited at the LD and HD conditions onto Si (100) substrate as a function of crystallite size $D$.

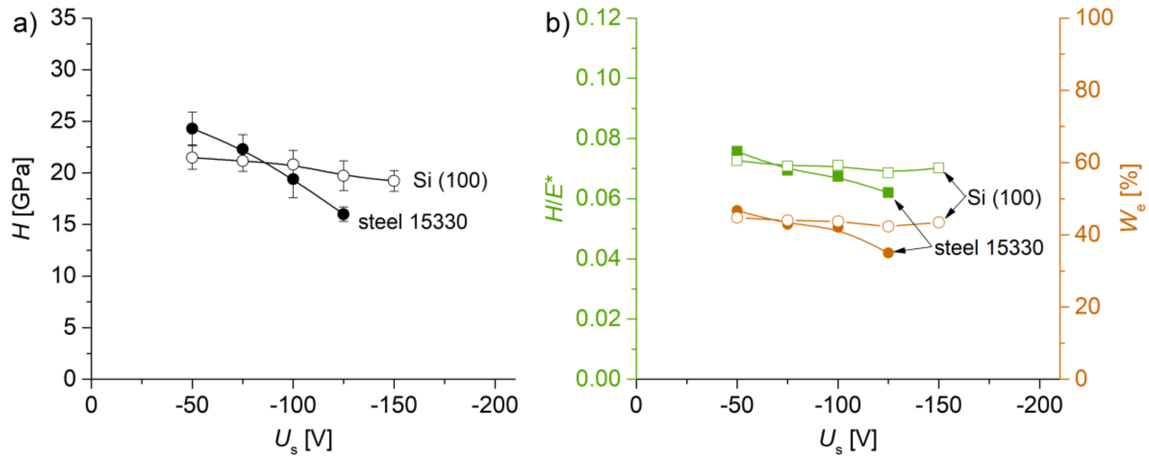


**Fig. 10**. Comparison of (a) hardness $H$, and (b) $H/E^*$ and elastic recovery $W_e$ of W films deposited at the HD conditions onto Si (100) and steel 15330 substrate as a function of substrate bias $U_s$. The films were sputtered at: $T_s$ = 300°C, $d_{s\text{-}t}$ = 80 mm, $p_{Ar}$ = 0.5 Pa.

Residual macro-stress ($\sigma$) plays a significant role in the mechanical reliability of the films. In the absence of thermal stress, tensile macro-stress ($\sigma > 0$) in hard metal films is caused by grain boundary shrinkage and compressive macro-stress ($\sigma < 0$) is caused by ion/atomic peening [221]. Peening process, is the process where the $\sigma < 0$ in the film is generated by its bombardment by energetic sputtered atoms, ions, and/or backscattered Ar neutrals (usually from high atomic mass target), at low sputtering-gas pressures [22]. Thus, the energetic particles bombardment of the film during its growth process produces defects as vacancies, gas incorporation, interstitials, dislocations, etc. that causes $\sigma < 0$. The presence of the compressive stress in the W films is confirmed by the XRD peaks shifting to lower angles, see Figs. 6 and 7. Fig. 9 shows that the $\sigma < 0$, measured by the Si (100) substrate curvature using Stoney's formula, in our W films was between -2 and -3 GPa, and suggesting that it is caused by aforementioned peening process at low $p_{Ar} \leq 1$ Pa. By comparing both $H$ and $\sigma$ in Fig. 9a and Table 2, it can be seen that with increasing of the $\sigma < 0$, the $H$ of the W films increases, but this effect is less significant compared to the effect of the $D$ on the $H$ of these films.

Comparison of the $H$, $H/E^*$, and $W_e$ values of the W films deposited on Si (100) and steel 15330 substrates at the HD conditions is shown in Fig. 10. The figure shows that highest $H_{steel\ 15330}$ = 24.3 GPa and $H_{Si\ (100)}$ = 21.3 GPa were achieved in the W film deposited at $U_s$ = -50 V on steel 15330 and Si (100) substrate, respectively. With further increasing of the $U_s$, the $H$ gradually decreasing in the both W films deposited on Si (100) and steel 15330 substrate. The $\sigma < 0$ of the W films deposited on the Si (100) decreases from 2.6 GPa to 2.0 GPa, with increasing negative $U_s$ from 50 V to 150 V, respectively, see Table 2, while values of the $\sigma$ in the films deposited on the steel 15330 substrate is unknown. However, Fig. 7b clearly show that with increasing $U_s$ the shift of the (110) peak to lower angles occurs. Considering the fact that compressive stress causes shift in the diffraction peaks to lower angles, it means that compressive stress in the W films deposited on the steel 15330 substrate decreases with increasing $U_s$. Decreasing of the $H$ may be due to incorporation of Ar atoms (not measured) into the W films, due to high $Ar^+$ bombardment controlled by $U_s$. Decreasing of the $H/E^*$, and $W_e$ values correspond to decreasing of $H$.

*In summary*, the W films deposited at low energy $E_{bi}$ of ions of 0.7 MJ/cm$^3$ and at high-density discharge $W_{t\ pulse}$ ~100 W/cm$^2$ exhibit enhanced $H$ up to 21.5 GPa on Si (100) substrate, and 24.3 GPa on steel 15330 substrate, enhanced $H/E^*$ up to 0.073 and $W_e$ up to 45 %, and good adhesion where no delamination was observed even at high compressive macro-stress up to 2.8 GPa. The enhanced mechanical properties of W films are due to grain boundary strengthening mechanism, where the crystallite size $D$ decreases to ~14 nm. The decreasing in $D$ is attributed to high-density discharge conditions.

# D. Thermal stability of β-(Ti,W) films deposited by magnetron sputtering

J. Musil, Š. Kos, S. Zenkin, Z. Čiperová, D. Javdošňák, R. Čerstvý

Surface & Coatings Technology 337 (2018) 75–81

# 1. Structure and microstructure of high-T β-Ti films

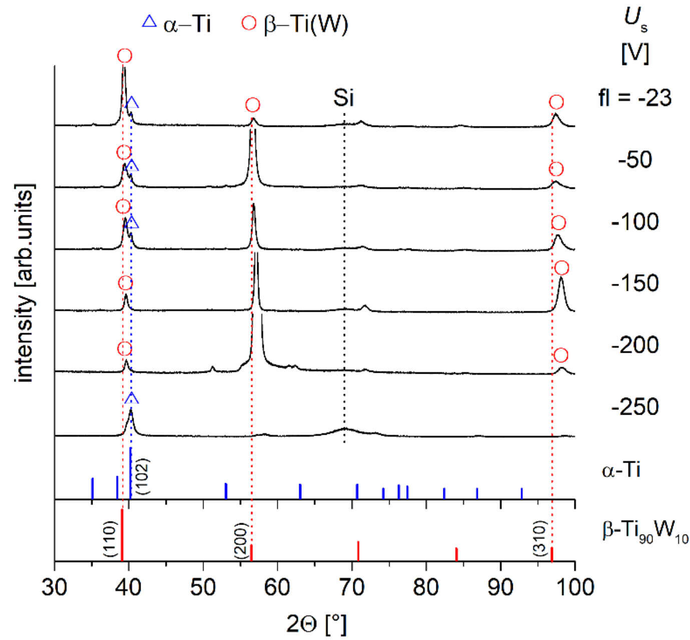


**Fig. 1.** Evolution of XRD structure of Ti-W film DC sputtered by unbalanced magnetron at: $I_d$ = 1 A, $T_s$ = 450°C, $d_{s\text{-}t}$ = 60 mm, and $p_{Ar}$ = 1 Pa as a function of negative DC substrate bias $U_s$.

The as-deposited Ti-W films sputtered by magnetron equipped with W target overlapped by the Ti plate with $Ø_{i\ Ti}$ = 30 mm exhibit fixed 12±1 at.% W content. Ti and W exhibit complete mutual solid solubility in the β phase at temperatures between the solidus and the critical temperature of the miscibility gap [157]. The structure of sputtered Ti-W alloy films was characterized by X-ray diffraction. Fig. 1 shows the evolution of structure of the Ti-W film with increasing ion bombardment expressed by the energy $E_{bi}$ controlled by the substrate bias $U_s$. This energy was calculated from the formula $E_{bi} = (U_s i_s)/a_D$; where $i_s$ is the substrate ion current density and $a_D$ is the deposition rate of the film [220]. The as-deposited films deposited at the low ion bombardment $U_{fl}$ = -23 V exhibit a bcc structure with a strong (110) texture, while the films deposited at high ion bombardment $U_s$ from -50 V to -200 V exhibit a bcc structure with a strong (200) texture. The crystallite size $D_{bcc}$ of the β-(c-Ti(W)) films increases with increasing negative substrate bias $U_s$ (Fig. 1) and affects its mechanical properties of the films, see Table 1. Fig. 1 shows the co-existence of the high-T β-(bcc-Ti(W)) and low-T α-(h-Ti(W)) phases in the nc-(Ti,W) films sputtered at $|U_s| \leq 100$ V, while at $|U_s|$ = 150–200 V, the films exhibit high-T β-(bcc-Ti(W)) phase only. The co-existence of both the high-T and low-T phases in the films sputtered at $|U_s| \leq 100$ V may be explained by relatively high deposition temperature $T_s$ = 450 °C which may causes partial decomposition of the metastable high-T phase to high-T and low-T phase. A strong ion bombardment $U_s$ = -250 V of the (Ti,W) film results in a re-sputtering of the film, where the high-T β-phase disappear and the low-T α-phase is formed only. The X-ray reflections corresponding to the β-phase and α-phase are denoted by open circles and triangles, respectively.

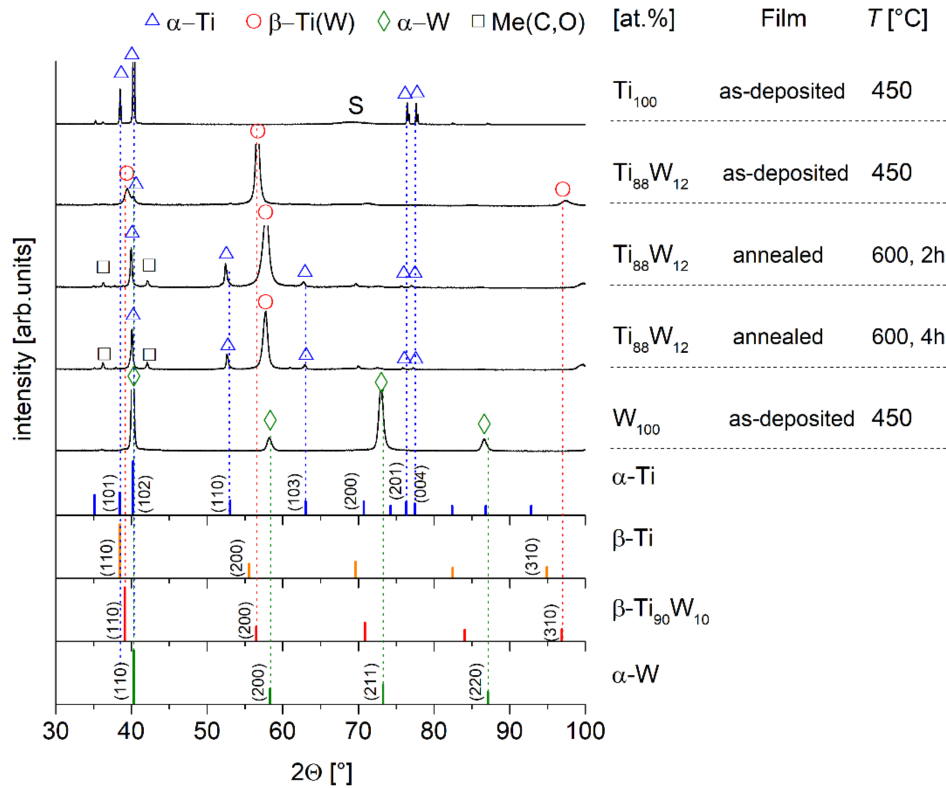


**Fig. 2.** XRD structure of Ti, Ti-W alloy, and W films DC sputtered by unbalanced magnetron at: $I_d$ = 1 A, $T_s$ = 450 °C, $d_{s-t}$ = 60 mm, $U_s$ = -50 V and $p_{Ar}$ = 1 Pa, and evolution of the structure of as-deposited Ti-W film after its annealing in inert Ar atmosphere at $T_a$ = 600 °C for 2 and 4 h at 1 Pa. All films were deposited on Si (100). The XRD pattern of a pure Ti and W film is given for comparison. Where Me(C,O) were identified peaks as a oxides or carbides of Ti or W.

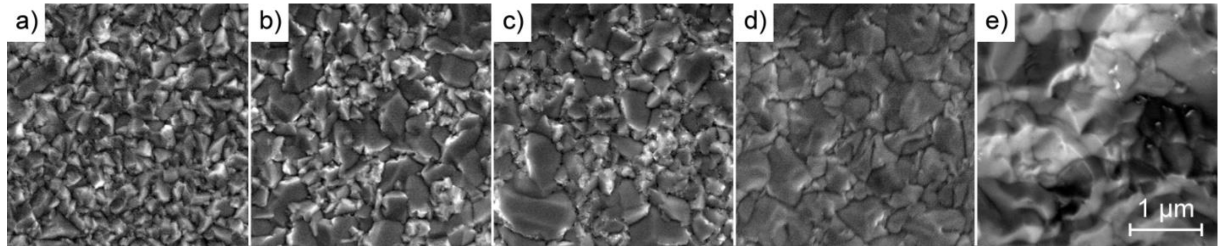


**Fig. 3.** Surface morphology SEM images of Ti-W alloy films deposited at varied DC substrate bias $U_s$: (a) $U_{fl}$ = -23 V, (b) -50 V, (c) -100 V, (d) -150 V, and (e) -200 V.

Fig. 2 shows the structure of (i) the pure Ti and W film sputtered at $U_s$ = -50 V, (ii) the as-deposited $Ti_{88}W_{12}$ film sputtered at $U_s$ = -50 V, and (iii) the thermally annealed β-$Ti_{88}W_{12}$ film at the annealing temperature $T_a$ = 600 °C for 2 h and 4 h. The surface morphology of the Ti-W films sputtered from $U_{fl}$ to -200 V is shown in Fig. 3. The figure shows that increasing of the ion bombardment result in qualitatively observed increasing of the grain coarsening of the as-deposited $Ti_{88}W_{12}$ films. This observation well correlates with aforementioned increasing of the $D_{bcc}$ with the $U_s$ (see Table 1).

**Table 1:** Deposition parameters, physical and mechanical properties of pure Ti and W, as-deposited Ti-W alloy films and annealed Ti-W alloy film DC sputtered by unbalanced magnetron at: $I_d$ = 1 A, $T_s$ = 450 °C, $d_{s-t}$ = 60 mm, $U_s$ = -50 V and $p_{Ar}$ = 1 Pa. Where $D_{bcc}$ and $D_h$ are crystallite size approximately estimated from bcc and hexagonal phase using Scherrer formula, respectively.

| Film | $U_s$ [V] | $i_s$ [mA/cm$^2$] | $a_D$ [nm/min] | $E_{bi}$ [MJ/cm$^3$] | $\sigma$ [GPa] | $H$ [GPa] | $E^*$ [GPa] | $H/E^*$ | $W_e$ [%] | $D_{bcc}$ [nm] | $D_h$ [nm] | crystal structure |
|---|---|---|---|---|---|---|---|---|---|---|---|---|
| Ti film | | | | | | | | | | | | |
| As-deposited Øi $_{Ti}$ = 0 mm | -50 | 1.0 | 100 | 0.08 | 0.5 | 2.7 | 138 | 0.02 | 15 | | 54 | h |
| $Ti_{88}W_{12}$ alloy film | | | | | | | | | | | | |
| As-deposited Øi $_{Ti}$ = 30 mm | $U_{fl}$ = -23 V | 1.0 | 137 | 0.11 | 0.1 | 4.8 | 115 | 0.04 | 29 | 18 | | h + bcc |
| | -50 | 1.2 | 147 | 0.24 | 0.1 | 5.0 | 111 | 0.05 | 31 | 24 | | h + bcc |
| | -100 | 1.3 | 135 | 0.57 | 0.2 | 5.4 | 116 | 0.05 | 31 | 27 | | h + bcc |
| | -150 | 1.5 | 98 | 1.35 | 0.2 | 4.6 | 119 | 0.04 | 28 | 35 | | bcc |
| | -200 | 1.7 | 79 | 2.54 | 0.2 | 4.5 | 117 | 0.04 | 27 | 28 | | bcc |
| | -250 | 1.6 | n.m.* | n.m.* | n.m.* | n.m.* | n.m.* | n.m.* | n.m.* | | 18 | h |
| Annealed at $T_a$ = 600°C, 2 h | -50 | | | | n.m. | 12.9 | 156 | 0.08 | 55 | 14 | 34 | h + bcc |
| Annealed at $T_a$ = 600°C, 4 h | -50 | | | | n.m. | 10.7 | 141 | 0.08 | 49 | 19 | 33 | h + bcc |
| W film | | | | | | | | | | | | |
| As-deposited | -50 | 0.4 | 27 | 0.49 | -2.1 | 16.2 | 300 | 0.05 | 36 | 33 | | bcc |

n.m. means not measured

* not measured due to high re-sputtering of the film

From this experiment the following conclusions can be drawn:

1. The pure Ti film has the low-T α-Ti phase with a hexagonal (h-) structure, i.e. low-T α-(h-Ti), while pure W film has the low-T α-W phase with a bcc structure.
2. The addition of 12 at.% W with bcc structure into the Ti with h- structure results in formation of the high-T β-(bcc-Ti(W)) film in magnetron sputtering.
3. The finding that the difference between structures of added (bcc-W) and host (h-Ti) elements results in the high-T cubic β-(bcc-Ti(W)) film is in accordance with Ref. [155,169].
4. The increasing of the $U_s$ from $U_{fl}$ = -23 V to -150 V of the $Ti_{88}W_{12}$ films results in increasing of the crystallite size from ~18 nm to ~35 nm and conversion of the heterostructural films composed of two: high amount of β-Ti(W) and low amount of α-Ti phases into the homostructural β-Ti(W) films.
5. In formation of the β-phase films a sufficient energy $E_{bi}$ must be delivered into the growing film and the hot material of the created film must be rapidly cooled down to RT.

## 2. Thermal stability of high-T β-phase films

The thermal stability of the high T β-phase film was investigated in detail using its slow thermal annealing. Here, it is worthwhile to note that the thermal annealing is an equilibrium process consisting in slow heating, annealing at a given annealing temperature ($T_a$) and slow cooling down to RT. As an example, the $Ti_{88}W_{12}$ alloy film sputtered at $U_s$ = -50 V was investigated in detail. This as-deposited high-T β-$Ti_{88}W_{12}$ alloy film was iso-thermally annealed in the deposition chamber. Prior to the annealing, the chamber was evacuated to $2\times10^{-3}$ Pa, then the argon gas was introduced into the chamber to set point pressure of 1 Pa, then the film was heated up

to $T_a$ = 600 °C with the heating rate of 10 °C/min, and after the annealing of the film at $T_a$ for 2 h and 4 h, the film was cooled down with the rate of 30 °C/min.

The structure of annealed high-T β-$Ti_{88}W_{12}$ alloy film is shown in Fig. 2. Figure shows that the thermal annealing results in a partial conversion of the homostructural β-(bcc-$Ti_{88}W_{12}$) structure into the heterostructural structure composed of two β-(bcc-$Ti_{88}W_{12}$) and α-(h-$Ti_{88}W_{12}$) phases of different crystal structure. This fact shows that the β-$Ti_{88}W_{12}$ material is metastable. It means that the thermal stability of the β-phase film is limited by a maximum temperature $T_{\beta\text{-phase max}}$. The $T_{\beta\text{-phase max}}$ value can be estimated according to a fact that the post-deposition annealing of the β-$Ti_{88}W_{12}$ alloy film at $T_a$ = 600 °C led to a formation of the heterostructural film, while the as-deposited β-$Ti_{88}W_{12}$ alloy film at $T_s$ = 450 °C is the homostructural (even with very low content of the α-(h-$Ti_{88}W_{12}$) phase, due to aforementioned high $T_s$). It means that the $T_{\beta\text{-phase max}}$ should be between $T_s$ and $T_a$ values, i.e. $T_s < T_{\beta\text{–phase max}} < T_a$. Therefore, we suppose that the $T_{\beta\text{-phase max}}$ is approximately ≈ 525 °C.

*In summary*, it can be concluded that slow annealing of the as-deposited high-T β-(bcc-Ti(W)) film to 600 °C results in its partial conversion to the low-T α-(h-Ti(W)) phase and high-T β-(bcc-Ti(W)) phase, leading to a formation of the heterostructural film composed of a mixture of cubic and hexagonal grains. The β-$Ti_{88}W_{12}$ film is thermally stable to a maximum temperature value $T_s < T_{\beta\text{–phase max}} < T_a$, where $T_{\beta\text{-phase max}}$ is around ≈ 525 °C.

## 3. Mechanical properties of films

The mechanical properties of the sputtered films were investigated as a function of the energy $E_{bi} = f(U_s)$ delivered during their growth by bombarding ions. The $Ti_{88}W_{12}$ films show correlations between the energy $E_{bi}$ and their mechanical properties. The $Ti_{88}W_{12}$ film sputtered at $U_s$ = -50 V shows the effect of a post-deposition annealing on its mechanical properties. Deposition parameters, physical and mechanical properties of the $Ti_{88}W_{12}$ films are given in Table 1. This table compares mechanical properties, macro-stress $\sigma$, crystallite size $D$ of the films with bcc and h structure and crystal structure of the as-deposited pure Ti and W, $Ti_{88}W_{12}$ films and the thermally annealed $Ti_{88}W_{12}$ film.

Main conclusions which can be drawn from Table 1 are the following:

1. The pure Ti film with a hexagonal crystal structure exhibits a very low hardness $H$ = 2.7 GPa, high effective Young's modulus $E^*$ = 138 GPa resulting in very low ratio $H/E^*$ = 0.02 and very low elastic recovery $W_e$ = 15 %. Such films may exhibit a low cracking resistance [85,203].

2. The as-deposited β-$Ti_{88}W_{12}$ film with a bcc crystal structure exhibits approximately two times higher $H$, $W_e$ and $H/E^*$ compared with the pure Ti film. The hardness of the film $H_{Ti88W12}$ ~ 5 GPa well correlates with the hardness $H_{rom}$ = 4.3 GPa calculated according to the rule-of-mixture (rom) [32] considering the measured hardness of pure W ($H_W$ = 16.2 GPa) and pure Ti ($H_{Ti}$ = 2.7 GPa) film.

3. The post-deposition annealed β-$Ti_{88}W_{12}$ film at $T_a$ = 600°C for 2 h and sputtered at $U_s$ = -50 V ($E_{bi}$ = 0.24 MJ/cm$^3$) exhibits compared to the as-deposited film a strong increasing of $H$ (2.5 times), $H/E^*$ (2 times), and $W_e$ (1.7 times). This increasing of $H$, $W_e$ and $H/E^*$ values are due to the conversion of the structure with homostructural β-(bcc-$Ti_{88}W_{12}$) phase into the heterostructural nanocomposite structure composed of two dominant β-(bcc-$Ti_{88}W_{12}$) and α-(h-$Ti_{88}W_{12}$) phases accompanied by change in the crystallite size from $D_{bcc}$ = 24 nm into $D_{bcc}$ = 14 nm and $D_h$ = 34 nm, respectively.

# 4. Cracking resistance of films

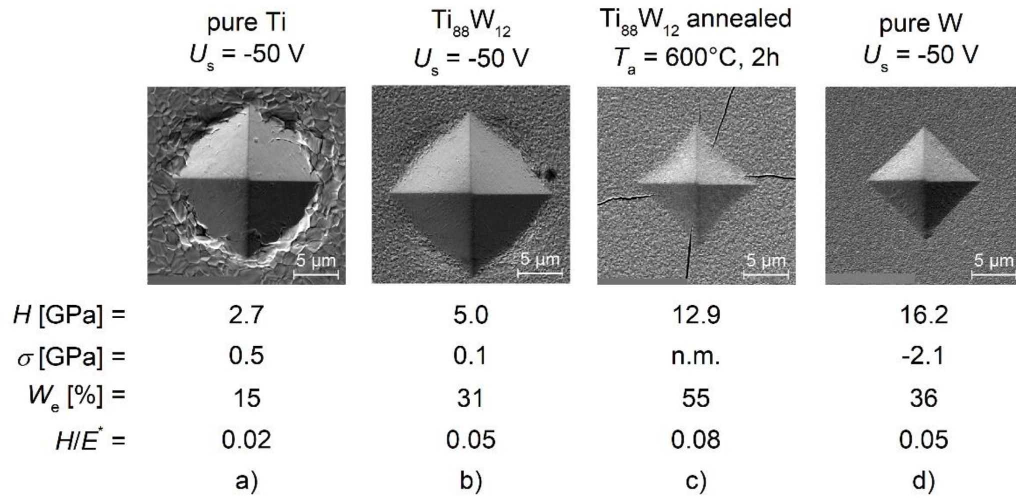


| | a) | b) | c) | d) |
|---|---|---|---|---|
| $H$ [GPa] = | 2.7 | 5.0 | 12.9 | 16.2 |
| $\sigma$ [GPa] = | 0.5 | 0.1 | n.m. | -2.1 |
| $W_e$ [%] = | 15 | 31 | 55 | 36 |
| $H/E^*$ = | 0.02 | 0.05 | 0.08 | 0.05 |

**Fig. 4.** SEM micrographs of the indentations at high loads up to 1 N applied into (a) pure Ti film, (b) $Ti_{88}W_{12}$ film, (c) annealed $Ti_{88}W_{12}$ film, and (d) pure W film, sputtered on Si (100). The indentation depth was 80–90 % of the film thickness.

In order to assess the cracking resistance of the as-deposited and post-deposition annealed $Ti_{88}W_{12}$ alloy film, and the pure metal Ti and W film, the indentation test using Vickers indenter at high loads up to 1 N was performed. The indentation depth was kept between 80 % and 90 % of the film thickness. The typical SEM micrographs of the indentation test are shown in Fig. 4. Figure shows that the soft films (see Fig. 4a,b) with $H \leq 5$ GPa exhibit no cracking even at (1) low elasticity expressed by low elastic deformation: $H/E^* < 0.10$ and $W_e < 60$ % [56], and (2) tensile macro-stress ($\sigma > 0$). This is due to a ductile behavior of such films, where the tensile stress in the films generated by an indenter is released in local plastic deformation.

The hardened heterostructural post-deposition annealed $Ti_{88}W_{12}$ alloy film with $H$ = 12.9 GPa exhibits multiple cracks, see Fig. 4c. The cracking of such film may be explained by low $H/E^* < 0.10$ and $W_e < 60$ % and absence of the compressive macro-stress which cannot inhibit the crack formation and propagation. Whereas, the hard and pure W film with $H$ = 16.2 GPa and also low $H/E^* < 0.10$ and $W_e < 60$ % exhibits no cracks around the indent, see Fig. 4d. The enhanced cracking resistance of the hard and pure W film is due to its high compressive macro-stress ($\sigma < 0$) which exceeds 2 GPa.

*In summary*, the soft and ductile metallic films (pure Ti and as-deposited $Ti_{88}W_{12}$ alloy) with hardness $H \leq 5$ GPa exhibit no cracks even at $H/E^* < 0.10$ and $W_e < 60$ %, while the hard

metallic films (annealed $Ti_{88}W_{12}$ alloy and pure W) with $H > 10$ GPa exhibit enhanced resistance to cracking when their compressive macro-stress ($\sigma < 0$) is sufficiently high, to inhibit the crack formation and propagation, even in the films with low $H/E^{*} < 0.10$ and $W_e < 60$ %.

# E. Tribological properties and oxidation resistance of tungsten and tungsten nitride films at temperatures up to 500 °C

D. Javdošňák, J. Musil, Z. Soukup, S. Haviar, R. Čerstvý, J. Houska

Tribology International 132 (2019) 211–220

## 1. Structure, microstructure and mechanical properties

**Table 1:** Deposition conditions, mechanical properties and elemental compositions of the $WN_x$ films where $i_{sap}$ is the average substrate ion current density in macro-pulse, $E_{bi} = \tau_{on}/T.(U_s.i_{sap})/a_D$ is the average energy of the ions delivered to the film in a macro-pulse, $I_{dp}$ and $U_{dp}$ are the average discharge current and voltage in a macro-pulse, respectively, $a_D$ is the deposition rate averaged over the deposition and $D$ is the average size of crystallites.

| $p_{N2}$ | $x$= [N]/[W] | composition | O | $i_{sap}$ | $E_{bi}$ | $I_{dp}$ | $U_{dp}$ | $a_D$ | $\sigma$ | $H$ | $E^*$ | $H/E^*$ | $W_e$ | $D$ |
|---|---|---|---|---|---|---|---|---|---|---|---|---|---|---|
| [Pa] | | [at.%] | [at.%] | [mA/ cm$^2$] | [MJ/ cm$^2$] | [A] | [V] | [nm/ min] | [GPa] | [GPa] | [GPa] | [-] | [%] | [nm] |
| 0.00 | 0 | $W_{100}$ | 7 | 13.7 | 1.0 | 8.5 | 470 | 60 | -2.9 | 23 | 294 | 0.08 | 47 | ~14 |
| 0.05 | 0.20 | $W_{83}N_{17}$ | 13 | 11.3 | 0.9 | 7.5 | 530 | 58 | -3.0 | 31 | 296 | 0.10 | 59 | ~20 |
| 0.125 | 0.27 | $W_{79}N_{21}$ | 5 | 8.3 | 0.8 | 7.2 | 550 | 54 | -3.5 | 33 | 287 | 0.11 | 65 | ~7 |
| 0.175 | 0.56 | $W_{64}N_{36}$ | 5 | 7.1 | 0.6 | 6.8 | 590 | 53 | -3.3 | 34 | 304 | 0.11 | 64 | ~7 |
| 0.25 | 0.64 | $W_{61}N_{39}$ | 3 | 6.2 | 0.6 | 6.6 | 610 | 49 | -3.2 | 34 | 293 | 0.12 | 65 | ~7 |
| 0.50 | 1.5 | $W_{40}N_{60}$ | 1 | 1.5 | 0.4 | 6.2 | 650 | 20 | -2.3 | 22 | 204 | 0.11 | 62 | ~4 |

Table 1 shows that increasing nitrogen partial pressure from 0 to 0.5 Pa leads to increasing nitrogen content in the films from 0 to 60 at.% (increasing $x$ from 0 to 1.5). The oxygen content of 1–13 at.%, resulting from the residual atmosphere and from the high formation enthalpy of tungsten oxides ($\Delta H_{WO2}$ = -571 to -595 kJ/mol and $\Delta H_{WO2.7\text{-}3}$ = -743 to -853 kJ/mol [121], compared to e.g. $\Delta H_{\beta\text{-}W2N}$ = -22 kJ/mol [121,222] or -71 kJ/mol [223] and $\Delta H_{\delta\text{-}WN}$ = -15 kJ/mol [121,222]), was neglected when calculating the $WN_x$ stoichiometry.

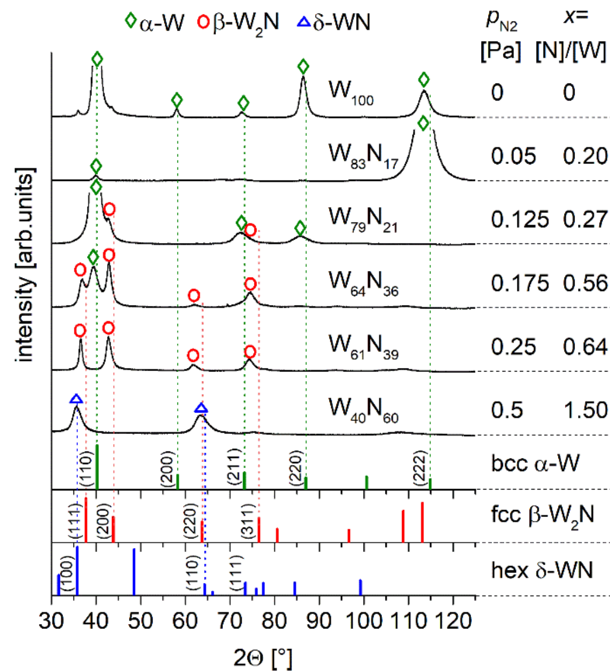


**Fig. 1.** XRD patterns of the as-deposited $WN_x$ films on Si (100). The films were deposited at $T_s$ = 300°C, $d_{s\text{-}t}$ = 80 mm, $p_T$ = 0.5 Pa, $U_s$ = -50 V using DORA AC unipolar power supply and the duty cycle was $\tau_{on}/T_p$ = 0.15.

The phase structure, shown in Fig. 1, corresponds to the amount of nitrogen. The pure tungsten film exhibits polycrystalline structure of the stable (low-*T*) α-W phase with a strong (110) preferential orientation and a weak contribution of (200), (211) and (222) planes. Addition of 17 at.% of N leads to a (222) texture of the α-W phase. The film with 21 at.% of N exhibits polycrystalline structure of two phases with a broad (110) peak from the α-W phase and a weak (200) peak from the metastable (high-*T*) β-$W_2N$ phase. The film with an intermediate N content of 36 at.% exhibits the same two phases with orientations α-W (110) and β-$W_2N$ (111) and (200). The film with further enhanced N content of 39 at.%, does not contain α-W anymore, and there is a polycrystalline structure of β-$W_2N$ with broad peaks from (111) and (200) planes. The film deposited in a pure $N_2$ atmosphere exhibits 60 at.% of N and a polycrystalline structure of hexagonal δ-WN phase with (100) and (110) preferential orientations.

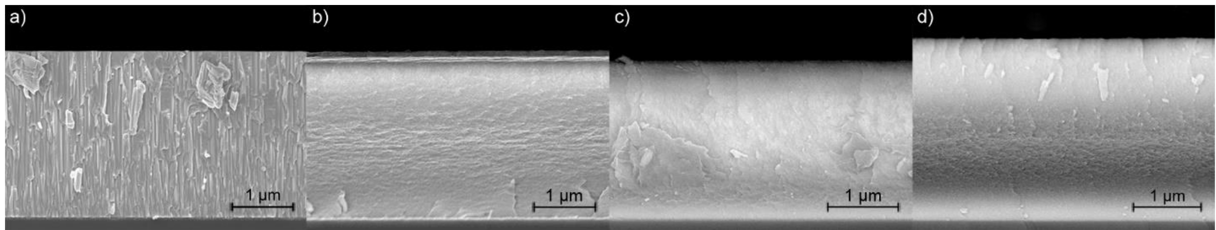


**Fig. 2.** SEM cross-section morphology images of the as-deposited $WN_x$ films with stoichiometry (a) $x = 0.20$, (b) $x = 0.27$, (c) $x = 0.64$ and (d) $x = 1.5$.

The mean grain size $D$ (perpendicular to the film surface) was roughly estimated from broadening of the diffraction peak using the Scherrer equation [195]. For the pure W film, and the film with 17 at.% of N, i.e. for $x \leq 0.20$, the grain size calculated from the α-W peaks (110) and (222) is approximately 14 nm and 20 nm, respectively. After the addition of more nitrogen into the films, the grain size calculated from α-W (110) or (222), β-$W_2N$ (200) and δ-WN (100) peaks decreases to $D = 7$ nm. The lowest $D = 4$ nm at $x = 1.5$ implies that the N excess ($x$ over 1.0) particularly suppresses the grain growth. These findings well correlate with decreasing ion flux density from plasma onto the substrate ($i_{sap}$) with increasing $x$ (see Table 1). The subsequently weaker energetic ion bombardment leads to lower mobility of the impinging atoms (W, N and WN molecules) and increasing concentration of defects. Furthermore, these findings well correlate with the microstructure shown in Fig. 2: while the $WN_x$ films with $x \leq 0.20$ exhibit columnar microstructure, films with $x \geq 0.27$ exhibit fine-grained and non-columnar microstructure.

The evolution of the mechanical properties with $p_{N2}$ is shown in Fig. 3. The pure W film exhibits very high $H$ up to 23 GPa (compared with e.g. bulk $H = 3.9$ GPa [145]) and $E^* = 294$ GPa, but low ratio $H/E^* = 0.08$ and low $W_e = 47$ %. The very high film hardness is caused by (i) low grain size $D = 14$ nm and (ii) high compressive macro-stress $\sigma$ of about -3 GPa. The addition of nitrogen into the films leads to (i) increasing $H$ up to 34 GPa (at $H/E^* = 0.11$–$0.12$ and $W_e = 64$–$65$ %) achieved at $0.27 \leq x \leq 0.64$, followed by (ii) decreasing $H$ down to 22 GPa (at $H/E^* = 0.11$ and $W_e = 62$ %) achieved for the poorly crystalline film at the highest $x = 1.5$. In parallel to the phase composition and crystal size changes (the highest $H$ values achieved at $x$

from 0.27 to 0.64 correspond to the fine-grained films with $D = 7$ nm), the $H$ evolution is correlated with that of $\sigma$. Possible reasons of the high compressive macro-stress in $WN_x$ include (i) bombardment by energetic backscattered (Ar, N and $N_2$) and sputtered (W) particles (not significantly scattered by working gas due to a low product $p_T \times d_{s\text{-}t}$) in general , and (ii) the subsequent presence of interstitial N atoms in particular [224]. The stress causes (i) a shift of the α-W, β-$W_2N$ and δ-WN diffraction peaks to lower angles, (ii) the aforementioned increase of the hardness [123] and (iii) decrease of the Young's modulus due to crystal lattice deformation. Because the $WN_x$ films with $x \geq 0.27$ exhibit high elasticity and resistance to plastic deformation expressed in terms of $H/E^* > 0.10$ and $W_e > 60$ %, and low $|\sigma|$ below 2 GPa (Table 1 and Fig. 3), they constitute promising candidates for films resistant to wear [8,9,71,225] and cracking [55,85,226].

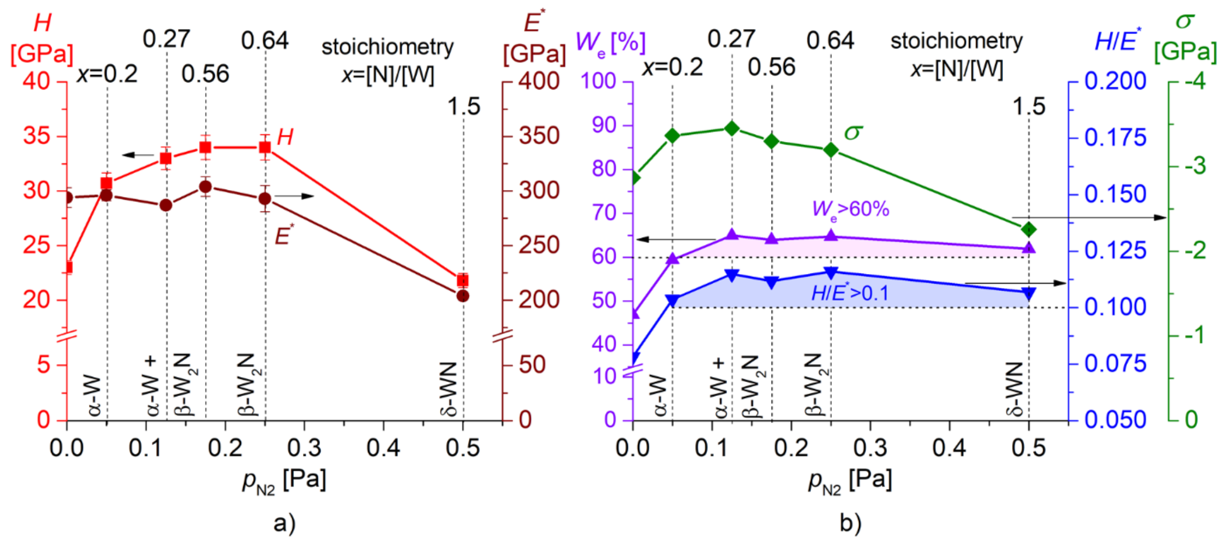


**Fig. 3.** Mechanical properties (a) $H$, $E^*$ and (b) $W_e$, $H/E^*$ and $\sigma$ of $WN_x$ films as a function of nitrogen partial pressure $p_{N2}$.

## 2. Tribological properties at temperatures up to 500°C

Investigation of the tribological properties was performed on five qualitatively different $WN_x$ films: α-W, N-containing α-W, α-W + β-$W_2N$, β-$W_2N$ and δ-WN (N-content 0, 17, 21, 39 and 60 at.% and stoichiometry $x = 0$, 0.20, 0.27, 0.64 and 1.5, respectively). Note that the first 50–200 m is the so-called "running-in stage" (see Fig. 4), where the value of $\mu$ is distorted by roughness of both contact surfaces. In this stage both surfaces are cleaned from contaminations and polished. After the running-in stage, the so-called "steady-state stage" begins. In order to properly describe the durability of the tested film, we propose that the latter stage must span sufficiently (i) long distance (>100 m not including the running-in stage) and (ii) long time (> 60 min, especially if the film is exposed to high temperature at which oxidation occurs). Figure 4 shows that the mean value $\mu = 0.7$ measured only at sliding distance up to ≈ 100 m (running-in stage) differs significantly from $\mu = 0.59$ measured at a sliding distance from ≈ 100 m to 1000 m (steady-state stage).

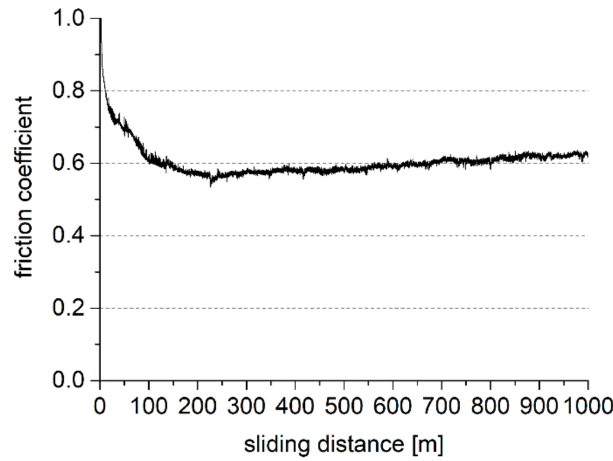


**Fig. 4.** Typical evolution of the friction coefficient of the $WN_x$ film with $x = 1.5$ at $T = 250$ °C as a function of sliding distance of the $Al_2O_3$ ball.

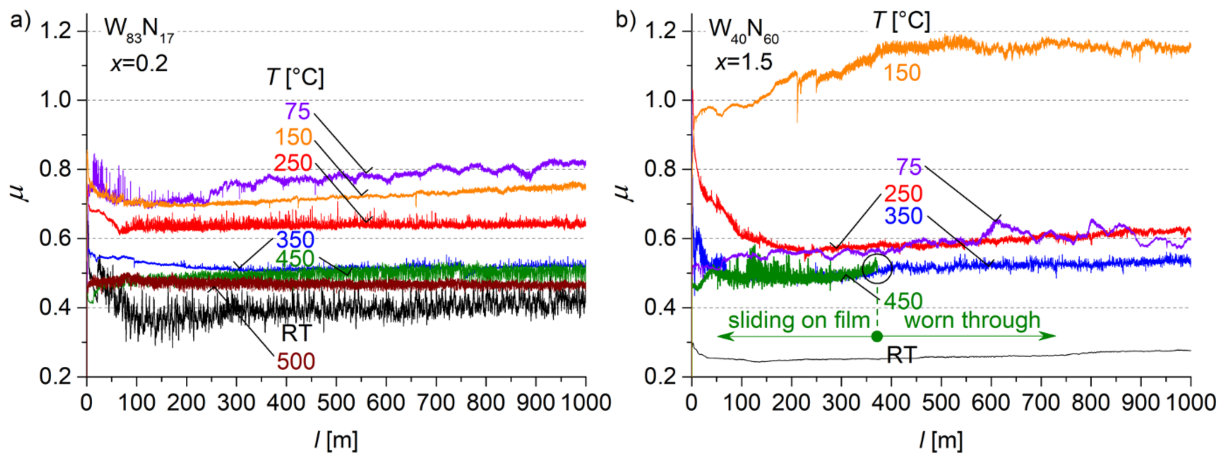


**Fig. 5.** Friction curves at varied test temperature $T$ for the $WN_x$ films with: (a) $x = 0.20$ and (b) $x = 1.5$.

**Table 2:** Summary of the durability test of the $WN_x$ films at $T = 450$–$500$ °C, in terms of the sliding distance $l'$ at which the films were worn through ($l' = 1000$ m for films which withstood the test).

| $x=$ [N]/[W] | composition [at.%] | phase | $h$ [nm] | $l'$ (450 °C) [m] | $l'$ (500 °C) [m] |
|---|---|---|---|---|---|
| **0** | $W_{100}$ | α-W (110) | 2 770 | **1000** | **400** |
| **0.20** | $W_{83}N_{17}$ | α-W (222) | 2 400 | **1000** | **1000** |
| **0.27** | $W_{79}N_{21}$ | α-W+β-$W_2N$ | 2 830 | **690** | - |
| **0.64** | $W_{61}N_{39}$ | β-$W_2N$ | 2 800 | **540** | - |
| **1.5** | $W_{40}N_{60}$ | δ-WN | 2 720 | **360** | - |

Figure 5 shows the evolution of the friction coefficient $\mu$ with sliding distance $l$ at various temperatures $T$ for two representative $WN_x$ films, one with low-N content ($x = 0.20$; Fig. 5a) and one with high-N content ($x = 1.5$; Fig. 5b). The figure shows that all tested films achieve the steady-state after the first $l = 50$–$200$ m (or after $l = 380$ m for $x = 1.5$ and $T = 150$ °C). In the steady state, the $\mu$ of all films increases with $l$. This emphasizes the importance of using long (1000 m) sliding distance. The friction curve shown in Fig. 5b for $x = 1.5$ and $T = 450$ °C exhibits strong oscillations (not displayed) for $l > 360$ m, i.e. after the film got worn through.

Table 2 summarizes the durability of all $WN_x$ films at $T$ = 450 °C (all films) and 500 °C (films which withstood the test at 450 °C), in terms of the sliding distance $l'$ at which the films were worn through.

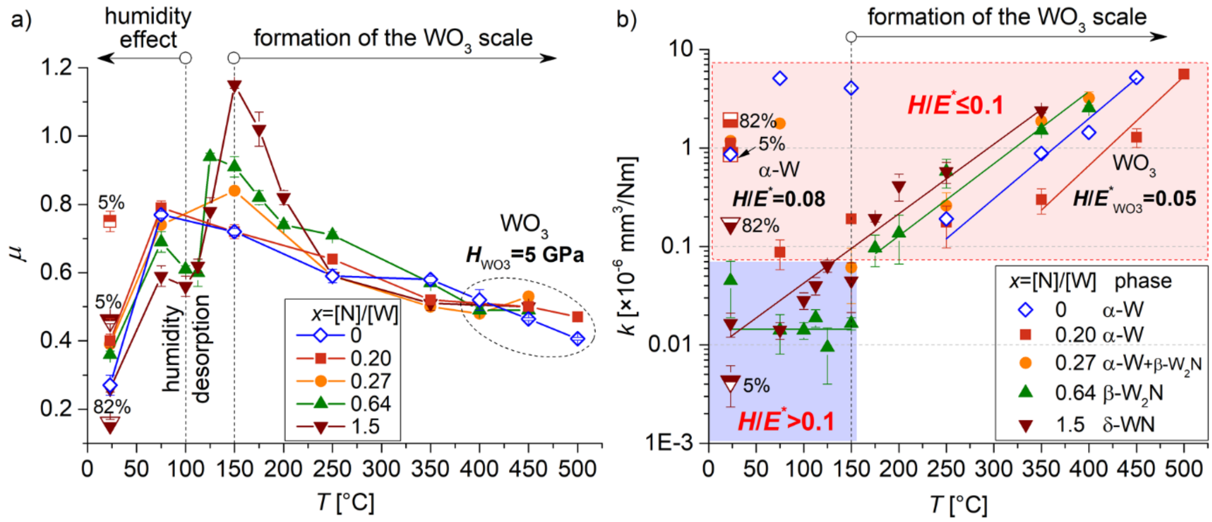


**Fig. 6.** Tribological properties (a) friction coefficient $\mu$ and (b) wear rate $k$ of $WN_x$ films as a function of the test temperature $T$. Symbols with empty bottom, full symbols and symbols with empty top correspond to relative humidity of 5, 30–50 and 82 %, respectively.

Figure 6a shows the $\mu$ of the $WN_x$ films as a function of the test temperature $T$ and stoichiometry $x$. All films exhibit almost similar trends $\mu(T)$. Independently of $x$, the lowest $\mu$ values in ambient air (RH = 30–50 %) between 0.26 (both $x = 0$ and $x = 1.5$) and 0.40 ($x = 0.20$) were obtained at RT. This can be explained by the surface hydration mechanism accompanied by the reaction: $WN_x + H_2O \rightarrow WO_3 + NH_3$, lowering the shear strength [5,210] which is proportional to $\mu$ [2]. Note that the low-$T$ $\mu$ values correlate with film hardness [227] ($x = 0$ and 1.5 lead to a low $\mu = 0.26$ at low $H$ = 22–23 GPa, while $0.20 \leq x \leq 0.64$ leads to higher $\mu$ up to 0.40 at high $H$ = 31–34 GPa), due to the fact that shear strength increases with $H$ [2]. Furthermore, the figure shows the effect of humidity during the measurement. Low RH = 5 % (dry nitrogen) led to e.g. enhanced $\mu$ from 0.4 to 0.75 at $x = 0.20$ or from 0.28 to 0.46 at $x = 1.5$, while high RH = 82% (moist environment) led to e.g. lowered $\mu$ from 0.28 to 0.16 at $x = 1.5$. The overall decrease of $\mu$ with increasing RH and vice versa (more significant at higher $x$) is due to the aforementioned surface hydration.

At $T$ of 75–100 °C, water molecules desorb from the film surface, the water lubrication mechanism fails, and $\mu$ immediately increases to 0.56–0.80. With further increase of $T$ to 125–150 °C, $\mu$ of the high-N content films with $x = 0.64$ and $x = 1.5$ further increases to its highest values of $\mu = 0.94$ and $\mu = 1.15$, respectively. These high $\mu$ values obtained at high-N contents may be caused by mechanical properties of the corresponding nitrides and/or N-rich oxynitrides (higher N/O ratio in the wear track at higher N content in the films was also confirmed by EDX, see Fig. 7). With $T$ increasing above 150 °C, $\mu$ decreases to 0.46–0.53 at 450 °C due to a formation of lubricious $WO_3$ scale on the $WN_x$ sliding surfaces. The monoclinic $WO_3$ phase belongs to the group of easy-to-shear Magnéli phases [228] with low shear strength, and thus leads to a decrease of the friction coefficient according to Hertzain contact model shown in [2]. For

previous observations of the lubricating role of $WO_3$ see [229–231]. While the presented trends are comparable to those observed previously, tested at $l < 200$ m and $L = 5$ N (and in a narrower $x$ range) [124,177], the quantitative $\mu$ values are different (particularly between 100 and 200 °C) due to the lower load $L = 2$ N (higher load leads to lower $\mu$ [2]).

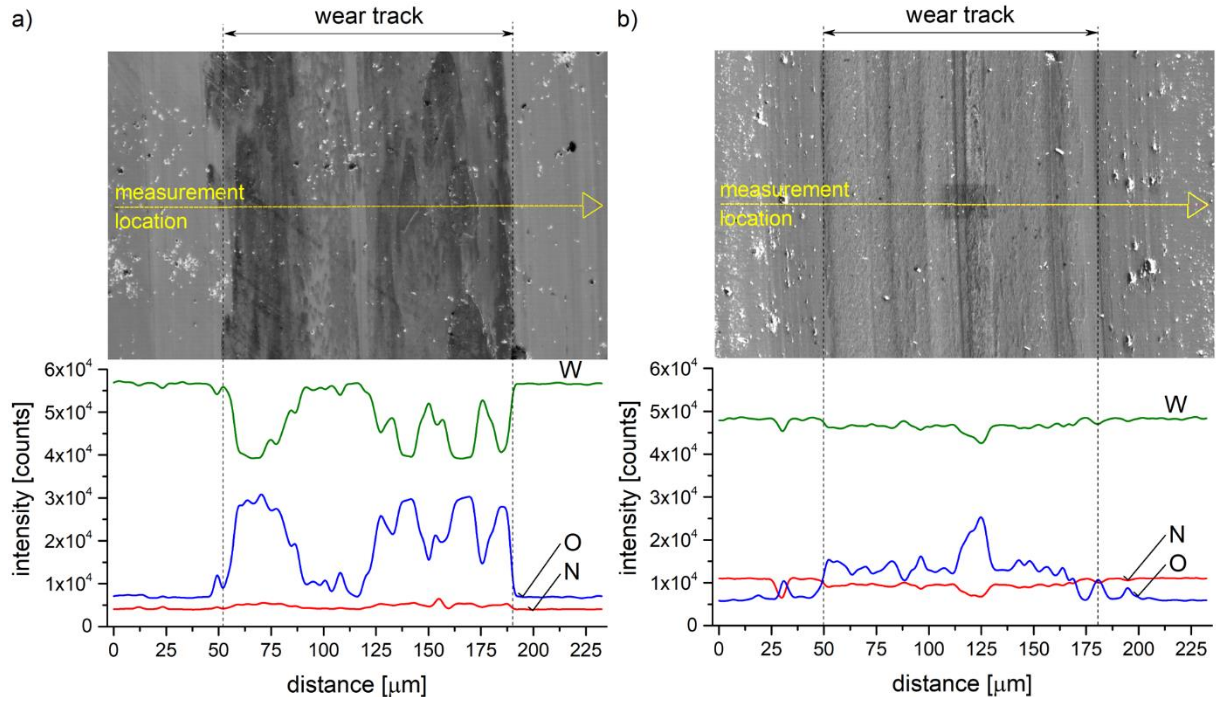


**Fig. 7.** Qualitative composition (W, O and N) of the wear track of the $WN_x$ films with (a) $x = 0.20$ and (b) $x = 1.5$, tested at $T = 150$°C, as obtained by EDX (the EDX measurement location is given by the horizontal arrows).

Figure 6b shows the evolution of the wear rate $k$ of the $WN_x$ films as a function of the test temperature $T$ and stoichiometry $x$. In the $T$ range from RT to 150 °C, the films dominated by the α-W phase ($x \leq 0.27$) exhibit relatively high $k$ up to $5\times10^{-6}$ mm$^3$/Nm. These high $k$ values can be attributed to the brittleness of the α-W phase (let us recall the low ratio $H/E^* = 0.08$ and elastic recovery $W_e = 47$ % at $x = 0$ shown in Fig. 3 and Table 1). On the other hand, the films dominated by the β-$W_2N$ and δ-WN phase ($x \geq 0.64$) with high $H/E^* = 0.11$–$0.12$ and $W_e = 62$–$65$ % exhibit in the same $T$ range very low $k = 0.01$–$0.06\times10^{-6}$ mm$^3$/Nm. Collectively, the results show that (i) if the contact surface of a film exhibits high $H/E^* > 0.1$ and high $W_e > 60$%, the enhanced resistance to wear is observed (similar results were also observed in [227]), and (ii) the wear resistance of the films is given by mechanical properties of the dominant crystalline phase, rather than by the overall mechanical properties. As an example of the latter finding, note that the film characterized by $x = 0.27$ is dominated by the brittle α-W phase (see Fig. 1) with $H/E^* = 0.08$ and $W_e = 47$ % (see Fig. 3) and therefore exhibits high $k$ up to $2\times10^{-6}$ mm$^3$/Nm despite its high overall $H/E^* = 0.11$, high elastic recovery $W_e = 65$ % and fine-grained non-columnar microstructure. In other words, the amount of β-$W_2N$ phase is sufficient to affect the mechanical properties, but insufficient to affect the tribological properties.

Again, the figure 6b shows the effect of humidity during the measurement at RT. It was found that $k$ decreases from 1.92 to 0.86 $\times10^{-6}$ mm$^3$/Nm and from 0.17 to $0.004\times10^{-6}$ mm$^3$/Nm with

decreasing RH from 82 % to 5 % for $x = 0.20$ and 1.5, respectively. The high $k$ at high RH = 82 % is due to the aforementioned surface hydration and formation of $WO_3$, which not only leads to low $\mu$ (Fig. 6a) but which is also soft and brittle ($H_{WO3} = 4–5$ GPa and $H/E^*_{WO3} = 0.05–0.06$) easy-to-wear (Fig. 6b). The effect of surface hydration is more pronounced in high-N content than in low-N content $WN_x$ films, confirming the importance of the reaction $WN_x + H_2O \rightarrow WO_3 + NH_3$.

In the case of $WN_x$ films with $x \leq 0.27$ dominated by the brittle α-W phase ($H/E^* = 0.08$ and $W_e = 47$ %), the $k(T)$ dependence is not necessarily monotonic (as in the case of $x \geq 0.64$ films) because the formation of a small amount of lubricious $WO_3$ can decrease the wear rate of these brittle ($H/E^* < 0.1$) films. This phenomenon was clearly observed in two cases: (i) for the W film ($x = 0$) wear rate decreased from $4\times10^{-6}$ mm$^3$/Nm to $0.2\times10^{-6}$ mm$^3$/Nm with $T$ increasing from 150 °C to 250 °C, and (ii) for the $WN_x$ film ($x = 0.27$), the wear rate decreased from $2\times10^{-6}$ mm$^3$/Nm to $0.06\times10^{-6}$ mm$^3$/Nm with $T$ increasing from 75 °C to 150 °C. The oxidation of tungsten in the wear tracks is qualitatively shown by EDX in Fig. 8 ($x = 0$ in the aforementioned range $T = 150–250$ °C) and Fig. 9 ($x = 0.27$ in the aforementioned range $T = 75–150$ °C). The films with lower wear rate (Figs. 8b and 9b) exhibit much smoother and narrower wear tracks.

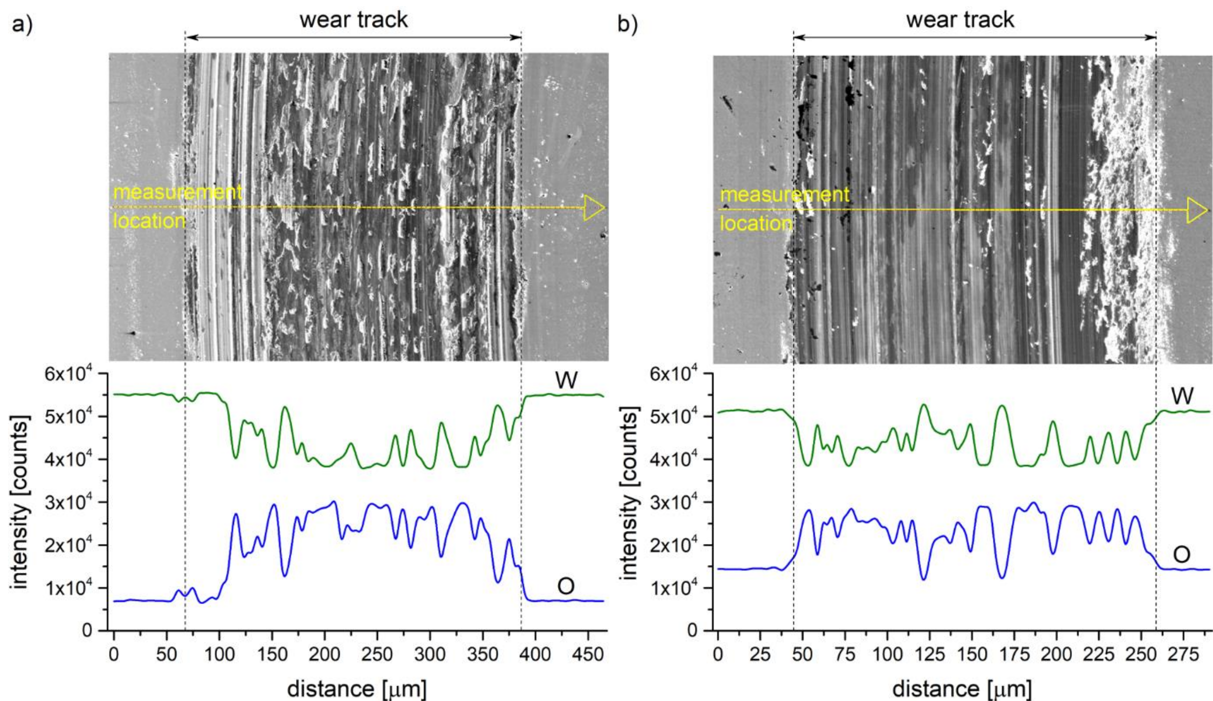


**Fig. 8.** Qualitative composition (W and O) of the wear track of the W films with $x = 0$ tested at (a) $T = 150$ °C ($k = 4\times10^{-6}$ mm$^3$/Nm) and (b) $T = 250$ °C ($k = 0.2\times10^{-6}$ mm$^3$/Nm). The EDX measurement location is given by the horizontal arrows.

With $T$ increasing above 150 °C ($x \geq 0.27$ films) – 250 °C ($x \leq 0.20$ films), formation of a high amount (unnecessarily high for the lubricating purposes) of lubricious $WO_3$ leads to steeply increasing $k$ from the order of $0.01\times10^{-6}$ – $0.1\times10^{-6}$ mm$^3$/Nm to the order of $1\times10^{-6}$ mm$^3$/Nm because as pointed out above, the $WO_3$ phase is not only lubricating but also brittle and easy-to-wear. The oxidation resistance exhibits a non-monotonic dependence on $x$, and is the best at

$x = 0.20$ (see also the discussion in Sec. 3.3). For example, the maximum measurable $k \approx 6\times10^{-6}$ mm$^3$/Nm (leading to wearing the films through for the given sliding distance and film thickness) corresponds to temperatures (slightly above) 450, 500, 400, 400 and 350 °C for $x = 0$, 0.20, 0.27, 0.64 and 1.5, respectively.

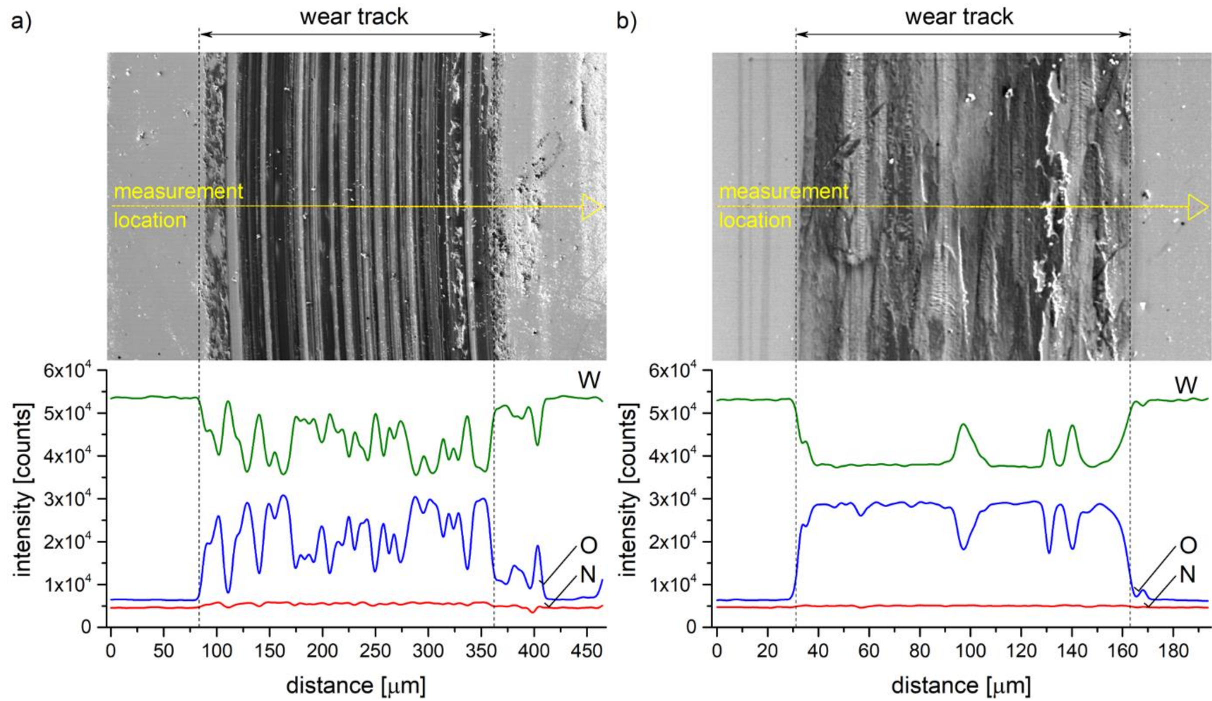


**Fig. 9.** Qualitative composition (W, O and N) of the wear track of the $WN_x$ films with $x = 0.27$ tested at (a) $T = 75$ °C ($k = 2\times10^{-6}$ mm$^3$/Nm) and (b) $T = 150$ °C ($k = 0.06\times10^{-6}$ mm$^3$/Nm). The EDX measurement location is given by the horizontal arrows.

The wear rate of $Al_2O_3$ (increasing with $T$) ball is shown in Table 3. The wear of the ball at $T \leq 150$ °C is accompanied by abrasion, while at $T > 150$°C, the oxidation wear occurs.

**Table 3:** The wear rate of $Al_2O_3$ ball of representative $WN_x$ films, one with low-N content ($x = 0.20$) and one with high-N content ($x = 1.5$).

| Test temperature $T$ [°C] | $x = 0.20$ Ball wear rate [$10^{-9}$ mm$^3$/Nm] | $x = 1.5$ Ball wear rate [$10^{-9}$ mm$^3$/Nm] |
|---|---|---|
| RT | 0.1 | 3.1 |
| 150 | 2.8 | 1.4 |
| 250 | 15.2 | 13.8 |
| 350 | 22.3 | 51.4 |
| 450 | 51.4 | Film was worn-out |

# 3. Oxidation resistance at temperatures up to 500 °C

The $WO_3$ formation was further studied in more detail for one film with low-N content ($x = 0.20$) and one film with high-N content ($x = 1.5$). While Fig. 7 shows for these two films some oxidation in the wear tracks at 150 °C, Fig. 10 confirms that the oxidation becomes much

stronger at 350 °C (strong but inhomogeneous oxidation at $x = 1.5$) and especially 500 °C (strong homogeneous oxidation across whole wear track [not yet observable at 350 °C] at $x = 0.20$).

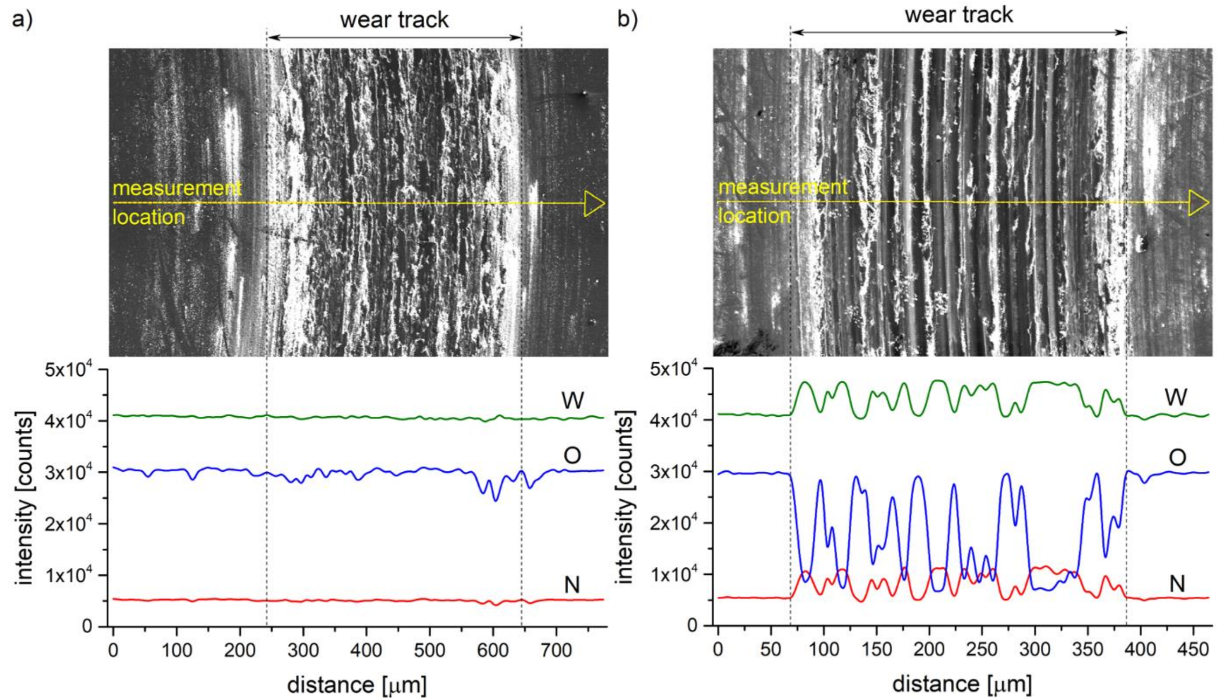


**Fig. 10.** Qualitative composition (W, O and N) of the wear track of the $WN_x$ films with (a) $x = 0.20$ at $T = 500$ °C and (b) $x = 1.5$ at $T = 350$ °C, as obtained by EDX (the EDX measurement location is given by the horizontal arrows).

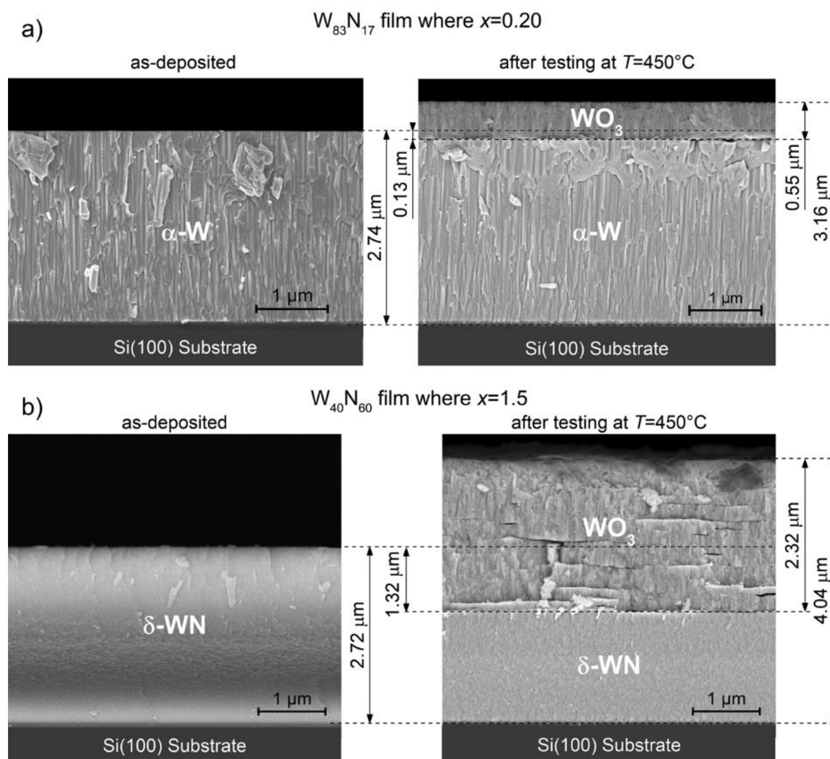


**Fig. 11.** Typical cross-sections images captured by SEM of the (a) $x = 0.20$ and (b) $x = 1.5$ $WN_x$ films as-deposited (left) and after the tribological test at $T = 450$ °C in ambient air for 333 min (right).

The cross-sections shown in Fig. 11 allow one to observe the volume expansion resulting from the oxidation at 450 °C for 333 min: the as-deposited thicknesses of 2.74 µm ($x$ = 0.20) and 2.72 µm ($x$ = 1.5) increased to 3.16 µm and 4.04 µm, respectively, due to a significantly higher volume of the oxide per W atom ($V_{WO3}$ = 31.83 cm$^3$/mol compared to $V_{α–W}$ = 9.95 cm$^3$/mol, $V_{β–W2N}$ = 10.58 cm$^3$/mol and $V_{δ–WN}$ = 12.34 cm$^3$/mol). The figure also shows cracks in the $WO_3$ scale (particularly in the thicker one in Fig. 11b), which may be explained by the volume expansion and which may contribute to the high wear rate of $WO_3$. The elemental composition of $WO_3$ scale on the film surface, as measured by EDX, indicates understoichiometric $WO_3$ and is almost independent of the N content: $W_{0.26}O_{0.73}N_{0.01}$ for $x$ = 0.20 (O/W ratio of 2.8; scale in Fig. 11a) and $W_{0.28}O_{0.71}N_{0.01}$ for $x$ = 1.5 (O/W ratio of 2.5; scale in Fig. 11b).

Figure 12 shows that below $T$ = 350 °C the presence of crystalline $WO_3$ is not observable by XRD, $T$ = 350 °C leads to a weak $WO_3$ peak at $x$ = 0.20 and a strong $WO_3$ peak at $x$ = 1.5, and $T$ = 450 °C leads to strong $WO_3$ peaks at any $x$. Note that these temperatures well correlate with those identified using the evolutions $k(T)$ in the previous section 3.2. Furthermore, decreasing α-W and δ-WN peaks at $x$ = 0.20 (Fig. 12a) and $x$ = 1.5 (Fig. 12b), respectively, are consistent with the fact that $WO_3$ forms at the expense of W and $WN_x$, respectively.

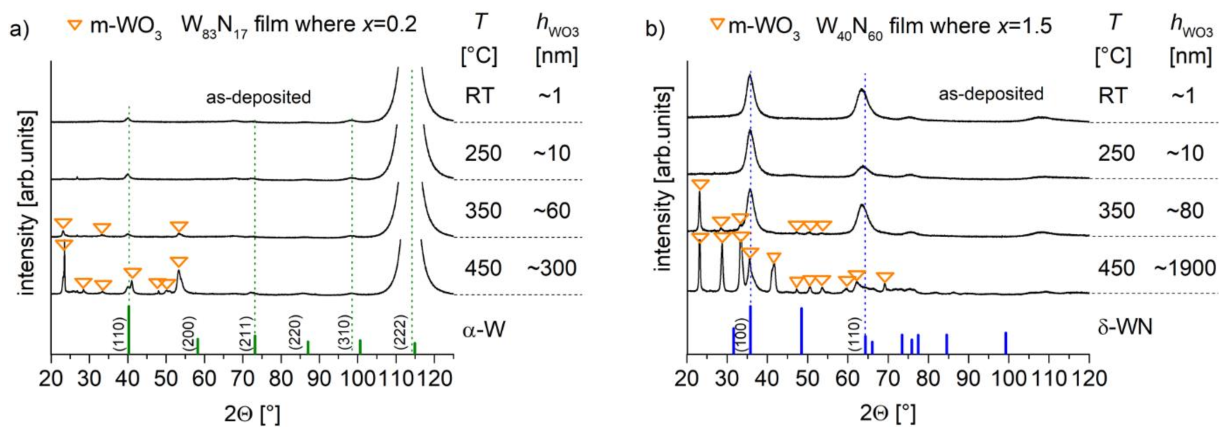


**Fig. 12.** XRD patterns of the $WN_x$ films with (a) $x$ = 0.20 and (b) $x$ = 1.5, as-deposited and after tribological tests at temperature $T$ in ambient air for 333 min. Thickness of the $WO_3$ scale around the wear track, $h_{WO3}$, is shown as well.

The temperature evolution of the $h_{WO3}$ on the surface of all films is quantified in Fig. 13. The thickness was measured by spectroscopic ellipsometry next to the wear tracks, i.e. after isothermal oxidation in ambient air for 333 min. It is shown that slight formation of $WO_3$ (crystalline or amorphous) is observable already at $T$ = 250 °C, i.e. below the temperature limit identified by less sensitive XRD in Fig. 12 (let alone the non-measurable oxidation on the order of nm which can take place at any $T$ [232]). Note that the oxidation inside the wear track is likely to be more intensive, because (i) outside the wear track the oxidation is slowed down by the diffusion of oxygen through the $WO_3$ scale (which exists outside the track but which gets continuously worn off inside the track) and (ii) the temperature induced by friction (due to high local pressures) inside the track can be significantly higher (often up to 1000 °C [232]) than the set temperature outside the track. However, comparison of the evolutions $k(T)$ (Fig. 6b) and

$h_{WO3}(T)$ (Fig. 13) confirms that for non-negligible $h_{WO3}$ (i.e. at $T \geq 250$ °C for any $x$), the wear rate increases with increasing $h_{WO3}$.

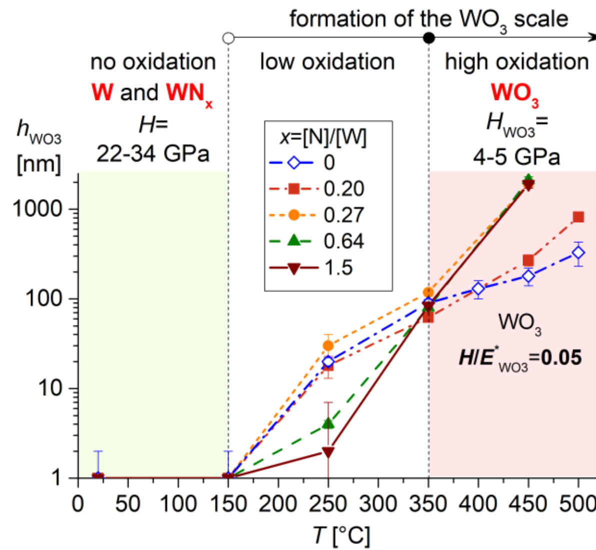


**Fig. 13.** Evolution of the thickness $h_{WO3}$ of the $WO_3$ scale growing on the surface of the $WN_x$ film after the tribological test at temperature $T$ in ambient air for 333 min.

Figure 13 shows that although the slight oxidation at $T = 250$ °C is relatively more intensive at low $x$ values, the slope of the $h_{WO3}(T)$ dependence is much higher at high $T$ and the oxidation at $T \geq 350$°C is much more intensive at high $x$ values. Note that for $T \geq 350$ °C the lower oxidation resistance of fine-grained $WN_x$ films with $x \geq 0.27$ compared to that of columnar W and $WN_x$ film with $x = 0.20$ is contrary to Refs. [220,233] which found (for other amorphous and polycrystalline nitrides) the opposite.

The lower oxidation resistance of high-N content compositions is not likely to be due to thermodynamics: the formation enthalpies of stable $WN_x$ phases ($\Delta H_{\beta\text{-}W2N} = -22$ kJ/mol and $\Delta H_{\delta\text{-}WN} = -15$ kJ/mol) are, per W atom, negligible compared to that of $WO_3$ ($\Delta H_{WO2.7\text{-}3} = -743$ to -853 kJ/mol). However, it can be explained by kinetics. In particular by N diffusion outward of $WN_x$ films with $x \geq 0.27$ leaving behind a low-density W structure with many vacancies and pores, which is more prone to oxidize than pure W or $WN_x$ with $x \leq 0.20$. It should be noted that the sputtering technique used leads to a placement of high-N content atoms in metastable positions (grain boundaries, etc.) which can easily diffuse outward from the film at high $T$. Examples of this finding are shown in Figs. 11a,b where N diffuses outwards only from a depth of 0.13 μm below the surface of film with $x = 0.20$ and forms (according to a visual inspection) 0.55 μm thick $WO_3$ scale, while in film with $x = 1.5$ N diffuses outwards from a depth of 1.32 μm and forms 2.32 μm thick $WO_3$ scale. Note that the outward diffusion of N and inward diffusion of O may be further facilitated (i) the aforementioned formation of cracks in the $WO_3$ scale and (ii) the sparse polycrystalline structure of $WO_3$ scale.

# V. Conclusions

This Ph.D. thesis reports on the preparation of Al-Si and Ti-W alloy films, pure W metallic films and ceramic Al-Si-N and W-N films by magnetron sputter deposition and their characterization by different analytical techniques.

The main obtained results are summarized as follows:

A. The Al-Si films:

1. The Al-Si films with Si $\geq$ 95 at.% exhibit hardness $H$ up to 15 GPa, $H/E^*$ up to 0.12 and elastic recovery $W_e$ up to 74 %, due to their high Si content amorphous and/or nanocrystalline microstructure with crystallite size $D < 10$ nm.
2. The $H$ of 23.6 GPa of the Al-Si film with 25.2 at.% Si, reported by F. Xu, D. Gong (2018), was not achieved in our Al-Si films deposited in a broad range of (i) Si contents from 6 to 98 at.%, (ii) substrate temperatures $T_s$ from RT to 500 °C, and (iii) negative DC substrate biases $U_s$ from 50 to 350 V, and not even by addition of oxygen (20–66 at.% O) into our films.
3. he high cracking resistance was observed in the soft ($H \leq 8$ GPa) and ductile Al-Si films with Al > 33 at.% and low elasticity $H/E^* < 0.08$ and $W_e < 50$ % and high plasticity, or in the hard ($H \geq 9$ GPa) and brittle films with high Si > 70 at.% if their elasticity ($H/E^* > 0.08$ and $W_e > 50$ %) and the compressive macro-stress of the films is sufficiently high to prevent crack formation and propagation.
4. The Al-Si films with Si $\geq$ 95 at.% exhibit enhanced wear resistance, due to: (1) $H > 12$ GPa ($H_{100Cr6} \approx 10.5$ GPa), (2) nanocomposite nc-Si/a-Al ($D_{Si} \leq 4$ nm) or amorphous microstructure, and (3) $H/E^* > 0.1$ and $W_e > 60$ %.
5. The wear rate $k = 1–2\times10^{-6}$ mm$^3$/Nm and friction coefficient $\mu = 0.85$ of the films are moderately high, due to formation of abrasive hard and non-lubricating products of oxidation $AlO_x$ and $FeO_x$ in the wear track during dry sliding contact using the 100Cr6 ball.

B. The Al-Si-N films:

1. The Al-Si-N films with columnar microstructure were easily worn through even at their high $H = 30$ GPa, $H/E^* = 0.14$ and $W_e = 80$ % and compressive macro-stress, while the films with non-columnar microstructure with $D < 10$ nm or amorphous microstructure exhibit enhanced wear resistance.
2. The relative humidity RH at room temperature has a significant effect on the $k$ of the Al-Si-N films, where with increasing RH from 5 % (dry nitrogen) to 50 % (moist environment), $k$ increases from $0.1\times10^{-6}$ mm$^3$/Nm to $\sim1.0\times10^{-6}$ mm$^3$/Nm, and at RH = 82 %, the film was worn through, due to high formation of the abrasive $Al_2O_3$ in the wear track.

C. The plasma etching with enhanced ionization using a very low magnetron discharge of ~0.75 W/cm$^2$, at opened shutter, has been demonstrated to be an effective way to improve the adhesion of several micron thick W films, where no delamination was observed even at high compressive macro-stress up to 2.8 GPa of the films. The pure W films deposited at low ion energy bombardment $E_{bi}$ = 0.7 MJ/cm$^3$ and at high-density discharge with target power density in a pulse $W_{t\,pulse}$ ~100 W/cm$^2$ exhibit enhanced $H$ up to 21.5 GPa on a Si (100) substrate, and 24.3 GPa on a steel 15330 substrate, and enhanced $H/E^*$ up to 0.073 and $W_e$ up to 45 %. The enhanced mechanical properties of W films are due to grain boundary strengthening mechanism, where the $D$ decrease to ~14 nm. Decrease in $D$ is attributed to high-density discharge conditions.

D. The β-Ti(W) films:

1. The β-Ti(W) phase films with 12 at.% W were successfully prepared by magnetron sputtering, due to its two non-equilibrium processes: (a) the extremely fast heating of the growing film by energy $E$ of the ions and/or neutrals bombardment delivered into the film and (b) the extremely fast cooling of the created material down to the deposition temperature.
2. The thermal annealing of the homostructural β-($Ti_{88}W_{12}$) phase alloy film at temperature $T_a$ = 600 °C in Ar results in its partial conversion into the heterostructural nanocomposite film composed of high amount of β-($Ti_{88}W_{12}$) phase and low amount of α-($Ti_{88}W_{12}$) phase.
3. The β-($Ti_{88}W_{12}$) film is thermally stable to maximum temperature $T_{\beta\text{-phase max}} < T_a$ = 600 °C.
4. The heterostructural nanocomposite β-($Ti_{88}W_{12}$)/α-($Ti_{88}W_{12}$) film exhibits an enhanced $H$ up to 13 GPa, $H/E^*$ up to 0.08 and $W_e$ up to 55 %.
5. The β-Ti phase films represent a new class of "the heterostructural nanocomposite films".
6. The soft ($H \leq 5$ GPa) and ductile pure Ti and homostructural β-($Ti_{88}W_{12}$) alloy film exhibit no cracking even at $H/E^* < 0.10$ and $W_e < 60$ % and tensile macro-stress ($\sigma > 0$), while the hard ($H > 10$ GPa) heterostructural β-($Ti_{88}W_{12}$) alloy and pure W film, both with low $H/E^* < 0.10$ and $W_e < 60$ %, exhibit enhanced resistance to cracking when the compressive macro-stress is sufficiently high $|\sigma| > 1$ GPa.

E. The W and $WN_x$ films:

1. The $\mu$ and $k$ of the W and $WN_x$ films are strongly influenced by (i) the RH of ambient air, (ii) the surface oxidation and (iii) mechanical properties of their dominating phase.
2. The high RH causes low $\mu$ but high $k$, and vice versa, due to surface hydration and oxidation ($WN_x + H_2O \rightarrow WO_3 + NH_3$) of the $WN_x$ films at room temperature $T$.

3. The high $H$ = 22–34 GPa, high elasticity expressed by $H/E^* > 0.1$ and high $W_e \geq 62\%$ and dense microstructure of the $WN_x$ films with $x \geq 0.64$ lead to enhanced wear resistance ($k \sim 0.02 \times 10^{-6}$ mm$^3$/Nm) at $T \leq 150$ °C.
4. The oxidation of the W and $WN_x$ films at $T > 150$ °C lead to formation of the soft and lubricious $WO_3$ ($H_{WO3}$ = 4–5 GPa and $H/E^*_{WO3} = 0.05$) scale that: (i) on the one hand decreases $\mu$ to 0.5, while (ii) on the other hand causes high $k$ due to its brittleness ($H/E^*_{WO3} < 0.1$).
5. The W and $WN_x$ films with $x \leq 0.20$ exhibit higher oxidation resistance and thus higher wear resistance than the films with $x > 0.27$ at $T \geq 350$ °C, due to easy outward N diffusion from the films that further facilitate oxidation.

In order to create wear resistant films, these conditions should be achieved: (1) High hardness (≥25 GPa), because it is a prime metric to estimate reliability of the film lifetime, and should be sufficiently high, higher than that of the counterpart body and/or oxide debris. (2) High toughness (combination of extrinsic and intrinsic toughening). A good metric for toughness of film can be the $H/E$ ratio and elastic recovery $W_e$ – the higher the $H/E$ ratio (≥0.10), the higher the toughness of the film: $H/E \propto W_e \geq 60$ % holds. (3) Non-columnar, fine-grained, dense and void free or amorphous microstructure, to prevent crack formation and propagation along the grain boundaries.

# VI. Appendix

**Table 1** Mechanical properties (hardness *H* and effective Young's modulus $E^*$) of bulk materials measured at load $L$ = 0.1–1 N by micro-hardness tester using Vickers indenter. Where $h_{max}$ is a penetration depth of indenter into the material.

| Bulk material | surface | $H$ [GPa] | $E^*$ [GPa] | $H/E^*$ | $h_{max}$ [nm] | $L$ [N] | description |
|---|---|---|---|---|---|---|---|
| Al | unpolished | 0.52 ± 0.03 | 75 ± 4 | 0.007 | 6314 | 0.5 | sheet 3 mm thick |
| Si | polished | 13.0 ± 0.1 | 154 ± 2 | 0.084 | 611 | 0.1 | Si (100) wafer 0.625 mm |
| Ti | unpolished | 3.3 ± 0.4 | 131 ± 11 | 0.025 | 3750 | 1 | target sheet 5 mm thick |
| V | unpolished | 1.8 ± 0.2 | 130 ± 9 | 0.014 | 4923 | 1 | target sheet 6 mm thick |
| Cu | polished | 1.15 ± 0.01 | 128 ± 2 | 0.009 | 3773 | 0.4 | sheet 2 mm thick |
| Zn | unpolished | 0.52 ± 0.04 | 95 ± 20 | 0.005 | 8894 | 1 | sheet 4 mm thick |
| Zr | unpolished | 3.9 ± 0.4 | 117 ± 7 | 0.033 | 2172 | 0.4 | sheet 6 mm thick |
| Nb | unpolished | 1.5 ± 0.1 | 115 ± 6 | 0.013 | 5359 | 1 | target sheet 6 mm thick |
| Mo | unpolished | 3.7 ± 0.4 | 340 ± 30 | 0.011 | 3352 | 1 | sheet 1.5 mm thick |
| W | unpolished | 6.7 ± 0.4 | 410 ± 30 | 0.016 | 2533 | 1 | target sheet 6 mm thick |
| $Al_2O_3$ | polished | 21.9 ± 1.9 | 358 ± 14 | 0.061 | 1592 | 1 | sintered Ø6 mm ball |
| brass | unpolished | 1.9 ± 0.1 | 107 ± 5 | 0.018 | 3000 | 0.4 | sheet 9 mm thick |
| Soda-lime glass | polished | 7.45 ± 0.04 | 70.5 ± 0.3 | 0.105 | 1297 | 0.2 | 1 mm thick |
| Steel 15330 | polished | 2.68 ± 0.08 | 304 ± 15 | 0.009 | 3929 | 1 | Ø25 /2 mm coin |
| Steel 17240 (INOX) | polished | 4.5 ± 0.4 | 190 ± 18 | 0.024 | 3179 | 1 | Ø25 /5 mm coin |
| bearing steel 100Cr6 | polished | 10.3 ± 0.2 | 211 ± 5 | 0.049 | 1361 | 0.4 | Ø6 mm ball |
| $Ti_{95}B_5$ | unpolished | 4.0 ± 0.6 | 146 ± 15 | 0.027 | 3419 | 1 | target sheet 6 mm thick |
| Ti-6Al-4V (VT6) | unpolished | 5.7 ± 0.9 | 131 ± 12 | 0.044 | 1263 | 0.2 | target sheet 6 mm thick |
| WC | polished | 20.0 ± 0.3 | 530 ± 20 | 0.038 | 1549 | 1 | Ø6 mm ball |

# VII. References


[1] A. Matthews, S. Franklin, K. Holmberg, Tribological coatings: contact mechanisms and selection, J. Phys. D. Appl. Phys. 40 (2007) 5463–5475. https://doi.org/10.1088/0022-3727/40/18/S07.

[2] J.L. Grosseau-Poussard, P. Moine, M. Brendle, Shear strength measurements of parallel MoSx thin films, Thin Solid Films. 307 (1997) 163–168. https://doi.org/http://dx.doi.org/10.1016/S0040-6090(97)00205-8.

[3] K. Holmberg, H. Ronkainen, A. Matthews, Tribology of thin coatings, Ceram. Int. 26 (2000) 787–795. https://doi.org/10.1016/S0272-8842(00)00015-8.

[4] C. Donnet, A. Erdemir, Solid Lubricant Coatings: Recent Developments and Future Trends, Tribol. Lett. 17 (2004) 389–397. https://doi.org/10.1023/B:TRIL.0000044487.32514.1d.

[5] I. Hutchings, P. Shipway, Friction, in: Tribology, Second, Elsevier, 2017: pp. 37–77. https://doi.org/10.1016/B978-0-08-100910-9.00003-9.

[6] A.A. Voevodin, C. Muratore, S.M. Aouadi, Hard coatings with high temperature adaptive lubrication and contact thermal management: review, Surf. Coatings Technol. 257 (2014) 247–265. https://doi.org/10.1016/j.surfcoat.2014.04.046.

[7] T.L. Oberle, Wear of Metals, JOM. 3 (1951) 438–439. https://doi.org/10.1007/BF03397325.

[8] A. Leyland, A. Matthews, On the significance of the H/E ratio in wear control: A nanocomposite coating approach to optimised tribological behaviour, Wear. 246 (2000) 1–11. https://doi.org/10.1016/S0043-1648(00)00488-9.

[9] A. Leyland, A. Matthews, Design criteria for wear-resistant nanostructured and glassy-metal coatings, Surf. Coatings Technol. 177–178 (2004) 317–324. https://doi.org/10.1016/j.surfcoat.2003.09.011.

[10] M.G. Gee, N.M. Jennett, High resolution characterisation of tribochemical films on alumina, Wear. 193 (1996) 133–145. https://doi.org/10.1016/0043-1648(95)06612-8.

[11] S.M. Aouadi, H. Gao, A. Martini, T.W. Scharf, C. Muratore, Lubricious oxide coatings for extreme temperature applications: A review, Surf. Coatings Technol. 257 (2014) 266–277. https://doi.org/10.1016/j.surfcoat.2014.05.064.

[12] P.H. Mayrhofer, R. Rachbauer, D. Holec, F. Rovere, J.M. Schneider, Protective Transition Metal Nitride Coatings, Elsevier, 2014. https://doi.org/10.1016/B978-0-08-096532-1.00423-4.

[13] H. Holleck, V. Schier, Multilayer PVD coatings for wear protection, Surf. Coatings Technol. 76–77 (1995) 328–336. https://doi.org/10.1016/0257-8972(95)02555-3.

[14] S. Zhang, N. Ali, Nanocomposite Thin Films And Coatings, 2007.

[15] A. Berman, C. Drummond, J. Israelachvili, Amontons' law at the molecular level, Tribol. Lett. 4 (1998) 95–101. https://doi.org/10.1023/A:1019103205079.

[16] J. Krim, Surface science and the atomic-scale origins of friction: What once was old is new again, Surf. Sci. 500 (2002) 741–758. https://doi.org/10.1016/S0039-6028(01)01529-1.

[17] D. Berman, A. Erdemir, A. V. Sumant, Approaches for Achieving Superlubricity in Two-Dimensional Materials, ACS Nano. 12 (2018) 2122–2137. https://doi.org/10.1021/acsnano.7b09046.

[18] C. Muratore, A.A. Voevodin, Chameleon Coatings: Adaptive Surfaces to Reduce Friction and Wear in Extreme Environments, Annu. Rev. Mater. Res. 39 (2009) 297–324. https://doi.org/10.1146/annurev-matsci-082908-145259.

[19] K. Holmberg, H. Ronkainen, A. Laukkanen, K. Wallin, Friction and wear of coated surfaces - scales, modelling and simulation of tribomechanisms, Surf. Coatings Technol. 202 (2007) 1034–1049. https://doi.org/10.1016/j.surfcoat.2007.07.105.

[20] K. Holmberg, A. Matthews, COATINGS TRIBOLOGY: Properties, Mechanisms, Techniques and Applications in Surface Engineering, 2nd Editio, Elsevier, 2009. https://www.elsevier.com/books/coatings-tribology/holmberg/978-0-444-52750-9.

[21] C. Lu, Y.W. Mai, Y.G. Shen, Recent advances on understanding the origin of superhardness in nanocomposite coatings: A critical review, J. Mater. Sci. 41 (2006) 937–950. https://doi.org/10.1007/s10853-006-6577-9.

[22] J.A. Thornton, D.W. Hoffman, Stress-related effects in thin films, Thin Solid Films. 171 (1989) 5–31. https://doi.org/10.1016/0040-6090(89)90030-8.

[23] N. Hansen, Hall-petch relation and boundary strengthening, Scr. Mater. 51 (2004) 801–806.

https://doi.org/10.1016/j.scriptamat.2004.06.002.

[24] S. Vepřek, The search for novel, superhard materials, J. Vac. Sci. Technol. A Vacuum, Surfaces, Film. 17 (1999) 2401. https://doi.org/10.1116/1.581977.

[25] T.J. Rupert, J.C. Trenkle, C.A. Schuh, Enhanced solid solution effects on the strength of nanocrystalline alloys, Acta Mater. 59 (2011) 1619–1631. https://doi.org/10.1016/j.actamat.2010.11.026.

[26] L. Yang, C. Liu, M. Wen, X. Dai, Y. Zhang, X. Chen, K. Zhang, Small atoms as reinforced agent for both hardness and toughness of Group-VIB transition metal films, J. Alloys Compd. 735 (2018) 1105–1110. https://doi.org/10.1016/j.jallcom.2017.11.208.

[27] M. Stiefel, D. Kiener, P.H. Mayrhofer, J. Keckes, J. Patscheider, E. Stergar, R. Rachbauer, S. Massl, D. Holec, H. Leitner, Decomposition pathways in age hardening of Ti-Al-N films, J. Appl. Phys. 110 (2011) 023515. https://doi.org/10.1063/1.3610451.

[28] S.H. Jhi, S.G. Louie, M.L. Cohen, J. Ihm, Vacancy hardening and softening in transition metal carbides and nitrides, Phys. Rev. Lett. 86 (2001) 3348–3351. https://doi.org/10.1103/PhysRevLett.86.3348.

[29] C.S. Shin, D. Gall, N. Hellgren, J. Patscheider, I. Petrov, J.E. Greene, Vacancy hardening in single-crystal TiN x (001) layers, J. Appl. Phys. 93 (2003) 6025–6028. https://doi.org/10.1063/1.1568521.

[30] T. Lee, K. Ohmori, C.S. Shin, D.G. Cahill, I. Petrov, J.E. Greene, Elastic constants of single-crystal Ti Nx (001) (0.67≤x≤1.0) determined as a function of x by picosecond ultrasonic measurements, Phys. Rev. B - Condens. Matter Mater. Phys. 71 (2005) 1–6. https://doi.org/10.1103/PhysRevB.71.144106.

[31] S. Veprek, M.G.J. Veprek-Heijman, P. Karvankova, J. Prochazka, Different approaches to superhard coatings and nanocomposites, Thin Solid Films. 476 (2005) 1–29. https://doi.org/10.1016/j.tsf.2004.10.053.

[32] H.S. Kim, On the rule of mixtures for the hardness of particle reinforced composites, Mater. Sci. Eng. A. 289 (2000) 30–33. https://doi.org/10.1016/S0921-5093(00)00909-6.

[33] J. Musil, J. Vlček, Magnetron sputtering of hard nanocomposite coatings and their properties, Surf. Coatings Technol. 142–144 (2001) 557–566. https://doi.org/10.1016/S0257-8972(01)01139-2.

[34] S. Veprek, R.F. Zhang, M.G.J. Veprek-Heijman, S.H. Sheng, a. S. Argon, Superhard nanocomposites: Origin of hardness enhancement, properties and applications, Surf. Coatings Technol. 204 (2010) 1898–1906. https://doi.org/10.1016/j.surfcoat.2009.09.033.

[35] S. Veprek, M.G.J. Veprek-Heijman, Limits to the preparation of superhard nanocomposites: Impurities, deposition and annealing temperature, Thin Solid Films. 522 (2012) 274–282. https://doi.org/10.1016/j.tsf.2012.08.048.

[36] A. Pélisson-Schecker, H.J. Hug, J. Patscheider, Morphology, microstructure evolution and optical properties of Al–Si–N nanocomposite coatings, Surf. Coatings Technol. 257 (2014) 114–120. https://doi.org/10.1016/j.surfcoat.2014.08.053.

[37] S. Hogmark, S. Jacobson, M. Larsson, Design and evaluation of tribological coatings, Wear. 246 (2000) 20–33. https://doi.org/10.1016/S0043-1648(00)00505-6.

[38] K. Holmberg, Reliability aspects of tribology, Tribol. Int. 34 (2001) 801–808. https://doi.org/10.1016/S0301-679X(01)00078-0.

[39] D.G. Sangiovanni, V. Chirita, L. Hultman, Electronic mechanism for toughness enhancement in TixM1−xN (M=Mo and W), Phys. Rev. B. 81 (2010) 104107. https://doi.org/10.1103/PhysRevB.81.104107.

[40] S. Zhang, D. Sun, Y. Fu, H. Du, Toughness measurement of thin films: A critical review, Surf. Coatings Technol. 198 (2005) 74–84. https://doi.org/10.1016/j.surfcoat.2004.10.021.

[41] C. Wang, K. Shi, C. Gross, J.M. Pureza, M. de Mesquita Lacerda, Y.W. Chung, Toughness enhancement of nanostructured hard coatings: Design strategies and toughness measurement techniques, Surf. Coatings Technol. 257 (2014) 206–212. https://doi.org/10.1016/j.surfcoat.2014.08.018.

[42] R. Daniel, M. Meindlhumer, W. Baumegger, J. Zalesak, B. Sartory, M. Burghammer, C. Mitterer, J. Keckes, Grain boundary design of thin films: Using tilted brittle interfaces for multiple crack deflection toughening, Acta Mater. 122 (2017) 130–137. https://doi.org/10.1016/j.actamat.2016.09.027.

[43] S.F. Pugh, XCII. Relations between the elastic moduli and the plastic properties of polycrystalline pure metals, London, Edinburgh, Dublin Philos. Mag. J. Sci. 45 (1954) 823–843. https://doi.org/10.1080/14786440808520496.

[44] D.G. Pettifor, Theoretical predictions of structure and related properties of intermetallics, Mater. Sci. Technol. 8 (1992) 345–349. https://doi.org/10.1179/mst.1992.8.4.345.

[45] K. Balasubramanian, S. V. Khare, D. Gall, Valence electron concentration as an indicator for mechanical

properties in rocksalt structure nitrides, carbides and carbonitrides, Acta Mater. 152 (2018) 175–185. https://doi.org/10.1016/j.actamat.2018.04.033.

[46] P. Hohenberg, W. Kohn, Inhomogeneous Electron Gas, Phys. Rev. 136 (1964) B864–B871. https://doi.org/10.1103/PhysRev.136.B864.

[47] V. Petrman, J. Houska, Trends in formation energies and elastic moduli of ternary and quaternary transition metal nitrides, J. Mater. Sci. 48 (2013) 7642–7651. https://doi.org/10.1007/s10853-013-7582-4.

[48] H. Wang, H. Zeng, Q. Li, J. Shen, Superlattice supertoughness of TiN/MN (M = V, Nb, Ta, Mo, and W): First-principles study, Thin Solid Films. 607 (2016) 59–66. https://doi.org/10.1016/j.tsf.2016.03.061.

[49] H. Kindlund, D.G. Sangiovanni, I. Petrov, J.E. Greene, L. Hultman, A review of the intrinsic ductility and toughness of hard transition-metal nitride alloy thin films, Thin Solid Films. 688 (2019) 137479. https://doi.org/10.1016/j.tsf.2019.137479.

[50] D.G. Sangiovanni, L. Hultman, V. Chirita, Supertoughening in B1 transition metal nitride alloys by increased valence electron concentration, Acta Mater. 59 (2011) 2121–2134. https://doi.org/10.1016/j.actamat.2010.12.013.

[51] S.H. Jhi, J. Ihm, S.G. Loule, M.L. Cohen, Electronic mechanism of hardness enhancement in transition-metal carbonitrides, Nature. 399 (1999) 132–134. https://doi.org/10.1038/20148.

[52] T. Reeswinkel, D. Music, J.M. Schneider, Coulomb-potential-dependent decohesion of Magn??li phases, J. Phys. Condens. Matter. 22 (2010). https://doi.org/10.1088/0953-8984/22/29/292203.

[53] R.O. Ritchie, The conflicts between strength and toughness, Nat. Mater. 10 (2011) 817–822. https://doi.org/10.1038/nmat3115.

[54] S. Zhang, D. Sun, Y. Fu, H. Du, Toughening of hard nanostructural thin films: A critical review, Surf. Coatings Technol. 198 (2005) 2–8. https://doi.org/10.1016/j.surfcoat.2004.10.020.

[55] J. Musil, Flexible hard nanocomposite coatings, RSC Adv. 5 (2015) 60482–60495. https://doi.org/10.1039/C5RA09586G.

[56] J. Musil, Advanced Hard Coatings with Enhanced Toughness and Resistance to Cracking, CRC, Boca, CRC Press, 2015. https://doi.org/10.1201/b18729.

[57] P.J. Withers, Fracture mechanics by three-dimensional crack-tip synchrotron X-ray microscopy, Philos. Trans. R. Soc. A Math. Phys. Eng. Sci. 373 (2015). https://doi.org/10.1098/rsta.2013.0157.

[58] M. Stueber, H. Holleck, H. Leiste, K. Seemann, S. Ulrich, C. Ziebert, Concepts for the design of advanced nanoscale PVD multilayer protective thin films, J. Alloys Compd. 483 (2009) 321–333. https://doi.org/10.1016/j.jallcom.2008.08.133.

[59] A. Bendavid, P.. J. Martin, H. Takikawa, The properties of nanocomposite aluminium – silicon based thin films deposited by filtered arc deposition, Thin Solid Films. 421 (2002) 83–88.

[60] M. Parlinska-Wojtan, A. Pélisson-Schecker, H.J. Hug, B. Rutkowski, J. Patscheider, AlN/Si3N4 multilayers as an interface model systemfor Al1 − xSixN/Si3N4 nanocomposite thin film, Surf. Coat. Technol. 261 (2015) 418–425. https://doi.org/10.1016/j.surfcoat.2014.10.021.

[61] Z. Xia, L. Riester, W.A. Curtin, H. Li, B.W. Sheldon, J. Liang, B. Chang, J.M. Xu, Direct observation of toughening mechanisms in carbon nanotube ceramic matrix composites, Acta Mater. 52 (2004) 931–944. https://doi.org/10.1016/j.actamat.2003.10.050.

[62] C. Subramanian, K.N. Strafford, Review of multicomponent and multilayer coatings for tribological applications, Wear. 165 (1993) 85–95. https://doi.org/10.1016/0043-1648(93)90376-W.

[63] P. Panjan, M. Čekada, B. Navinšek, A new experimental method for studying the cracking behaviour of PVD multilayer coatings, Surf. Coatings Technol. 174–175 (2003) 55–62. https://doi.org/10.1016/S0257-8972(03)00618-2.

[64] R. Daniel, M. Meindlhumer, J. Zalesak, B. Sartory, A. Zeilinger, C. Mitterer, J. Keckes, Fracture toughness enhancement of brittle nanostructured materials by spatial heterogeneity: A micromechanical proof for CrN/Cr and TiN/SiOx multilayers, Mater. Des. 104 (2016) 227–234. https://doi.org/10.1016/j.matdes.2016.05.029.

[65] R. Hahn, M. Bartosik, R. Soler, C. Kirchlechner, G. Dehm, P.H. Mayrhofer, Superlattice effect for enhanced fracture toughness of hard coatings, Scr. Mater. 124 (2016) 67–70. https://doi.org/10.1016/j.scriptamat.2016.06.030.

[66] D.B. Marshall, A.G. Evans, M. Drory, Transformation Toughening in Ceramics., Fract. Mech. Ceram. 6 (1983) 289–307.

[67] Z. Chen, B. Cotterell, W. Wang, The fracture of brittle thin films on compliant substrates in flexible displays, Eng. Fract. Mech. 69 (2002) 597–603. https://doi.org/10.1016/S0013-7944(01)00104-7.

[68] Y. Leterrier, L. Médico, F. Demarco, J.-A.E. Månson, U. Betz, M.F. Escolà, M. Kharrazi Olsson, F. Atamny, Mechanical integrity of transparent conductive oxide films for flexible polymer-based displays, Thin Solid Films. 460 (2004) 156–166. https://doi.org/10.1016/j.tsf.2004.01.052.

[69] M. Mikula, M. Truchlý, D.G. Sangiovanni, D. Plašienka, T. Roch, M. Gregor, P. Ďurina, M. Janík, P. Kúš, Experimental and computational studies on toughness enhancement in Ti-Al-Ta-N quaternaries, J. Vac. Sci. Technol. A Vacuum, Surfaces, Film. 35 (2017) 060602. https://doi.org/10.1116/1.4997431.

[70] B. Grossmann, M. Tkadletz, N. Schalk, C. Czettl, M. Pohler, C. Mitterer, High-temperature tribology and oxidation of Ti1−x−yAlxTayN hard coatings, Surf. Coatings Technol. 342 (2018) 190–197. https://doi.org/10.1016/j.surfcoat.2018.02.062.

[71] J. Musil, M. Jirout, Toughness of hard nanostructured ceramic thin films, Surf. Coatings Technol. 201 (2007) 5148–5152. https://doi.org/10.1016/j.surfcoat.2006.07.020.

[72] J. Musil, J. Blažek, K. Fajfrlík, R. Čerstvý, Flexible antibacterial Al–Cu–N films, Surf. Coatings Technol. 264 (2015) 114–120. https://doi.org/10.1016/j.surfcoat.2015.01.006.

[73] J. Musil, S. Zenkin, Š. Kos, R. Čerstvý, S. Haviar, Flexible hydrophobic ZrN nitride films, Vacuum. (2016). https://doi.org/10.1016/j.vacuum.2016.05.020.

[74] Č.R. Musil, J., Jílek R., Flexible Ti-Ni-N Thin Films Prepared by Magnetron Sputtering, J. Mater. Sci. Eng. 4 (2014) 1–7.

[75] J. Musil, M. Zítek, K. Fajfrlík, R. Čerstvý, Flexible antibacterial Zr-Cu-N thin films resistant to cracking, J. Vac. Sci. Technol. A Vacuum, Surfaces, Film. 34 (2016) 021508. https://doi.org/10.1116/1.4937727.

[76] J. Musil, J. Sklenka, R. Čerstvý, T. Suzuki, T. Mori, M. Takahashi, The effect of addition of Al in ZrO 2 thin film on its resistance to cracking, Surf. Coatings Technol. 207 (2012) 355–360. https://doi.org/10.1016/j.surfcoat.2012.07.017.

[77] J. Musil, S. Zenkin, R. Čerstvý, S. Haviar, Z. Čiperová, (Zr,Ti,O) alloy films with enhanced hardness and resistance to cracking prepared by magnetron sputtering, Surf. Coatings Technol. 322 (2017) 86–91. https://doi.org/10.1016/j.surfcoat.2017.05.006.

[78] J. Musil, J. Sklenka, J. Prochazka, Protective over-layer coating preventing cracking of thin films deposited on flexible substrates, Surf. Coatings Technol. 240 (2014) 275–280. https://doi.org/10.1016/j.surfcoat.2013.12.041.

[79] M. Jaroš, J. Musil, S. Haviar, Interrelationships among macrostress, microstructure and mechanical behavior of sputtered hard Ti(Al,V)N films, Mater. Lett. 235 (2019) 92–96. https://doi.org/10.1016/j.matlet.2018.09.173.

[80] A. Anders, A structure zone diagram including plasma-based deposition and ion etching, Thin Solid Films. 518 (2010) 4087–4090. https://doi.org/10.1016/j.tsf.2009.10.145.

[81] J. Musil, G. Remnev, V. Legostaev, V. Uglov, A. Lebedynskiy, A. Lauk, J. Procházka, S. Haviar, E. Smolyanskiy, Flexible hard Al-Si-N films for high temperature operation, Surf. Coatings Technol. 307 (2016) 1112–1118. https://doi.org/10.1016/j.surfcoat.2016.05.054.

[82] S. Vepřek, S. Reiprich, A concept for the design of novel superhard coatings, Thin Solid Films. 268 (1995) 64–71. https://doi.org/10.1016/0040-6090(95)06695-0.

[83] A. Pélisson, M. Parlinska-Wojtan, H.J. Hug, J. Patscheider, Microstructure and mechanical properties of Al-Si-N transparent hard coatings deposited by magnetron sputtering, Surf. Coatings Technol. 202 (2007) 884–889. https://doi.org/10.1016/j.surfcoat.2007.05.094.

[84] J. Musil, D. Javdošňák, R. Čerstvý, S. Haviar, G. Remnev, V. Uglov, Effect of energy on the formation of flexible hard Al-Si-N films prepared by magnetron sputtering, Vacuum. 133 (2016) 43–45. https://doi.org/10.1016/j.vacuum.2016.08.014.

[85] J. Musil, M. Jaroš, R. Čerstvý, S. Haviar, Evolution of microstructure and macrostress in sputtered hard Ti(Al,V)N films with increasing energy delivered during their growth by bombarding ions, J. Vac. Sci. Technol. A Vacuum, Surfaces, Film. 35 (2017) 020601. https://doi.org/10.1116/1.4967935.

[86] M. Jaroš, J. Musil, R. Čerstvý, S. Haviar, Effect of energy on macrostress in Ti(Al,V)N films prepared by magnetron sputtering, Vacuum. 158 (2018) 52–59. https://doi.org/10.1016/j.vacuum.2018.09.038.

[87] J.A. Thornton, Influence of apparatus geometry and deposition conditions on the structure and topography of thick sputtered coatings, J. Vac. Sci. Technol. 11 (1974) 666–670. https://doi.org/10.1116/1.1312732.

[88] H. Poláková, J. Musil, J. Vlček, J. Allaart, C. Mitterer, Structure-hardness relations in sputtered Ti-Al-V-N films, Thin Solid Films. 444 (2003) 189–198. https://doi.org/10.1016/S0040-6090(03)01096-4.

[89] H. Windischmann, Critical Reviews in Solid State and Materials Sciences Intrinsic stress in sputter-deposited thin films Intrinsic Stress in Sputter-Deposited Thin Films, Crit. Rev. Solid State Mater. Sci.

Criticul Rev. Solid State Und Mater. Sci. 176 (1992) 37–41. https://doi.org/10.1080/10408439208244586.

[90] K. Meyer, I.K. Schuller, C.M. Falco, Thermalization of sputtered atoms, J. Appl. Phys. 52 (1981) 5803. https://doi.org/10.1063/1.329473.

[91] J. Lu, C.G. Lee, Numerical estimates for energy of sputtered target atoms and reflected Ar neutrals in sputter processes, Vacuum. 86 (2012) 1134–1140. https://doi.org/10.1016/j.vacuum.2011.10.018.

[92] J. Musil, M. Jaroš, Plasma and floating potentials in magnetron discharges, J. Vac. Sci. Technol. A Vacuum, Surfaces, Film. 35 (2017) 060605. https://doi.org/10.1116/1.4992054.

[93] H. Ye, An overview of the development of Al-Si-alloy based material for engine applications, J. Mater. Eng. Perform. 12 (2003) 288–297. https://doi.org/10.1361/105994903770343132.

[94] A. Wang, L. Zhou, Y. Kong, Y. Du, Z.K. Liu, S.L. Shang, Y. Ouyang, J. Wang, L. Zhang, J. Wang, First-principles study of binary special quasirandom structures for the Al-Cu, Al-Si, Cu-Si, and Mg-Si systems, Calphad Comput. Coupling Phase Diagrams Thermochem. 33 (2009) 769–773. https://doi.org/10.1016/j.calphad.2009.10.007.

[95] P.N.H. Nakashima, A.E. Smith, J. Etheridge, B.C. Muddle, The Bonding Electron Density in Aluminum, Science (80-. ). 331 (2011) 1583–1586. https://doi.org/10.1126/science.1198543.

[96] J. Il Jang, M.J. Lance, S. Wen, T.Y. Tsui, G.M. Pharr, Indentation-induced phase transformations in silicon: Influences of load, rate and indenter angle on the transformation behavior, Acta Mater. 53 (2005) 1759–1770. https://doi.org/10.1016/j.actamat.2004.12.025.

[97] J.M. Zuo, P. Blaha, K. Schwarz, The theoretical charge density of silicon: experimental testing of exchange and correlation potentials, J. Phys. Condens. Matter. 9 (1997) 7541–7561. https://doi.org/10.1088/0953-8984/9/36/004.

[98] J.L. Murray, A.J. McAlister, The Al-Si (Aluminum-Silicon) system, Bull. Alloy Phase Diagrams. 5 (1984) 74–84. https://doi.org/10.1007/BF02868729.

[99] A. Bendijk, R. Delhez, L. Katgerman, T.H. De Keijser, E.J. Mittemeijer, N.M. Van Der Pers, Characterization of Al-Si-alloys rapidly quenched from the melt, J. Mater. Sci. 15 (1980) 2803–2810. https://doi.org/10.1007/BF00550549.

[100] K.D. Leedy, J.M. Rigsbee, Microstructure of radio frequency sputtered Ag 1− x Si x alloys , J. Vac. Sci. Technol. A Vacuum, Surfaces, Film. 14 (2002) 2202–2206. https://doi.org/10.1116/1.580047.

[101] J. Musil, Š. Kos, S. Zenkin, Z. Čiperová, D. Javdošňák, R. Čerstvý, β- (Me 1 , Me 2 ) and MeNx films deposited by magnetron sputtering: Novel heterostructural alloy and compound films, Surf. Coatings Technol. 337 (2018) 75–81. https://doi.org/10.1016/j.surfcoat.2017.12.057.

[102] K. Nakata, M. Ushio, Wear resistance of plasma sprayed Al-Si binary alloy coatings on A6063 Al alloy substrate, Surf. Coatings Technol. 142–144 (2001) 277–283. https://doi.org/10.1016/S0257-8972(01)01088-X.

[103] W.Y. Li, C. Zhang, X.P. Guo, G. Zhang, H.L. Liao, C. Coddet, Deposition characteristics of Al-12Si alloy coating fabricated by cold spraying with relatively large powder particles, Appl. Surf. Sci. 253 (2007) 7124–7130. https://doi.org/10.1016/j.apsusc.2007.02.142.

[104] W. f. Wang, M. c. Wang, F. j. Sun, Y. g. Zheng, J. m. Jiao, Microstructure and cavitation erosion characteristics of Al-Si alloy coating prepared by electrospark deposition, Surf. Coatings Technol. 202 (2008) 5116–5121. https://doi.org/10.1016/j.surfcoat.2008.05.013.

[105] G.P. Dinda, A.K. Dasgupta, J. Mazumder, Evolution of microstructure in laser deposited Al-11.28%Si alloy, Surf. Coatings Technol. 206 (2012) 2152–2160. https://doi.org/10.1016/j.surfcoat.2011.09.051.

[106] N. Kang, P. Coddet, H. Liao, T. Baur, C. Coddet, Wear behavior and microstructure of hypereutectic Al-Si alloys prepared by selective laser melting, Appl. Surf. Sci. 378 (2016) 142–149. https://doi.org/10.1016/j.apsusc.2016.03.221.

[107] N. Kang, P. Coddet, C. Chen, Y. Wang, H. Liao, C. Coddet, Microstructure and wear behavior of in-situ hypereutectic Al-high Si alloys produced by selective laser melting, Mater. Des. 99 (2016) 120–126. https://doi.org/10.1016/j.matdes.2016.03.053.

[108] F. Xu, D. Gong, Improved the elevated temperature mechanical properties of Al-Si alloy deposited with Al-Si coating by magnetron sputtering, Vacuum. 150 (2018) 1–7. https://doi.org/10.1016/j.vacuum.2018.01.013.

[109] C.-L. Chen, a. Richter, R.C. Thomson, Mechanical properties of intermetallic phases in multi-component Al–Si alloys using nanoindentation, Intermetallics. 17 (2009) 634–641. https://doi.org/10.1016/j.intermet.2009.02.003.

[110] C.L. Chang, C.S. Huang, Effect of bias voltage on microstructure, mechanical and wear properties of Al-

Si-N coatings deposited by cathodic arc evaporation, Thin Solid Films. 519 (2011) 4923–4927. https://doi.org/10.1016/j.tsf.2011.01.054.

[111] J. Musil, M. Šašek, P. Zeman, R. Čerstvý, D. Heřman, J.G. Han, V. Šatava, Properties of magnetron sputtered Al-Si-N thin films with a low and high Si content, Surf. Coatings Technol. 202 (2008) 3485–3493. https://doi.org/10.1016/j.surfcoat.2007.12.024.

[112] H. Liu, W. Tang, D. Hui, L. Hei, F. Lu, Characterization of (Al, Si)N films deposited by balanced magnetron sputtering, Thin Solid Films. 517 (2009) 5988–5993. https://doi.org/10.1016/j.tsf.2009.03.173.

[113] E. Lewin, D. Loch, A. Montagne, A.P. Ehiasarian, J. Patscheider, Comparison of Al-Si-N nanocomposite coatings deposited by HIPIMS and DC magnetron sputtering, Surf. Coatings Technol. 232 (2013) 680–689. https://doi.org/10.1016/j.surfcoat.2013.06.076.

[114] J.C. Ding, Q.M. Wang, Z.R. Liu, S. Jeong, T.F. Zhang, K.H. Kim, Influence of bias voltage on the microstructure, mechanical and corrosion properties of AlSiN films deposited by HiPIMS technique, J. Alloys Compd. 772 (2019) 112–121. https://doi.org/10.1016/j.jallcom.2018.09.063.

[115] N. Petkov, T. Bakalova, T. Cholakova, H. Bahchedzhiev, P. Louda, P. Ryšánek, M. Kormunda, P. Čapková, P. Kejzlar, Study of surface morphology, structure, mechanical and tribological properties of an AlSiN coating obtained by the cathodic arc deposition method, Superlattices Microstruct. 109 (2017) 402–413. https://doi.org/10.1016/j.spmi.2017.05.022.

[116] I. Bozhko, E. Rybalko, A. Pershukova, M. Fedorischeva, Y. Khristenko, V. Sergeev, Microstructure and properties of nanocomposite Al-Si-N system coatings produced by magnetron sputtering, 030014 (2016) 030014. https://doi.org/10.1063/1.4964552.

[117] I.A. Bozhko, E. V. Rybalko, M. V. Fedorischeva, V.L. Solntsev, A.G. Cherniavsky, A.Y. Kaleri, S.G. Psakhie, V.P. Sergeev, Protection from high-velocity impact particles for quartz glass by coatings on the basis of Al-Si-N, (2016) 020018. https://doi.org/10.1063/1.4966311.

[118] Soni, S. Kumari, S.K. Sharma, S.K. Mishra, Effect of Deposition Pressure, Nitrogen Content and Substrate Temperature on Optical and Mechanical Behavior of Nanocomposite Al-Si-N Hard Coatings for Solar Thermal Applications, J. Mater. Eng. Perform. (2018) 4–11. https://doi.org/10.1007/s11665-018-3730-y.

[119] a. Mazel, P. Marti, F. Henry, B. Armas, R. Bonnet, M. Loubradou, Nanostructure and local chemical composition of AlNSi3N4 layers grown by LPCVD, Thin Solid Films. 304 (1997) 256–266. https://doi.org/10.1016/S0040-6090(97)00221-6.

[120] S. Zenkin, F. Konusov, A. Lauk, D. Zelentsov, S. Demchenko, Structure, Mechanical and Optical Properties of Silicon-Rich Al–Si–N Films Prepared by High Power Impulse Magnetron Sputtering, Coatings. 9 (2019) 53. https://doi.org/10.3390/coatings9010053.

[121] E. Lassner, W.-D. Schubert, Tungsten: Properties, Chemistry, Technology of the Element, Alloys and Chemical Compounds., Springer, Boston, MA, 1999. https://doi.org/10.1007/978-1-4615-4907-9.

[122] I.L. Velicu, V. Tiron, C. Porosnicu, I. Burducea, N. Lupu, G. Stoian, G. Popa, D. Munteanu, Enhanced properties of tungsten thin films deposited with a novel HiPIMS approach, Appl. Surf. Sci. 424 (2017) 397–406. https://doi.org/10.1016/j.apsusc.2017.01.067.

[123] T. Polcar, N.M.G. Parreira, A. Cavaleiro, Tribological characterization of tungsten nitride coatings deposited by reactive magnetron sputtering, Wear. 262 (2007) 655–665. https://doi.org/10.1016/j.wear.2006.07.010.

[124] T. Polcar, N.M.G. Parreira, A. Cavaleiro, Structural and tribological characterization of tungsten nitride coatings at elevated temperature, Wear. 265 (2008) 319–326. https://doi.org/10.1016/j.wear.2007.10.011.

[125] W.H. Kao, Optimized a-C:Wx% coatings with enhanced tribological properties and improved micro-drilling performance, Surf. Coatings Technol. 201 (2007) 7392–7400. https://doi.org/10.1016/j.surfcoat.2007.02.007.

[126] M.D. Abad, M.A. Muñoz-Márquez, S. El Mrabet, A. Justo, J.C. Sánchez-López, Tailored synthesis of nanostructured WC/a-C coatings by dual magnetron sputtering, Surf. Coatings Technol. 204 (2010) 3490–3500. https://doi.org/10.1016/j.surfcoat.2010.04.019.

[127] J. Pu, D. He, L. Wang, Effects of WC phase contents on the microstructure, mechanical properties and tribological behaviors of WC/a-C superlattice coatings, Appl. Surf. Sci. 357 (2015) 2039–2047. https://doi.org/10.1016/j.apsusc.2015.09.181.

[128] G.Y. Du, D.C. Ba, Z. Tan, K. Liu, Tribological behavior of radio-frequency sputtering WS2 thin films with vacuum annealing, Thin Solid Films. 520 (2011) 849–852. https://doi.org/10.1016/j.tsf.2011.04.195.

[129] A.A. Voevodin, J.S. Zabinski, Supertough wear-resistant coatings with “chameleon” surface adaptation, Thin Solid Films. 370 (2000) 223–231. https://doi.org/10.1016/S0040-6090(00)00917-2.

[130] J.H. Wu, D.A. Rigney, M.L. Falk, J.H. Sanders, A.A. Voevodin, J.S. Zabinski, Tribological behavior of WC/DLC/WS2nanocomposite coatings, Surf. Coatings Technol. 188–189 (2004) 605–611. https://doi.org/10.1016/j.surfcoat.2004.07.079.

[131] T. Polcar, M. Evaristo, A. Cavaleiro, The tribological behavior of W-S-C films in pin-on-disk testing at elevated temperature, Vacuum. 81 (2007) 1439–1442. https://doi.org/10.1016/j.vacuum.2007.04.010.

[132] T. Polcar, A. Cavaleiro, Self-adaptive low friction coatings based on transition metal dichalcogenides, Thin Solid Films. 519 (2011) 4037–4044. https://doi.org/10.1016/j.tsf.2011.01.180.

[133] F. Gustavsson, S. Jacobson, A. Cavaleiro, T. Polcar, Ultra-low friction W-S-N solid lubricant coating, Surf. Coatings Technol. 232 (2013) 541–548. https://doi.org/10.1016/j.surfcoat.2013.06.026.

[134] P. Mutafov, M. Evaristo, A. Cavaleiro, T. Polcar, Structure, mechanical and tribological properties of self-lubricant W-S-N coatings, Surf. Coatings Technol. 261 (2015) 7–14. https://doi.org/10.1016/j.surfcoat.2014.11.074.

[135] L. Yu, H. Zhao, J. Xu, Mechanical, tribological and corrosion performance of WBN composite films deposited by reactive magnetron sputtering, Appl. Surf. Sci. 315 (2014) 380–386. https://doi.org/10.1016/j.apsusc.2014.07.170.

[136] R. Ospina, D. Escobar, E. Restrepo-Parra, P.J. Arango, J.F. Jurado, Mechanical and tribological behavior of W/WCN bilayers grown by pulsed vacuum arc discharge, Tribol. Int. 62 (2013) 124–129. https://doi.org/10.1016/j.triboint.2013.01.014.

[137] H. Zhao, Z. Ni, F. Ye, Effect of carbon content on structure and properties of WCN coatings prepared by RF magnetron sputtering, Surf. Coatings Technol. 287 (2016) 129–137. https://doi.org/10.1016/j.surfcoat.2016.01.003.

[138] C. Strondl, N.M. Carvalho, J.T.M. De Hosson, T.G. Krug, Influence of energetic ion bombardment on W-C:H coatings deposited with W and WC targets, Surf. Coatings Technol. 200 (2005) 1142–1146. https://doi.org/10.1016/j.surfcoat.2005.02.182.

[139] A.A. Voevodin, J.P. O'Neill, S. V. Prasad, J.S. Zabinski, Nanocrystalline WC and WC/a-C composite coatings produced from intersected plasma fluxes at low deposition temperatures, J. Vac. Sci. Technol. A Vacuum, Surfaces, Film. 17 (1999) 986–992. https://doi.org/10.1116/1.581674.

[140] A.A. Gharam, M.J. Lukitsch, M.P. Balogh, N. Irish, A.T. Alpas, High temperature tribological behavior of W-DLC against aluminum, Surf. Coatings Technol. 206 (2011) 1905–1912. https://doi.org/10.1016/j.surfcoat.2011.08.002.

[141] A. Banerji, S. Bhowmick, A.T. Alpas, High temperature tribological behavior of W containing diamond-like carbon (DLC) coating against titanium alloys, Surf. Coatings Technol. 241 (2014) 93–104. https://doi.org/10.1016/j.surfcoat.2013.10.075.

[142] R. Zhang, Z. Huo, X. Jiao, H. Zhong, Y. Shi, Deposition of Tungsten Thin Films on Flexible Polymer Substrates by Direct-Current Magnetron Sputtering, J. Electron. Mater. 44 (2015) 4557–4562. https://doi.org/10.1007/s11664-015-3936-9.

[143] R. Matera, G. Federici, Design requirements for plasma facing materials in ITER, J. Nucl. Mater. 233–237 (1996) 17–25. https://doi.org/10.1016/S0022-3115(96)00317-0.

[144] T.J. Renk, P.P. Provencio, T.J. Tanaka, J.P. Blanchard, C.J. Martin, T.R. Knowles, Survivability of First-Wall Materials in Fusion Devices: An Experimental Study of Material Exposure to Pulsed Energetic Ions, Fusion Sci. Technol. 61 (2012) 57–80. https://doi.org/10.13182/FST12-A13339.

[145] S. Eroglu, H. Ekren, T. Baykara, Surface hardening of tungsten heavy alloys, Scr. Mater. 38 (1997) 131–136. https://doi.org/10.1016/S1359-6462(97)00412-0.

[146] H.L. Sun, Z.X. Song, D.G. Guo, F. Ma, K.W. Xu, Microstructure and Mechanical Properties of Nanocrystalline Tungsten Thin Films, J. Mater. Sci. Technol. 26 (2010) 87–92. https://doi.org/10.1016/S1005-0302(10)60014-X.

[147] N. Gordillo, M. Panizo-Laiz, E. Tejado, I. Fernandez-Martinez, A. Rivera, J.Y. Pastor, C.G. De Castro, J. Del Rio, J.M. Perlado, R. Gonzalez-Arrabal, Morphological and microstructural characterization of nanostructured pure α-phase W coatings on a wide thickness range, Appl. Surf. Sci. 316 (2014) 1–8. https://doi.org/10.1016/j.apsusc.2014.07.061.

[148] F.T.N. Vüllers, R. Spolenak, Alpha- vs. beta-W nanocrystalline thin films: A comprehensive study of sputter parameters and resulting materials' properties, Thin Solid Films. 577 (2015) 26–34. https://doi.org/10.1016/j.tsf.2015.01.030.

[149] I.A. Weerasekera, D. V Baxter, Structure and stability of sputter deposited thin films, 64 (1994) 3231–3233.

[150] S.M. Rossnagel, I.C. Noyan, C. Cabral, Phase transformation of thin sputter-deposited tungsten films at room temperature, J. Vac. Sci. Technol. B Microelectron. Nanom. Struct. 20 (2002) 2047. https://doi.org/10.1116/1.1506905.

[151] G.S. Chen, L.C. Yang, H.S. Tian, C.S. Hsu, Evaluating substrate bias on the phase-forming behavior of tungsten thin films deposited by diode and ionized magnetron sputtering, Thin Solid Films. 484 (2005) 83–89. https://doi.org/10.1016/j.tsf.2005.02.032.

[152] J. Liu, K. Barmak, Topologically close-packed phases: Deposition and formation mechanism of metastable β-W in thin films, Acta Mater. 104 (2016) 223–227. https://doi.org/10.1016/j.actamat.2015.11.049.

[153] C.S. Chang, T.B. Wu, C.K. Huang, W.C. Shih, L.L. Chao, Thermal stability and oxidation resistance of W, TiW, W(N) and TiW(N) thin films deposited on Si, Japanese J. Appl. Physics, Part 1 Regul. Pap. Short Notes Rev. Pap. 39 (2000) 6413–6421.

[154] R.R. Boyer, An overview on the use of titanium in the aerospace industry, Mater. Sci. Eng. A. 213 (1996) 103–114. https://doi.org/10.1016/0921-5093(96)10233-1.

[155] I. Weiss, S.L. Semiatin, Thermomechanical processing of beta titanium alloys—an overview, Mater. Sci. Eng. A. 243 (1998) 46–65. https://doi.org/10.1016/S0921-5093(97)00783-1.

[156] P.J. Bania, Beta titanium alloys and their role in the titanium industry, Jom. 46 (1994) 16–19. https://doi.org/10.1007/BF03220742.

[157] J.L. Murray, The Ti-W (Titanium-Tungsten) system, Bull. Alloy Phase Diagrams. 2 (1981) 192–196. https://doi.org/10.1007/BF02881477.

[158] S.N. Saud, S. Raheleh Hosseinian, H.R. Bakhsheshi-Rad, F. Yaghoubidoust, N. Iqbal, E. Hamzah, C.H.R. Ooi, Corrosion and bioactivity performance of graphene oxide coating on Ti-Nb shape memory alloys in simulated body fluid, Mater. Sci. Eng. C. 68 (2016) 687–694. https://doi.org/10.1016/j.msec.2016.06.048.

[159] D. Photiou, N.T. Panagiotopoulos, L. Koutsokeras, G.A. Evangelakis, G. Constantinides, Microstructure and nanomechanical properties of magnetron sputtered Ti − Nb films, Surf. Coatings Technol. 302 (2016) 310–319. https://doi.org/10.1016/j.surfcoat.2016.06.014.

[160] S. Achache, S. Lamri, M. Arab Pour Yazdi, A. Billard, M. François, F. Sanchette, Ni-free superelastic binary Ti-Nb coatings obtained by DC magnetron co-sputtering, Surf. Coatings Technol. 275 (2015) 283–288. https://doi.org/10.1016/j.surfcoat.2015.05.005.

[161] E.D. Gonzalez, C.R.M. Afonso, P.A.P. Nascente, Influence of Nb content on the structure, morphology, nanostructure, and properties of titanium-niobium magnetron sputter deposited coatings for biomedical applications, Surf. Coatings Technol. 326 (2017) 424–428. https://doi.org/10.1016/j.surfcoat.2017.03.015.

[162] E.D. Gonzalez, T.C. Niemeyer, C.R.M. Afonso, P.A.P. Nascente, Ti-Nb thin films deposited by magnetron sputtering on stainless steel, J. Vac. Sci. Technol. A Vacuum, Surfaces, Film. 34 (2016) 021511. https://doi.org/10.1116/1.4940753.

[163] Y. Motemani, P.J.S. Buenconsejo, C. Craciunescu, A. Ludwig, High-Temperature Shape Memory Effect in Ti-Ta Thin Films Sputter Deposited at Room Temperature, Adv. Mater. Interfaces. 1 (2014) 5–9. https://doi.org/10.1002/admi.201400019.

[164] P.M. Kadletz, Y. Motemani, J. Iannotta, S. Salomon, C. Khare, L. Grossmann, H.J. Maier, A. Ludwig, W.W. Schmahl, Crystallographic Structure Analysis of a Ti-Ta Thin Film Materials Library Fabricated by Combinatorial Magnetron Sputtering, ACS Comb. Sci. 20 (2018) 137–150. https://doi.org/10.1021/acscombsci.7b00135.

[165] F. Zhang, C. Li, M. Yan, J. He, Y. Yang, F. Yin, Microstructure and nanomechanical properties of co-deposited Ti-Cr films prepared by magnetron sputtering, Surf. Coatings Technol. 325 (2017) 636–642. https://doi.org/10.1016/j.surfcoat.2017.07.005.

[166] J. Musil, A.J. Bell, J. Vlček, T. Hurkmans, Formation of high temperature phases in sputter deposited Ti-based films below 100 °C, J. Vac. Sci. Technol. A Vacuum, Surfaces, Film. 14 (1996) 2247–2250. https://doi.org/10.1116/1.580055.

[167] W.F. Ho, T.Y. Chiang, S.C. Wu, H.C. Hsu, Mechanical properties and deformation behavior of cast binary Ti-Cr alloys, J. Alloys Compd. 468 (2009) 533–538. https://doi.org/10.1016/j.jallcom.2008.01.046.

[168] H.C. Hsu, S.C. Wu, T.Y. Chiang, W.F. Ho, Structure and grindability of dental Ti-Cr alloys, J. Alloys Compd. 476 (2009) 817–825. https://doi.org/10.1016/j.jallcom.2008.09.116.

[169] M. Callisti, F.D. Tichelaar, T. Polcar, In situ TEM observations on the structural evolution of a nanocrystalline W-Ti alloy at elevated temperatures, J. Alloys Compd. 749 (2018) 1000–1008. https://doi.org/10.1016/j.jallcom.2018.03.335.

[170] T. Saito, Multifunctional Alloys Obtained via a Dislocation-Free Plastic Deformation Mechanism, Science

(80-. ). 300 (2003) 464–467. https://doi.org/10.1126/science.1081957.

[171] E. Frutos, M. Karlík, J.A. Jiménez, H. Langhansová, J. Lieskovská, T. Polcar, Development of new β/α″-Ti-Nb-Zr biocompatible coating with low Young's modulus and high toughness for medical applications, Mater. Des. 142 (2018) 44–55. https://doi.org/10.1016/j.matdes.2018.01.014.

[172] S. Achache, S. Lamri, A. Alhussein, A. Billard, M. François, F. Sanchette, Gum Metal thin films obtained by magnetron sputtering of a Ti-Nb-Zr-Ta target, Mater. Sci. Eng. A. 673 (2016) 492–502. https://doi.org/10.1016/j.msea.2016.07.096.

[173] S. Achache, A. Alhussein, S. Lamri, M. Francois, F. Sanchette, C. Pulgarin, J. Kiwi, S. Rtimi, Sputtered Gum metal thin films showing bacterial inactivation and biocompatibility, Colloids Surfaces B Biointerfaces. 146 (2016) 687–691. https://doi.org/10.1016/j.colsurfb.2016.07.007.

[174] J. Castanho, A. Cavaleiro, Study of tungsten sputtered films with low nitrogen content, Vacuum. 45 (1994) 1051–1053. https://doi.org/https://doi.org/10.1016/0042-207X(94)90020-5.

[175] M.T. Vieira, A.S. Ramos, Influence of ductile interlayers on the mechanical performance of tungsten nitride coatings, J. Mater. Process. Technol. 92–93 (1999) 156–161. https://doi.org/10.1016/S0924-0136(99)00235-6.

[176] N.M.G. Parreira, N.J.M. Carvalho, F. Vaz, A. Cavaleiro, Mechanical evaluation of unbiased W-O-N coatings deposited by d.c. reactive magnetron sputtering, Surf. Coatings Technol. 200 (2006) 6511–6516. https://doi.org/10.1016/j.surfcoat.2005.11.020.

[177] T. Polcar, A. Cavaleiro, Structure, mechanical properties and tribology of W-N and W-O coatings, Int. J. Refract. Met. Hard Mater. 28 (2010) 15–22. https://doi.org/10.1016/j.ijrmhm.2009.07.013.

[178] S.H. Mohamed, Thermal stability of tungsten nitride films deposited by reactive magnetron sputtering, Surf. Coatings Technol. 202 (2008) 2169–2175. https://doi.org/10.1016/j.surfcoat.2007.09.005.

[179] A.H. Abdelhameed, W. Jacob, Deposition of thermally stable tungsten nitride thin films by reactive magnetron sputtering, Surf. Coatings Technol. 375 (2019) 701–707. https://doi.org/10.1016/j.surfcoat.2019.07.046.

[180] H. Ju, X. He, L. Yu, J. Xu, The microstructure and tribological properties at elevated temperatures of tungsten silicon nitride films, Surf. Coatings Technol. 326 (2017) 255–263. https://doi.org/10.1016/j.surfcoat.2017.07.060.

[181] L. Yu, H. Zhao, H. Ju, J. Xu, Influence of Cu content on the structure, mechanical and tribological properties of W2N-Cu films, Thin Solid Films. 624 (2017) 144–151. https://doi.org/10.1016/j.tsf.2017.01.030.

[182] P.J. Kelly, R.D. Arnell, Magnetron sputtering: a review of recent developments and applications, Vacuum. 56 (2000) 159–172. https://doi.org/10.1016/S0042-207X(99)00189-X.

[183] W.D. Westwood, Sputter deposition, AVS The Ed, New York, 2003. https://lib.ugent.be/catalog/rug01:001466783.

[184] B. Window, N. Savvides, Charged particle fluxes from planar magnetron sputtering sources, J. Vac. Sci. Technol. A Vacuum, Surfaces, Film. 4 (1986) 196–202. https://doi.org/10.1116/1.573470.

[185] B. Window, Recent advances in sputter deposition, Surf. Coatings Technol. 71 (1995) 93–97. https://doi.org/10.1016/0257-8972(95)80024-7.

[186] R. a Powell, S.M. Rossnagel, PVD for microelectronics: sputter deposition applied to semiconductor manufacturing, 1998. https://doi.org/10.1016/S1079-4050(99)80012-X.

[187] M. Ohring, Materials Science of Thin Film: Deposition and Structure, 2nd edition, 2005.

[188] J. Musil, J. Vlcek, P. Baroch, Magnetron Discharges for Thin Films Plasma Processing, Mater. Surf. Process. by Dir. Energy Tech. (2006) 67–110. https://doi.org/10.1016/B978-008044496-3/50004-6.

[189] D.M. Mattox, Handbook of Physical Vapor Deposition (PVD) Processing - 2nd edition, 2010. https://doi.org/10.1016/B978-0-8155-2037-5.00025-3.

[190] C.A. Bishop, Vacuum Deposition onto Webs, Films and Foils, 2011. https://doi.org/10.1016/B978-1-4377-7867-0.00027-1.

[191] J.E. Greene, Review Article: Tracing the recorded history of thin-film sputter deposition: From the 1800s to 2017, J. Vac. Sci. Technol. A Vacuum, Surfaces, Film. 35 (2017) 05C204. https://doi.org/10.1116/1.4998940.

[192] W.M. Posadowski, A. Wiatrowski, J. Dora, Z.J. Radzimski, Magnetron sputtering process control by medium-frequency power supply parameter, Thin Solid Films. 516 (2008) 4478–4482. https://doi.org/10.1016/j.tsf.2007.05.077.

[193] G.G. Stoney, The Tension of Metallic Films Deposited by Electrolysis, Proc. R. Soc. A Math. Phys. Eng. Sci. 82 (1909) 172–175. https://doi.org/10.1098/rspa.1909.0021.

[194] R. Daniel, K.J. Martinschitz, J. Keckes, C. Mitterer, The origin of stresses in magnetron-sputtered thin films with zone T structures, Acta Mater. 58 (2010) 2621–2633. https://doi.org/10.1016/j.actamat.2009.12.048.

[195] P. Scherrer, Bestimmung der Größe und der inneren Struktur von Kolloidteilchen mittels Röntgenstrahlen, Nachrichten von Der Gesellschaft Der Wissenschaften Zu Göttingen, Math. Klasse. 2 (1918) 98–100. https://doi.org/10.1007/978-3-662-33915-2.

[196] R. Danz, P. Gretscher, C-DIC: A new microscopy method for rational study of phase structures in incident light arrangement, Thin Solid Films. 462–463 (2004) 257–262. https://doi.org/10.1016/j.tsf.2004.05.124.

[197] W.C. Oliver, G.M. Pharr, An improved technique for determining hardness and elastic modulus using load and displacement sensing indentation experiments, J. Mater. Res. (1992).

[198] B.K. Rao, P. Jena, Molecular view of the interfacial adhesion in aluminum-silicon carbide metal-matrix composites, Appl. Phys. Lett. 57 (1990) 2308–2310. https://doi.org/10.1063/1.103878.

[199] A.A. Voevodin, A.L. Yerokhin, V. V. Lyubimov, M.S. Donley, J.S. Zabinski, Characterization of wear protective Al-Si-O coatings formed on Al-based alloys by micro-arc discharge treatment, Surf. Coatings Technol. 86–87 (1996) 516–521. https://doi.org/10.1016/S0257-8972(96)03069-1.

[200] K. Bobzin, E. Lugscheider, M. Maes, C. Piñero, Relation of hardness and oxygen flow of Al2O3 coatings deposited by reactive bipolar pulsed magnetron sputtering, Thin Solid Films. 494 (2006) 255–262. https://doi.org/10.1016/j.tsf.2005.08.162.

[201] L. Šimurka, R. Čtvrtlík, J. Tomaštík, G. Bektaş, J. Svoboda, K. Bange, Mechanical and optical properties of SiO2 thin films deposited on glass, Chem. Pap. 72 (2018) 2143–2151. https://doi.org/10.1007/s11696-018-0420-z.

[202] D. Javdošňák, J. Musil, Z. Soukup, S. Haviar, R. Čerstvý, J. Houska, Tribological properties and oxidation resistance of tungsten and tungsten nitride films at temperatures up to 500 °C, Tribol. Int. 132 (2018) 211–220. https://doi.org/10.1016/J.TRIBOINT.2018.12.019.

[203] M. Jaroš, J. Musil, R. Čerstvý, S. Haviar, Effect of energy on structure, microstructure and mechanical properties of hard Ti(Al,V)N x films prepared by magnetron sputtering, Surf. Coatings Technol. (2017) 2–9. https://doi.org/10.1016/j.surfcoat.2017.06.074.

[204] A. Erdemir, A crystal chemical approach to the formulation of self-lubricating nanocomposite coatings, Surf. Coatings Technol. 200 (2005) 1792–1796. https://doi.org/10.1016/j.surfcoat.2005.08.054.

[205] G. Subhash, W. Zhang, Investigation of the overall friction coefficient in single-pass scratch test, Wear. 252 (2002) 123–134. https://doi.org/10.1016/S0043-1648(01)00852-3.

[206] T.T. Nguyen, T.T. Nguyen, G.T. Nguyen, V. V. Le, Effect of the Si content on structure and mechanical properties in Al1-xSixN materials, Vacuum. 129 (2016) 1–8. https://doi.org/10.1016/j.vacuum.2016.04.006.

[207] A. Pélisson-schecker, H.J. Hug, J. Patscheider, A. Pélisson-schecker, H.J. Hug, J. Patscheider, Complex phase compositions in nanostructured coatings as evidenced by photoelectron spectroscopy : The case of Al – Si – N hard coatings Complex phase compositions in nanostructured coatings as evidenced by photoelectron spectroscopy : The case of Al – Si, J. Appl. Phys. 023508 (2010). https://doi.org/:10.1063/1.3460099.

[208] Y.G. Shen, Effect of deposition conditions on mechanical stresses and microstructure of sputter-deposited molybdenum and reactively sputter-deposited molybdenum nitride films, Mater. Sci. Eng. A. 359 (2003) 158–167. https://doi.org/10.1016/S0921-5093(03)00336-8.

[209] D. Zhang, W. Chen, X. Ai, Z. Lv, Effect of the humidity on the friction and wear characteristics of $Si_3N_4$ –hBN composite ceramics, Proc. Inst. Mech. Eng. Part J J. Eng. Tribol. 231 (2017) 1517–1526. https://doi.org/10.1177/1350650117700342.

[210] A.M. Homola, J.N. Israelachvili, M.L. Gee, P.M. McGuiggan, Measurements of and relation between the adhesion and friction of two surfaces separated by molecularly thin liquid films., J. Tribol. 111 (1989) 675. https://doi.org/10.1115/1.3261994.

[211] T.J. Vink, W. Walrave, J.L.C. Daams, A.G. Dirks, M.A.J. Somers, K.J.A. Van Den Aker, Stress, strain, and microstructure in thin tungsten films deposited by dc magnetron sputtering, J. Appl. Phys. 74 (1993) 988–995. https://doi.org/10.1063/1.354842.

[212] Y.G. Shen, Y.W. Mai, Q.C. Zhang, D.R. McKenzie, W.D. McFall, W.E. McBride, Residual stress, microstructure, and structure of tungsten thin films deposited by magnetron sputtering, J. Appl. Phys. 87 (2000) 177. https://doi.org/10.1063/1.371841.

[213] T. Karabacak, C.R. Picu, J.J. Senkevich, G.C. Wang, T.M. Lu, Stress reduction in tungsten films using nanostructured compliant layers, J. Appl. Phys. 96 (2004) 5740–5746. https://doi.org/10.1063/1.1803106.

[214] V. Stelmakh, V. Rinnerbauer, J.D. Joannopoulos, M. Soljacic, I. Celanovic, J.J. Senkevich, C. Tucker, T. Ives, R. Shrader, M. Soljačić, I. Celanovic, J.J. Senkevich, C. Tucker, T. Ives, R. Shrader, Evolution of sputtered tungsten coatings at high temperature, J. Vac. Sci. Technol. A Vacuum, Surfaces, Film. 31 (2013) 061505. https://doi.org/10.1116/1.4817813.

[215] T. Karabacak, J.J. Senkevich, G.-C. Wang, T.-M. Lu, Stress reduction in sputter deposited films using nanostructured compliant layers by high working-gas pressures, J. Vac. Sci. Technol. A Vacuum, Surfaces, Film. 23 (2005) 986. https://doi.org/10.1116/1.1861940.

[216] H. Maier, J. Luthin, M. Balden, J. Linke, F. Koch, H. Bolt, Properties of tungsten coatings deposited onto the fine grain graphite by different methods, Surf. Coatings Technol. 142–144 (2001) 733–737. https://doi.org/10.1016/S0257-8972(01)01177-X.

[217] I. Petrov, F. Adibi, J.E. Greene, L. Hultman, J.E. Sundgren, Average energy deposited per atom: A universal parameter for describing ion-assisted film growth, Appl. Phys. Lett. 63 (1993) 36–38. https://doi.org/10.1063/1.109742.

[218] J. Musil, H. Poláková, J. Šuna, J. Vlček, Effect of ion bombardment on properties of hard reactively sputtered Ti(Fe)Nx films, Surf. Coatings Technol. 177–178 (2004) 289–298. https://doi.org/10.1016/j.surfcoat.2003.09.007.

[219] S. Zhang, D. Sun, Y. Fu, H. Du, Recent advances of superhard nanocomposite coatings: A review, Surf. Coatings Technol. 167 (2003) 113–119. https://doi.org/10.1016/S0257-8972(02)00903-9.

[220] J. Musil, Hard nanocomposite coatings: Thermal stability, oxidation resistance and toughness, Surf. Coatings Technol. 207 (2012) 50–65. https://doi.org/10.1016/j.surfcoat.2012.05.073.

[221] G.C.A.M. Janssen, J.D. Kamminga, Stress in hard metal films, Appl. Phys. Lett. 85 (2004) 3086–3088. https://doi.org/10.1063/1.1807016.

[222] M. Uekubo, T. Oku, K. Nii, M. Murakami, K. Takahiro, S. Yamaguchi, T. Nakano, T. Ohta, WNx diffusion barriers between Si and Cu, Thin Solid Films. 286 (1996) 170–175. https://doi.org/10.1016/S0040-6090(96)08553-7.

[223] B.H.A. Wriedt, The N-W (Nitrogen-Tungsten) System, 10 (1989) 358–367.

[224] Y.G. Shen, Y.W. Mai, D.R. McKenzie, Q.C. Zhang, W.D. McFall, W.E. McBride, Composition, residual stress, and structural properties of thin tungsten nitride films deposited by reactive magnetron sputtering, J. Appl. Phys. 88 (2000) 1380–1388. https://doi.org/10.1063/1.373827.

[225] J. Musil, F. Kunc, H. Zeman, H. Poláková, Relationships between hardness, Young's modulus and elastic recovery in hard nanocomposite coatings, Surf. Coatings Technol. 154 (2002) 304–313. https://doi.org/10.1016/S0257-8972(01)01714-5.

[226] J. Musil, J. Sklenka, R. Čerstvý, Protection of brittle film against cracking, Appl. Surf. Sci. 370 (2016) 306–311. https://doi.org/10.1016/j.apsusc.2016.02.132.

[227] J. Musil, P. Novák, R. Čerstvý, Z. Soukup, Tribological and mechanical properties of nanocrystalline-TiC/a-C nanocomposite thin films, J. Vac. Sci. Technol. A Vacuum, Surfaces, Film. 28 (2010) 244–249. https://doi.org/10.1116/1.3294717.

[228] A. Erdemir, A crystal-chemical approach to lubrication by solid oxides *, Tribol. Lett. 8 (2000) 97–102. https://doi.org/10.1023/A:1019183101329.

[229] G. Gassner, P.H. Mayrhofer, K. Kutschej, C. Mitterer, M. Kathrein, A new low friction concept for high temperatures: Lubricious oxide formation on sputtered VN coatings, Tribol. Lett. 17 (2004) 751–756. https://doi.org/10.1007/s11249-004-8083-z.

[230] G. Gassner, P.H. Mayrhofer, K. Kutschej, C. Mitterer, M. Kathrein, Magnéli phase formation of PVD Mo-N and W-N coatings, Surf. Coatings Technol. 201 (2006) 3335–3341. https://doi.org/10.1016/j.surfcoat.2006.07.067.

[231] S.M. Aouadi, B. Luster, P. Kohli, C. Muratore, A.A. Voevodin, Progress in the development of adaptive nitride-based coatings for high temperature tribological applications, Surf. Coatings Technol. 204 (2009) 962–968. https://doi.org/10.1016/j.surfcoat.2009.04.010.

[232] K. Holmberg, Coatings Tribology: Properties, Techniques and Applications in Surface Engineering, 1994. https://doi.org/10.1002/vipr.19950070117.

[233] J. Musil, J. Vlček, P. Zeman, Hard amorphous nanocomposite coatings with oxidation resistance above 1000°C, Adv. Appl. Ceram. 107 (2008) 148–154. https://doi.org/10.1179/174367508X306460.

# VIII. Further publications of the candidate

## 1. Papers in international journals

[1] J. Musil, **D. Javdošňák**, R. Čerstvý, S. Haviar, G. Remnev, V. Uglov
"*Effect of energy on the formation of flexible hard Al-Si-N films prepared by magnetron sputtering*"
Vacuum 133 (2016) 43-45

[2] J. Musil, Š. Kos, S. Zenkin, Z. Čiperová, **D. Javdošňák**, R. Čerstvý
"*β- ($Me_1$, $Me_2$) and $MeN_x$ films deposited by magnetron sputtering: Novel heterostructural alloy and compound films*"
Surf. Coat. Technol. 337 (2018) 75–81

[3] **D. Javdošňák**, J. Musil, Z. Soukup, S. Haviar, R. Čerstvý, J. Houška
"*Tribological properties and oxidation resistance of tungsten and tungsten nitride films at temperatures up to 500 °C*"
Trib. Int. 132 (2019) 211–220

## 2. Oral presentations at international conferences

[1] **D. Javdošňák**, J. Musil, Z. Soukup, S. Haviar, R. Čerstvý, J. Houška
"*Tribological properties and oxidation resistance of $WN_x$ thin films at high temperatures up to 500 °C*" 45th International Conference on Metallurgical Coatings and Thin Films (ICMCTF 2018), 23.–27. 4. 2018, San Diego, USA

[2] **D. Javdošňák**, J. Musil, Z. Soukup, S. Haviar, R. Čerstvý, J. Houška
"*Tribological and mechanical properties and oxidation resistance of tungsten and tungsten nitride films at temperatures up to 500 °C*" 37th European Materials Research Society (E-MRS 2019 Spring Meeting), 27.–31.5. 2019, Nice, France

[3] **D. Javdošňák**, J. Musil, Z. Soukup, S. Haviar, R. Čerstvý, J. Houška
"*Tribological and mechanical properties and oxidation resistance of tungsten and tungsten nitride films at temperatures up to 500 °C*" 21st International Vacuum Congress (IVC 2019), 1.–5.7. 2019, Malmö, Sweden

## 3. Poster presentations at international conferences

[1] **D. Javdošňák**, J. Musil, Z. Soukup, R. Čerstvý, S. Haviar, J. Houška
"*Mechanical properties of $WN_x$ films and their thermal stability*" 16th International Conference on Plasma Surface Engineering (PSE 2018), 17.–21. 9. 2018, Garmisch-Partenkirchen, Germany

[2] Z. Soukup, J. Musil, **D. Javdošňák**, R. Čerstvý, S. Haviar
"*Tribological properties of tungsten nitride films at temperatures up to 500 °C*"16th International Conference on Plasma Surface Engineering (PSE 2018), 17.–21. 9. 2018, Garmisch-Partenkirchen, Germany

[3] **D. Javdošňák**, J. Musil, Z. Soukup, R. Čerstvý, S. Haviar, J. Houška
"*Mechanical properties of $WN_x$ films and their oxidation resistance*" 28th Symposium on Plasma Physics and Technology (SPPT 2018), 18.–21. 6. 2018, Prague, Czech Republic

[4] **D. Javdošňák**, Z. Soukup, J. Musil, R. Čerstvý, S. Haviar, J. Houška
"*Tribological properties and oxidation resistance of $WN_x$ thin films at high temperatures up to 500 °C*" 16th International Conference on Reactive Sputter Deposition (RSD 2017), 4.–6. 12. 2017, Plzeň, Czech Republic

[5] **D. Javdošňák**, J. Musil, R. Čerstvý, S. Haviar, J. Houška
"*Effect of energy on the formation of flexible hard Al-Si-N films prepared by magnetron sputtering*" E-MRS 2017 Spring Meeting, 22.–26. 5. 2017, Strasbourg, France

[6] **D. Javdošňák**, J. Musil, R. Čerstvý, S. Haviar, J. Houška
"*Effect of energy on the formation of flexible hard Al-Si-N films prepared by magnetron sputtering*" 15th International Conference on Reactive Sputter Deposition 2016 (RSD2016), 1.–2. 12. 2016 Ghent, Belgium

# Abstract

A. The Al-Si films with Si content ranging from 6 to 98 at.% were grown on a Si (100) substrate by non-reactive magnetron sputter deposition from alloy or Al/Si composed targets with different Al and Si fractions in the erosion zone. X-ray diffraction and scanning electron microscopy results show that the Al-Si films exhibit (1) either a crystalline structure consisting of two clearly separated fcc-Al and diamond c-Si phase with strong (111) texture, or an amorphous structure, and (2) fine-grained non-columnar microstructure. It was found that Al-Si films with ≥ 95 at.% Si exhibit enhanced (1) hardness *H* up to 15 GPa, (2) cracking resistance, and (3) wear resistance. Moreover, the soft (*H* ≤ 8 GPa) Al-Si films with > 70 at.% Al exhibit cracking resistance, due to its ductility. The Al-Si films with ≥ 95 at.% Si exhibit moderate wear rate of 1–2 × $10^{-6}$ $mm^3$/Nm and high friction coefficient of 0.85, due to formation of abrasive hard and non-lubricating oxidation products $AlO_x$ and $FeO_x$ in the wear track.

B. This study demonstrates significance of the microstructure on the wear resistance of the ceramic Al-Si-N films deposited by magnetron sputtering. The microstructure of the films was tuned by the Si content. Moreover, the effect of the humidity (air and dry nitrogen) during the dry sliding on the wear rate of the films was investigated as well. It was found that the films deposited with 4, 10 and 30 at. % Si exhibit (1) columnar microstructure, (2) non-columnar microstructure, and (3) amorphous microstructure, respectively. The high hardness *H* = 28–33 GPa, high ratio of hardness to effective Young's modulus $H/E^*$ > 0.10, high elastic recovery $W_e$ > 60 % and compressive macro-stress higher than 1 GPa do not have the same effect as microstructure on the wear resistance of the films.

C. This study dealt with the investigation of the adhesion improvement and finding deposition conditions under which the W films exhibit enhanced mechanical properties. It was found that the improved plasma etching with enhanced ionization is an effective way to remove oxides and other contaminants from the substrate surface and to achieve good adhesion even within several micron thick W films with high compressive macro-stress up to 2.8 GPa. Furthermore, the W films were prepared at different energies of ion bombardment and different plasma densities, using low-density DC discharge ($W_t$ = 2.3 W/$cm^2$) and high-density AC pulsed unipolar discharge ($W_{t\ pulse}$ ≈ 100 W/$cm^2$). It was found that the W films deposited at a low ion energy and at high density discharge exhibit enhanced *H* up to 24.3 GPa.

D. The formation of the films with high-temperature (high-T) β-Ti phase by magnetron sputter-deposition, their thermal stability and resistance to cracking were investigated in detail. It was found that addition of 12 at.% of the α-W with bcc structure into the α-Ti with hexagonal structure had the effect to: (1) stabilize β-Ti(W) phase, (2) enhance two times the hardness *H* up to 5 GPa, the hardness to effective Young's modulus ratio $H/E^*$ up to

0.05 and elastic recovery $W_e$ up to 31 %, and (3) enhance cracking resistance. Furthermore, thermally annealed β-($Ti_{88}W_{12}$) films at 600 °C in Ar exhibit (1) partially converted structure with β-($Ti_{88}W_{12}$) and α-($Ti_{88}W_{12}$) phases, (2) enhanced $H$ up to 13 GPa, $H/E^*$ up to 0.08 and $W_e$ up to 55 %, and (3) cracks during an indentation test at high loads up to 1 N. The conditions under which the β-Ti(W) phase film was successfully stabilized are discussed in detail. Moreover, the conditions under which the soft $H \leq 5$ GPa and hard $H > 10$ GPa alloy or pure metal films are resistant to cracking, are discussed in detail.

E. The structure, microstructure, mechanical and tribological properties and oxidation resistance of $WN_x$ films with a stoichiometry $x$ = [N]/[W] ranging from 0 to 1.5 prepared by magnetron sputtering was investigated. It was found that (i) films with $x \leq 0.20$ exhibit α-W structure and columnar microstructure, while films with $x \geq 0.27$ exhibit β-$W_2N$ or δ-WN structure and fine-grained microstructure, (ii) the hardness $H$ and hardness to effective Young's modulus $H/E^*$ strongly affect the tribological properties of the films. Furthermore, we investigate and discuss how the tribological properties are affected by the humidity and by the film oxidation. The oxidation is expressed in terms of the thickness of the $WO_3$ scale, and is shown to be significantly different for $x \leq 0.20$ and $x \geq 0.27$ $WN_x$ films.

# Resumé česky

A. Vrstvy na bázi Al-Si s obsahem Si v rozmezí od 6 do 98 at.% byly připraveny na Si (100) substrátu magnetronovým nereaktivním naprašováním ze slitinového terče nebo ze složených terčů s různým obsahem Al a Si v erozní zóně. Rentgenová difrakce a řádkovací elektronová mikroskopie ukázala, že vrstvy Al-Si jsou (1) buď krystalické se dvěma jasně oddělenými fázemi fcc-Al a diamantová c-Si s přednostní orientací (111), nebo amorfní, a (2) jemnozrnné s nesloupcovou mikrostrukturou. Zjistilo se, že Al-Si vrstvy s obsahem Si ≥ 95 at.% mají zvýšenou (1) tvrdost až do 15 GPa, (2) odolnost vůči praskání, a (3) odolnost vůči otěru. Vrstvy Al-Si s obsahem Al > 70 at.% jsou měkké a navíc odolné proti praskání díky jejich duktilitě. Vrstvy Al-Si s obsahem Si ≥ 95 at.% mají mírný koeficient opotřebení 1–2 × $10^{-6}$ $mm^3/Nm$ a vysoký koeficient tření 0.85, kvůli tvorbě tvrdých abrazivních a nemazavých produktů oxidace $AlO_x$ a $FeO_x$ v dráze otěru.

B. Tato studie demonstruje význam mikrostruktury na odolnost keramických vrstev Al-Si-N naprašovaných magnetronovým naprašováním proti opotřebení. Mikrostruktura vrstev byla řízena obsahem Si ve vrstvách. Mimoto, byl studován vliv vlhkosti prostředí (vzduch a suchý dusík) v průběhu suchého klouzání na opotřebení vrstev. Zjistilo se, že vrstvy s obsahem Si 4, 10, a 30 at.% mají v tomto pořadí (1) sloupcovou mikrostrukturu, (2) nesloupcovou mikrostrukturu, a (3) amorfní mikrostrukturu. Vysoká tvrdost $H$ = 28–33 GPa, vysoký poměr tvrdosti k efektivnímu Youngova modulu $H/E^*$ > 0.10 a vysoká elastická vratnost $W_e$ > 60 % a tlakové makro-pnutí vyšší než 1 GPa nemají tak významný vliv na opotřebení vrstev ve srovnání s mikrostrukturou.

C. Tato studie se zabývá nejen vylepšením přilnavosti vrstev k podkladu, ale také hledáním podmínek naprašování, při kterých vrstvy W mají vylepšené mechanické vlastnosti. Bylo zjištěno, že leptání podložky plazmatem se zvýšenou ionizací pomocí magnetronového výboje se jeví jako efektivní způsob k odstranění oxidů a jiných nečistot z jejího povrchu, a k dosažení lepší přilnavosti vrstvy k podložce, a to i přes vysokou tloušťku (několik mikrometrů) vrstev s vysokým zbytkovým tlakovým pnutím až 2.8 GPa. Mimoto, byly vrstvy W připraveny za různých podmínek energií iontového bombardu a za různých hustot plazmatu, s použitím nízko-hustotního DC výboje ($W_t$ = 2.3 $W/cm^2$) a vysoko-hustotního AC unipolárního pulzního výboje ($W_{t\,pulse}$ ≈ 100 $W/cm^2$). Bylo zjištěno, že vrstvy W naprašované za podmínek nízké energie iontů a vysoké hustotě plazmatu jsou velmi tvrdé až 24.3 GPa.

D. Tvorba vrstev s vysoko-teplotní (high-T) β-Ti fází pomocí magnetronového naprašování, jejich tepelná stabilita a jejich odolnost proti praskání byla podrobně vyšetřovaná. Zjistilo se, že přidáním 12 at.% W s α-W fází a bcc strukturou do α-Ti s šesterečnou strukturou má za následek (1) stabilizace β-Ti(W) fáze, (2) dvojnásobné zvýšení tvrdosti $H$, poměru tvrdosti k efektivnímu Youngova modulu pružnosti $H/E^*$ a elastické vratnosti $W_e$ na $H$ = 5 GPa, $H/E^*$ = 0.05 a $W_e$ = 31 %. Mimoto, bylo zjištěno, že po tepelném žíhání vrstvy β-

($Ti_{88}W_{12}$) při teplotě 600 °C v Ar dochází k (1) částečné přeměně struktury na směs fází β-($Ti_{88}W_{12}$) a α-($Ti_{88}W_{12}$), (2) zvýšení $H$ na 13 GPa, $H/E^*$ na 0.08 a $W_e$ na 55 %, a (3) tvorbě prasklin po indentačním testu při vysokých zátěží až do 1 N. Dále byly podrobně vyšetřovány podmínky, za kterých byla úspěšně připravena vrstva se stabilizovanou β-Ti(W) fází. Také byly podrobně diskutovány podmínky, za kterých měkké $H \leq 5$ GPa a tvrdé $H > 10$ GPa vrstvy jsou odolné proti praskání.

E. Struktura, mikrostruktura, mechanické a tribologické vlastnostmi a oxidační odolností tenkých vrstev na bázi $WN_x$ připravených magnetronovým naprašováním se stechiometrií $x = [N]/[W]$ v rozsahu od 0 do 1.5 byla zkoumána. Zjistilo se že (i) vrstvy s $x \leq 0.20$ vykazují α-W strukturu se sloupcovou mikrostrukturou, zatímco vrstvy s $x \geq 0.27$ vykazují β-$W_2N$ nebo δ-WN strukturu a jemnozrnnou mikrostrukturu, (ii) tvrdost $H$ a poměr tvrdosti k efektivnímu Youngově modulu $H/E^*$ silně ovlivňuje tribologické vlastnosti vrstev. Dále jsme vyšetřovali a diskutovali, jak jsou tribologické vlastnosti ovlivněny vlhkostí okolního vzduchu a oxidací vrstev. Oxidace vrstev je hodnocena na základě tloušťky vzniklé vrstvy $WO_3$ na povrchu $WN_x$ vrstvy, a ukazuje se, že je výrazně odlišná u vrstev $WN_x$ s $x \leq 0.20$ a $x \geq 0.27$.